The 18F(p,α)15O reaction: A textbook case in nuclear astrophysics

Francois de Oliveira Santos

Progress in Particle and Nuclear Physics 142 (2025) 104154

Contents lists available at ScienceDirect

Progress in Particle and Nuclear Physics

journal homepage: www.elsevier.com/locate/ppnp

Review

The $^{18}F(p,\alpha)^{15}O$ reaction: A textbook case in nuclear astrophysics

F. de Oliveira Santos

GANIL, CEA/DSM-CNRS/IN2P3, Boulevard Henri Becquerel, Caen Cedex 5, F-14076, France

ARTICLE INFO

Keywords:
Nuclear astrophysics
Novae
Experimental techniques
Radioactive beams
Indirect methods
Direct reactions
$^{18}F(p,\alpha)^{15}O$

ABSTRACT

Nuclear astrophysics recently celebrated its 100th anniversary and remains an active field of science. This article reviews several contemporary experimental techniques used to determine nuclear-reaction rates. Additionally, it presents some theoretical aspects directly related to these experimental techniques, providing an introduction to the fundamental principles underlying them. The $^{18}F(p,\alpha)^{15}O$ reaction, which is associated with γ-ray emission from classical novae during the first hours after expansion, is used as a central theme throughout the article. Several examples of recent experiments are highlighted, particularly those conducted in nuclear facilities utilizing radioactive beams.

Contents

E-mail address: oliveira@ganil.fr.

https://doi.org/10.1016/j.ppnp.2025.104154

Available online 10 January 2025

1. Introduction

In the article J. Perrin published in 1919 [1], he was the first to propose the idea that nuclear reactions could be at the origin of the energy generated by the Sun and the other stars. He wrote that (translated from French): *"...the nebula of gas contracting, the collisions between light atoms become more and more numerous... able to fuse into heavy atoms, and ... accompanied by ultra-X rays, which, for the most part, do not come out of the star whose temperature becomes colossal.... it is... a deep penetration that intimately mixes atomic nuclei"*. For the first time, the two physics fields, Nuclear Physics and Astrophysics, were coupled. The same year, E. Rutherford carried out the first induced nuclear reaction in laboratory [2], proving that it is possible to transform atomic nuclei into other nuclei, and F. W. Aston made the first accurate measurements of atomic masses [3], proving that the combination of light elements into heavier ones is accompanied by a large excess of energy. A. S. Eddington concluded in 1920 [4]: *"... Aston has further shown conclusively that the mass of the helium atom is less than the sum of the masses of the 4 hydrogen atoms which enter into it... We can therefore at once calculate the quantity of energy liberated when helium is made out of hydrogen. If 5 per cent of a star's mass consists initially of hydrogen atoms, which are gradually being combined to form more complex elements, the total heat liberated will more than suffice for our demands, and we need look no further for the source of a star's energy"*. A new branch of physics, called *Nuclear Astrophysics*, emerged. Since then, Nuclear Astrophysics has followed a route full of splendid discoveries. It led us, in 2017, almost a century after the first article, to a new excitement due to the first observation of the coalescence of two neutron stars [5] and the associated new nucleosynthesis process, which looks like the scenario proposed in 1948 by Alpher, Bethe and Gamow [6], also referred as the $\alpha\beta\gamma$-paper, of an *"... early stage of matter as a highly compressed neutron gas..."*.

Among all astrophysical phenomena, novae are particularly fascinating objects, not least because it is possible to observe these events through binoculars almost once every year. These luminous outbursts occur in binary star systems that include a white dwarf star, a remnant of a star that exhausted its nuclear fuel and collapsed into a dense and hot core. The strong gravitational field of the white dwarf draws matter away from its companion star, often a main-sequence or red giant star. This transfer of matter sets the stage for the nova event. As the white dwarf accumulates hydrogen from its companion, the hydrogen builds up on its surface. When the pressure and temperature become sufficiently high, a thermonuclear runaway reaction ensues, leading to a sudden increase in brightness. During these nova outbursts, the temperatures can reach $3–4 \times 10^8$ K. At such extreme temperatures, rapid nuclear

reactions occur, allowing for the synthesis of both stable and radioactive nuclei [7]. The process is dominated by proton-capture reactions. These captures not only produce a variety of elements but also release a significant amount of energy, contributing to the nova brightness. In the initial hours following the onset of the nova explosion, the emission of γ-rays is particularly intense. The γ-ray spectrum is dominated by the 511 keV γ line, which originates from the annihilation of positrons [8,9]. Detecting these γ-rays from nova ejecta is a key goal for astronomers, as it would provide a direct means to study the nucleosynthesis processes occurring in novae and the mechanisms of matter ejection [10]. Although such observations have not yet been realized, they are anticipated in the near future [11].

Positrons are largely generated by the decay of the ^{18}F ($t_{1/2}$ = 109.77 min) nuclei in the first day of the nova. Thus, the number of γ-rays emitted is proportional to the ^{18}F content in the nova ejecta. As the ^{18}F lifetime is comparable to the time the ejected envelope becomes transparent to γ-rays, the observations of ^{18}F should provide information on the ejecta dynamics. In 2020, for the first time, a nova was detected a few hours (<8 h) after the explosion [12]. Nova RETICULI 2020 was detected in X-rays by the eROSITA satellite, 8 days before it was observed in visible light. So, in the next few years, an alert can be expected to be triggered shortly after the explosion, and the possibility of the nova being studied in the γ-ray range just a few hours after the alert can be anticipated.

The role of the ^{18}F(p, α)^{15}O reaction in producing ^{18}F in novae was first thoroughly explored in 2000 by A. Coc et al. [9]. This pioneering work highlighted the importance of this reaction and sparked an extensive series of experiments over the subsequent two decades, aimed at accurately determining the reaction rate. Initial work to determine the rate of this reaction was undertaken by Wiescher and Kettner as early as 1982 [13], but very little experimental information was available at that time, so the uncertainty of the rate was very high. The first real experimental study of ^{19}Ne aiming to determine the astrophysical ^{18}F(p, α)^{15}O rate was proposed in 1998 by Utku et al. [14]. The ^{18}F(p, α)^{15}O reaction is probably the most studied reaction in nuclear astrophysics recently, with more than 50 studies published in the last two decades. Despite this considerable effort, its rate remains uncertain at nova temperatures with a factor of ∼10 uncertainty in the predicted abundance of ^{18}F ejected by nova explosions [15].

This article reviews several experimental techniques used today to determine astrophysical reaction rates. In order to better compare these approaches, we have chosen to show the results obtained in the study of the same reaction. Reaction ^{18}F(p, α)^{15}O was chosen. This reaction has been studied in the last three decades using five different experimental techniques: direct measurements, elastic resonant scattering, inelastic scattering, inverse-kinematics and Trojan Horse transfer reactions, and they will be presented in this article. By way of introduction, some useful definitions are presented. It should be noted that definitions are sometimes simplified, and that some of them may vary from other articles. Emphasis is placed on the experimental aspects to be considered when choosing the approach to be used. A critical comparison between these experimental methods is made. Some theoretical aspects directly related to these methods are also presented. Several examples of recent experiments are given, but this article is not an exhaustive review of the various experimental studies carried out to determine the rate of this reaction. This reaction illustrates the current challenges of nuclear astrophysics, linked in particular to the new radioactive beams recently produced in various facilities around the world.

2. Direct measurement of the reaction rate

2.1. Reaction rate

In stellar environments, the probability that a proton undergoes a reaction with ^{18}F is proportional to $N_{^{18}\mathrm{F}}$, the number density of ^{18}F nuclei, and to the product $v\ \sigma(v)$ of the velocity times the cross section [16–18]. It follows that the number of ^{18}F nuclei consumed per unit of volume per second with velocities between v and $v + dv$ is given by $N_p\ N_{^{18}\mathrm{F}}\ v\ \sigma(v)\ \Phi(v)\ dv$, with N_p the number density of protons, and $\Phi(v)dv$ is the probability to have the relative velocity between v and $v + dv$. The total number of reactions per second, integrated over all velocities, is equal to

$$N_p\ N_{^{18}\mathrm{F}} \int_0^\infty v\ \sigma(v)\ \Phi(v)\ dv. \tag{1}$$

The thermonuclear reaction rate is defined as $r = \int_0^\infty v\ \sigma(v)\ \Phi(v)\ dv$. In most cases, the probability density $\Phi(v)$ is given by the Maxwell–Boltzmann velocity distribution, thus the reaction rate is

$$r = \sqrt{\frac{8}{\pi\ \mu}}(kT)^{-\frac{3}{2}} \int_0^\infty \sigma(E)\ E\ e^{-\frac{E}{kT}} dE \tag{2}$$

with μ the reduced mass, $\mu = \frac{m_{^{18}\mathrm{F}} m_p}{m_{^{18}\mathrm{F}} + m_p} \approx 0.95$ atomic mass unit, $m_{^{18}\mathrm{F}}$ and m_p are the masses of ^{18}F and p, and k the Boltzmann constant. The reaction rate is a function of the temperature, and it is usually given in cm^3 mol^{-1} s^{-1}, which is obtained to multiplying Eq. (2) by the Avogadro constant. Reaction rates are usually given in the form of tables [19], or fitted into analytical expressions of the temperature [16,20], and then used in astrophysics simulation codes.

Recently, the availability of high-intensity laser facilities capable of delivering petawatts of power into small volumes has opened up the possibility of using such facilities to measure reaction rates. The very powerful laser beams produce plasmas at high temperature and high density in which the astrophysical reactions occur. Several high-intensity laser facilities are in their commissioning phase. First results were obtained recently in the reactions $d(d,n)^3$He and ^{3}He$(d,p)^4$He [21,22] using the Texas Petawatt laser. The predicted rate of the ^{18}F(p, α)^{15}O reaction at the temperature of 0.25 GK is $r \approx 1$ cm^3 mol^{-1} s^{-1} [15]. In the laboratory, if it were possible to heat a hydrogen target (1 mm^3, 1 g cm^{-3}) mixed with 10^9 atoms of ^{18}F at this temperature for 10^{-9} s (the plasma disassembly time), only 1 atom of ^{15}O would be produced. Yet, there is still a long way to go before being able to apply this method to the ^{18}F(p, α)^{15}O case.

2.2. Requested precision

The reaction rates are known at best with an accuracy typically in the order of a factor 2, see [23]. The reactions $^{12}C(\alpha, \gamma)^{16}O$ and $^{3}He(^{4}He, \gamma)^{7}Be$ are among those that require more accurate values. For the former case, it was shown that its rate significantly influences the pre-supernova stellar structure, the explosive nucleosynthesis and the nature, neutron star or black hole, of the remnant left after the core-collapse. A 10% accuracy is requested [24]. For the latter reaction, its rate is linked to the solar neutrinos measurement and therefore it constrains the standard solar model. A 3% accuracy is requested [25].

Despite recent progress [26–31], the $^{18}F(p, \alpha)^{15}O$ reaction rate is still uncertain by a factor 3, making it the most uncertain reaction among the creation and destruction pathways of ^{18}F [32]. This translates into more than a factor 10 uncertainty for the calculated abundance of ^{18}F in the ejecta of novae explosions [15]. A better understanding of the reaction rates relating to the production and destruction of ^{18}F is required with uncertainties below 30% to calculate ^{18}F yields in novae. This would improve the reliability of the predicted γ-ray fluxes that should enlighten us on the underlying novae outbursts.

3. Direct measurement of the nuclear cross section

3.1. Principle

All terms in Eq. (2) are known, except the cross section, which has to be determined experimentally in the relevant energy range. Ideally one would measure the cross section $\sigma(E)$ of the $^{18}F(p, \alpha)^{15}O$ reaction directly at the appropriate energies. Reactions between charged particles, however, have very low cross sections ($\sigma \lesssim 1$ μb) at the energies of interest because of the strong Coulomb repulsion and the very weak penetrability through the Coulomb barrier by tunnel effect. Thus, it is extremely difficult to measure directly the cross sections of interest. Direct measurements of cross sections at the relevant energies were possible in a few dozen cases only. Generally, it requires weeks or months of beam time and extremely low background conditions.

3.2. Astrophysical S factor

For the $^{18}F(p, \alpha)^{15}O$ reaction, in novae, the kinetic energies of the particles are E∼400 keV at maximum, this is well below the Coulomb barrier H

$$H_{^{18}F+p} \sim 0.6 \text{ MeV} \frac{Z_{^{18}F}\, Z_p}{A^{1/3}} \sim 2 \text{ MeV} \tag{3}$$

with $A = 18 + 1$, $Z_{^{18}F} = 9$ and $Z_p = 1$. In these conditions, fusion of the two charged particles is unlikely and can only proceed through the quantum tunneling effect. The probability of penetrating the Coulomb barrier can be calculated approximately with the Gamow function

$$P(E) = e^{-2\pi\eta} \tag{4}$$

with

$$2\pi\eta = 31.29\, Z_{^{18}F}\, Z_p \left[\frac{\mu \text{ (amu)}}{E \text{ (keV)}}\right]^{1/2}. \tag{5}$$

It is very convenient to write the cross sections as

$$\sigma(E) \equiv \frac{S(E)}{E} e^{-2\pi\eta} \tag{6}$$

where the Coulomb effect is set apart from the total cross section by the $e^{-2\pi\eta}$ factor. The E^{-1} factor is a non-nuclear energy-dependent term, proportional to the de Broglie wavelength to the square, i.e. $E^{-1} \propto \lambda^2 = (\frac{h}{mv})^2$, the geometrical cross section of the nucleus. The nuclear dependence of the cross section is reduced to the function $S(E)$. It is called *the astrophysical S factor*. This function usually varies slowly with energy.

3.3. Gamow window

The integrand of Eq. (2) is negligible at low energy since $\lim_{E\to 0} \sigma(E) = 0$, and at high energy, $\lim_{E\to+\infty} e^{-\frac{E}{kT}} = 0$, then it is non negligible in a limited range of energies: $E_0 - \Delta/2 \leqslant E \leqslant E_0 + \Delta/2$. This range is called the *Gamow window*. The Gamow window can be calculated using different analytical formulas [16,33]. For reactions between charged particles at relatively low temperatures

$$\begin{aligned} E_0 &\approx 0.122(Z_1^2 Z_2^2 \mu T_9^2)^{1/3} \text{ MeV} \\ \Delta &\approx 0.237(Z_1^2 Z_2^2 \mu T_9^5)^{1/6} \text{ MeV} \end{aligned} \tag{7}$$

where Z_1 and Z_2 are the charges of the interacting nuclei, T_9 is the temperature of the environment in GK. Note that Eq. (7) is an approximation, it has to be corrected in several cases, e.g. for reactions involving broad resonances, or for reactions with (not charged) neutrons, or at extreme temperatures. In the novae explosions, with temperatures $T = 0.05$–0.35 GK, the $^{18}F(p, \alpha)^{15}O$ reaction occurs in the $E_0 \approx 70$–260 keV energy range and in the $\Delta \approx 40$–126 keV energy windows [33].

Table 1
List of all direct measurements of the $^{18}F(p, \alpha)^{15}O$ reaction.

Laboratory	^{18}F beam Intensity (pps)	Purity %	Ref.
LLN	10^6	100	[34,35]
ANL	5×10^5	0.4	[36,37]
HRIBF	2×10^5	20	[38–41]
TRIUMF	5×10^6	60–95	[42,43]
GANIL	2×10^4	97	[44]

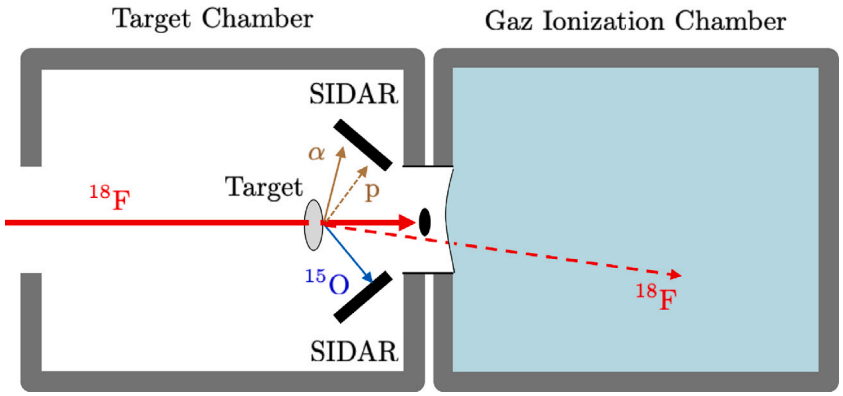

Fig. 1. Scheme of the experimental setup used for the direct measurement of the $^{18}F(p, \alpha)^{15}O$ reaction [38,41]. The experiment was carried out in inverse kinematics with a ^{18}F beam. The reaction products, ^{15}O, p and α, were detected with silicon detectors (SIDAR) placed behind the thin plastic target composed with hydrogen.

3.4. Projectile

The ^{18}F isotope is radioactive and short-lived, so it cannot be used as a target, it must be used as a beam. The $^{18}F(p, \alpha)^{15}O$ reaction is a favorable case for a direct measure of the cross section. On the one hand, this reaction has one of the highest cross sections in astrophysics since it involves the strong nuclear interaction on both the entrance and exit channels. Moreover, in explosive astrophysical scenarios, temperatures exceed several hundred million degrees and the Gamow window is in the hundreds of keV range, leading to cross sections of up to several millibarns. On the other hand, the ^{18}F beam is among the most intense radioactive beams currently available in Radioactive Ion Beam (RIB) facilities, see Table 1. Also note, the purity of the beam is another very important parameter.

3.5. Incident energy

The beam energy must correspond exactly to the aimed energy in the center of mass. For example, 250 keV in the center of mass corresponds to a ^{18}F beam energy of 5 MeV. In practice, the beam energy is higher so that the desired center-of-mass energy is achieved at the center of the target.

3.6. Target

Given the very short lifetime of ^{18}F ($t_{1/2}$ = 109.77 min), all direct measurements of $^{18}F(p, \alpha)^{15}O$ were carried out in inverse kinematics (heavy ion on light target nucleus). Plastic targets (containing hydrogen) were used in all the experiments. The target is necessarily thin due to the exponential fall in the cross section with decreasing energy and the energy losses of the beam in the target. The need to have the ejectiles exit the target also dictates a thinner target.

It is possible that in the future a direct kinematic measurement could be made using a ^{18}F target, by rapidly producing and extracting ^{18}F nuclei from its production target using techniques that already exist in the medical field.

3.7. Experimental setup

The "on-the-fly" method was used in all direct measurements of the $^{18}F(p, \alpha)^{15}O$ reaction. Fig. 1 shows one example of experimental setup used for this measurement. Products of the reaction are identified using reaction kinematics, by plotting the measured energy of the particles against time of flight [34], or as a function of their measured angle, see Fig. 2. The reaction of interest can be identified as well as the reactions induced by the beam contaminant (^{18}O).

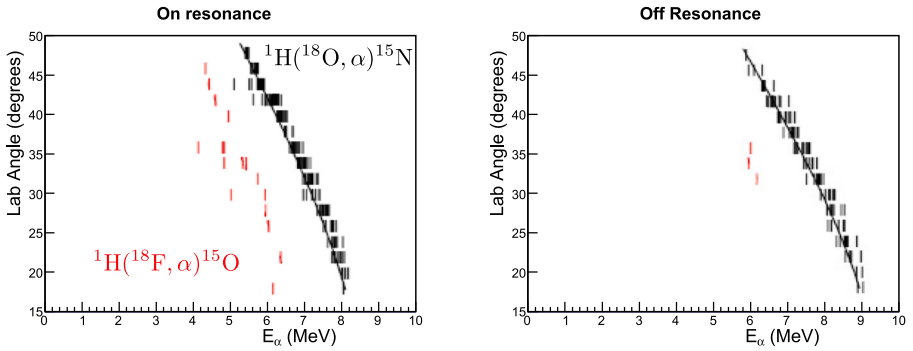

Fig. 2. The angle of the measured α particles is plotted as a function of their energy, in the direct measurement of the ^{18}F(p, α)^{15}O reaction [41]. (Left) The measurement is taken at the energy of the 332-keV resonance in ^{19}Ne, at E_{beam} = 6.6 MeV. (Right) Outside this resonance, at E_{beam} = 7.5 MeV. The reaction of interest is easily identified on this plot, as well as reactions from ^{18}O, a contaminant in the beam.

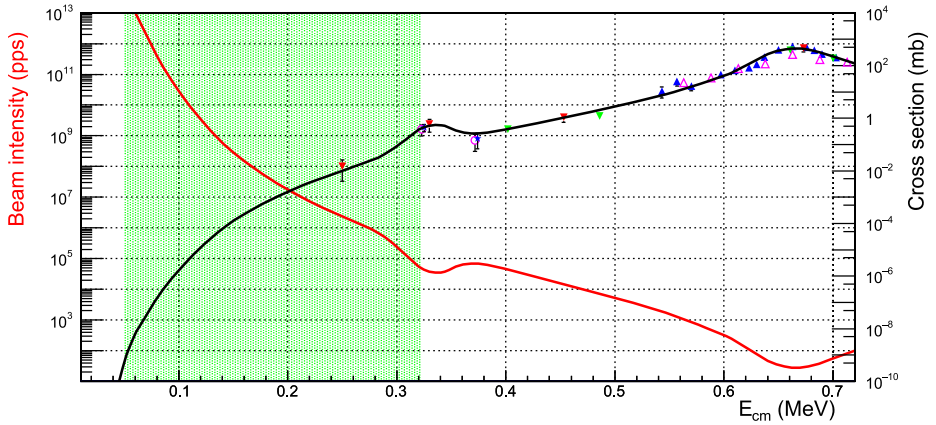

Fig. 3. All direct measurements of the ^{18}F(p, α)^{15}O total cross section (vertical axis on the right) is shown as a function of the c.m. energy. The points are measured values taken from Ref. [35,38,40–42,44]. The black curve shows a theoretical fit to the data. The red curve shows the beam intensity (left axis) needed to produce 1 reaction per week. The green area corresponds to the Gamow window of novae explosions. The lowest energies are inaccessible with the present means.

It should be noted that ^{18}F is often implanted close to the target during the experiment, and as a result, it emits ionizing particles (positrons) and γ radiations that can produce an intense background on the detectors. The spectra measured are often cleaned up by selecting the good events in a time window, in a measurement between two detectors (e.g. silicon and microchannel plate assembly) or with the RF of the accelerator with a pulsed beam. This comment is valid for many of the experiments presented in this article.

To date, ten direct measurements of the ^{18}F(p, α)^{15}O reaction were carried out in five different laboratories, see Table 1. Fig. 3 shows the results of these experiments and the beam intensity required to induce 1 reaction per week (red curve). Beam intensity $>10^{12}$ pps is required to reach the left side of the Gamow window. Such a beam intensity is available nowhere in the world. The lowest energy measured is ≈250 keV, which is still in the right side of the Gamow window. The ^{18}F(p, α)^{15}O reaction shows particularly well the difficulty of measuring cross sections at low energy.

There are other experimental methods for direct measurement, but they have not yet been used to study the ^{18}F(p, α)^{15}O reaction. (i) The on-the-fly method can be carried out using electromagnetic recoil spectrometers [45–47], e.g. DRAGON located in TRIUMF Laboratory in Vancouver, Canada [48]. In these experiments, the beam is sent onto a windowless gas target and the recoil nucleus is selected with the spectrometer and identified with particle detectors, whereas the relatively intense beam is mostly rejected. To improve the signal-to-noise ratio, the measurement of the recoil nucleus is done in coincidence with the particle (or the γ ray) emitted in the reaction. (ii) Many direct measurements have been carried out at the LUNA laboratory (Laboratory for Underground Nuclear Astrophysics) [49,50], which is located at Gran Sasso laboratory in Italy. Several similar facilities are under development in the world [51–53]. These facilities are used for radiative capture reactions, e.g. (p,γ), where the γ background originated from cosmic rays is much reduced underground. (iii) The activation method [54] uses a target that is as pure as possible to induce nuclear reactions and to preserve the reaction products inside the target. If the reaction products are radioactive, the decay rates can be measured in a low background environment, in order to deduce the reaction cross section. This method has never been used for the ^{18}F(p, α)^{15}O reaction, although it is certainly technically possible, within certain limits. The reaction product, i.e. ^{15}O, has a relatively short lifetime ($t_{1/2}$ = 122 s) and no characteristic γ line. One way to measure it would be to extract ^{15}O from the target and

chemically purify it in less than 122 s (e.g. [55]), and then observe the 511 keV γ ray in coincidence with its associated β radiation. The sensitivity obviously depends on the extraction efficiency and on the background. (iv) Another version of the previous method is to measure the produced nuclei, stable or long-lived nuclei, trapped inside the target, using an Accelerator Mass Spectrometer (AMS) [56–58]. This method is not feasible in the case of the ^{18}F(p, α)^{15}O reaction because the reaction product, ^{15}O, decays to a daughter nucleus, ^{15}N, which is a natural contaminant very abundant in any sample.

Direct measurements are possible with a storage ring. A project to measure the ^{18}F(p, α)^{15}O reaction using the CRYRING ring at FAIR [59] is in preparation. The idea is to accumulate in the ring ^{18}F nuclei produced by fragmentation reactions, then decelerate them to the right energy and use a gaseous hydrogen jet target. The recoil nuclei ^{15}O will have a different trajectory and will be detected by a silicon detector placed after a magnetic dipole in the ring, probably in coincidence with the α particles measured with a detector placed just behind the target [60].

3.8. Limitations

The main limitation of direct-measurement experiments is the count rate, which is often very low, the cross section decreasing exponentially at low energy. Another difficulty is the energy of the emitted particles, which can be very low, that need to be detected. In the ^{18}F(p, α)^{15}O reaction, the important $J^\pi = 3/2^+$ resonances in ^{19}Ne are populated by proton capture with angular momentum $\ell = 0$, resulting in an isotropic angular distribution of the emitted α particles. For other resonances $\ell \neq 0$, the angular distribution must be taken into account. For example, for the resonance observed at 330 keV with $J^\pi = 3/2^-$, the angular distribution must follow the form $a + b\cos^2(\theta)$, with a and b being two free parameters [17,61]. The situation can be even more complicated with interferences between several resonances and between several reaction mechanisms, see Ref. [62]. An R matrix calculation code is often used to fit the data.

4. Predicting nuclear cross sections

In many cases, cross sections are so small that direct measurements are not possible in the Gamow window using the present experimental facilities. Theoretical models are used instead to predict their values at the lowest energies.

4.1. Empirical trends

It is possible to estimate the cross section of any reaction in the Gamow window with a precision of a factor of ≈100 without any prior knowledge of the reaction. This is because, in contrast to the cross section, the astrophysical $S(E)$ factor varies slowly with energy, and depends mainly on whether the reaction is nuclear or electromagnetic. As a first approximation, it can be assumed to be a constant in the energy range of the Gamow peak, $S(E) = S_G$. Fig. 4 (left) shows examples of S_G values measured for different nuclear reactions.

It is possible to calculate the penetrability $e^{-2\pi\eta}$ term with a higher accuracy, using the regular and irregular Coulomb functions, F and G [16–18]. These functions can be calculated numerically with, for instance, the GNU Scientific Library (GSL) [65]. Penetrability is also a function of the orbital angular momentum ℓ of the captured particle, since the centrifugal force produces another barrier in addition to the Coulomb barrier. In general, only the lowest angular momentum ($\ell = 0$) is considered in astrophysics. The following relation can be used

$$\sigma(E) \equiv \frac{S^*(E)}{E} P_{\ell=0}(E) \tag{8}$$

where $P_{\ell=0}(E)$ is the penetrability calculated numerically, and $S^*(E)$ the corrected value of the astrophysical S factor. A clearer picture is obtained with S^*_G, see Fig. 4 (right). One can see that the range of values on S^*_G is much reduced compared to S_G. The two categories of reactions, electromagnetic and nuclear, are well separated by a factor $\approx 10^5$. The spread of values within one category of reactions is a factor $\simeq 10^2$ only, whatever the mass of the nuclei. This spreading within one category is irreducible because it comes from many effects: the existence of different reaction mechanisms, contributions from different angular momenta, interferences between resonances, different level densities, etc. Despite the drastic reduction in the range of values, the uncertainty on S^*_G remains too large for many astrophysical models.

How can cross sections be accurately predicted at low energy? The first step towards this prediction is to propose nuclear reaction mechanisms.

4.2. Isolated resonance in the compound nucleus

The ^{18}F(p, α)^{15}O reaction can proceed through the formation of a quasi-stationary state in the compound nucleus (CN): $^{18}\mathrm{F} + p \rightarrow {}^{19}\mathrm{Ne}^*$, followed by the emission of an α particle: $^{19}\mathrm{Ne}^* \rightarrow {}^{15}\mathrm{O} + \alpha$. This is a two-steps process. Two matrix elements are needed to describe this process

$$\sigma(E) \propto |\langle \psi_{^{15}\mathrm{O}+\alpha} | H_2 | \psi_{^{19}\mathrm{Ne}^*} \rangle \langle \psi_{^{19}\mathrm{Ne}^*} | H_1 | \psi_{^{18}\mathrm{F}+p} \rangle|^2 \tag{9}$$

The two channels are coupled. The resolution of this quantum problem results in the Breit–Wigner (BW) formula [16,66,67], which is written

$$\sigma_{BW}(E) = \pi\lambda^2 \frac{2J_{^{19}\mathrm{Ne}^*} + 1}{(2J_p + 1)(2J_{^{18}\mathrm{F}} + 1)} \frac{\Gamma_p \Gamma_\alpha}{(E - E_r)^2 + (\Gamma/2)^2} \tag{10}$$

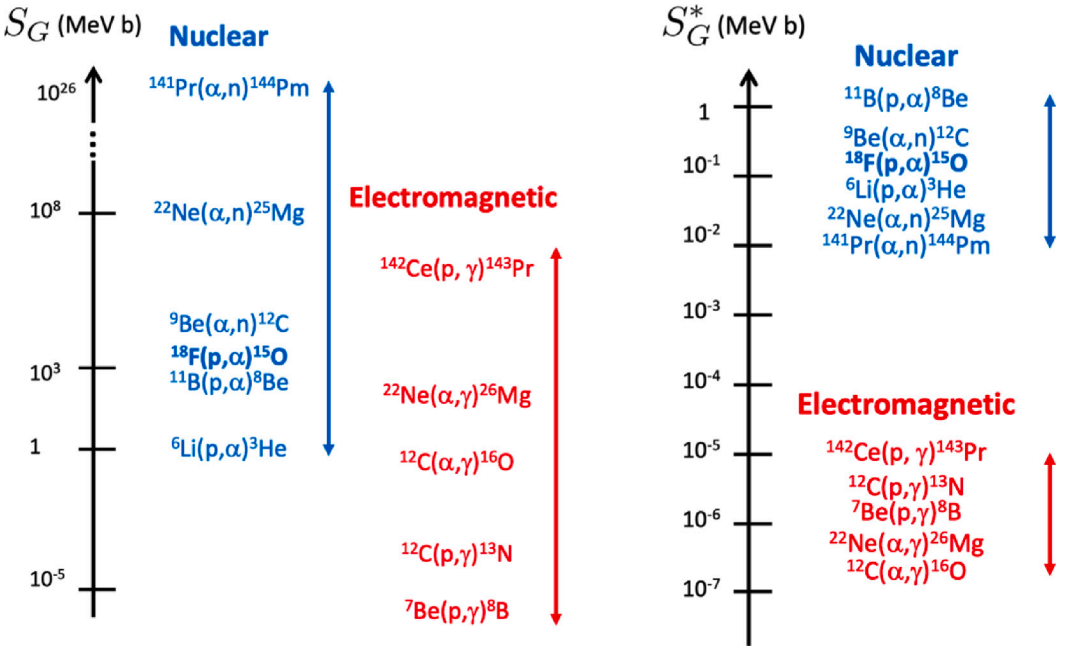

Fig. 4. (Left) Average astrophysical S factor (S_G) measured in the Gamow peak for different nuclear reactions [63,64]. These reactions can be classified into two categories, whether it is purely nuclear or whether it involves electromagnetic interaction. (Right) Corrected astrophysical S factors S^*_G (see text) using higher-accuracy penetrability function. This parameter has the advantage of dividing nuclear reactions into two clearly distinct categories and, within one category, the spreading of values is much reduced (factor ≈100) compared to the spreading shown with S_G. There is a factor ≈10^5 in magnitude between the nuclear and electromagnetic categories.

with λ the de Broglie wave-length, J are the spins and Γ_p, Γ_α and Γ are the partial widths and total width of the quasi-stationary state. The excitation function, i.e. cross section as a function of the incident energy, shows resonances as dramatic increases of the cross section at certain incident energies $E = E_r$ corresponding to excited states (the quasi-stationary states) of the CN. Accurate excitation function can be calculated using the R-matrix formalism, see Section 5.2. Different computer codes are available to calculate cross sections or to analyze data, e.g. the AZURE code [68,69]. To calculate the ^{18}F(p, α)^{15}O cross section at low energy, we need to know the properties (spin, width, resonance energy) of all the excited states of ^{19}Ne above the proton emission threshold. These properties must therefore be either measured, or predicted theoretically.

Fig. 5 shows the level scheme of ^{19}Ne with the most important states for the calculation of the ^{18}F(p, α)^{15}O reaction rate. Many other excited states exist but are not represented in this figure, because of their lesser importance, and also because they are not known in ^{19}Ne although they are known in the mirror nucleus ^{19}F. The two resonances at 665 keV and 332 keV are clearly visible in Fig. 3.

4.3. Interferences between resonances

The total cross section is not always the sum of several BW resonances. Interferences can also occur between resonances of the same spin and parity. Such interferences result sometimes in weaker cross sections (negative interference). In the case of the ^{18}F(p, α)^{15}O reaction, the cross section is uncertain by a factor of up to 10 at low energies from possible interferences between several $3/2^+$ resonances and between two $1/2^+$ resonances. Without going into too much detail, Fig. 6 illustrates the possible effects of interferences between three $3/2^+$ resonances. Note that the rate of the reaction is less uncertain, since it is the integral of the cross section.

In principle, the Trojan Horse Method (see Section 8) could be used to constrain the sign of interferences, but this is impractical due to the limited energy resolution of these measurements. The only way to determine the sign of the interference is to measure the cross-section directly. Sometimes, the sign of the interferences can be constrained from measurements at energies above the Gamow window, see example in Fig. 6 and Ref. [39].

4.4. Direct radiative capture

Direct-radiative-capture reaction can be seen as a perturbation to the Coulomb scattering. The direct-radiative-capture reaction is an entirely electromagnetic process [72]. Reactions proceed through electromagnetic interaction directly to the final state: $A + x \rightarrow \gamma + B^*$, with B^* built as $A + x$. The extra energy given by the Q-value of the reaction plus the kinetic energy of the

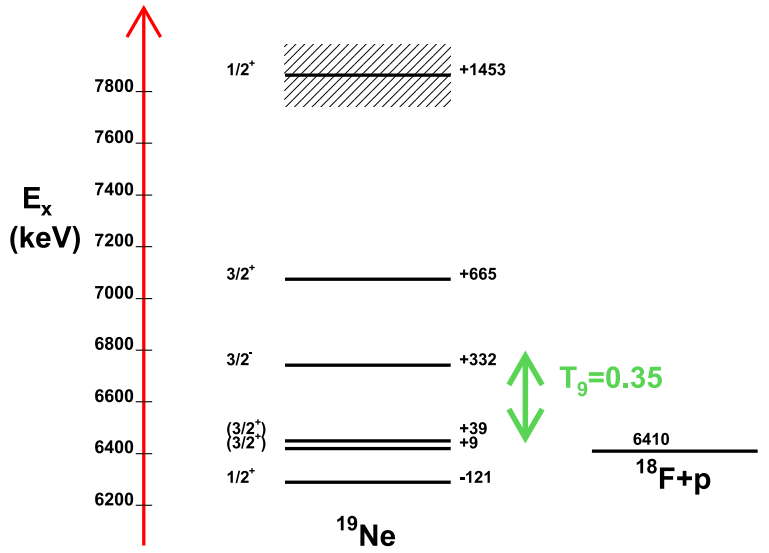

Fig. 5. Simplified level diagram showing several important states in ^{19}Ne for the calculation of the ^{18}F(p, α)^{15}O reaction rate. *Source:* From Ref. [14,70,71].

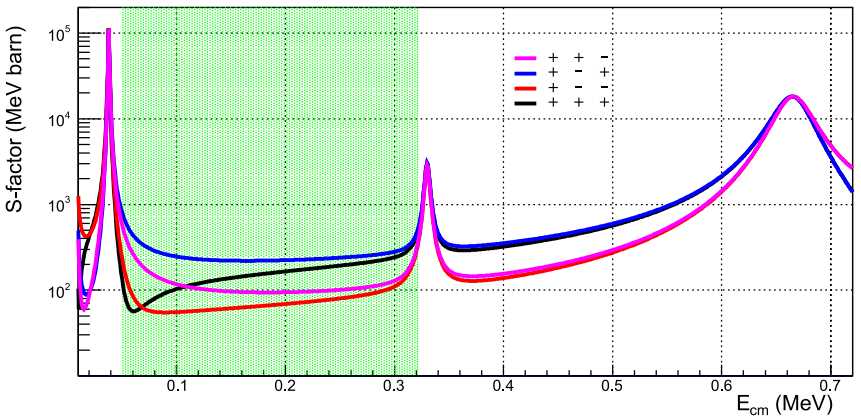

Fig. 6. The astrophysical S factor of the ^{18}F(p, α)^{15}O reaction is calculated as a function of the c.m. energy. In this simulation, the three $E_r = 9$ keV, 39 keV and 665 keV $3/2^+$ resonances are considered. The signs of the interferences are changed and the results are presented with different colors. The three signs are given for the three $3/2^+$ resonances, The (+) sign means that the amplitude of probability is positive, whereas a (−) sign means this amplitude is negative. The green area corresponds to the Gamow window of novae explosions. In this energy range, the astrophysical S factor can vary by a factor up to 10 as a result of interferences.

incident particle is transported by the electromagnetic radiation. The cross section is described by a single matrix element,

$$\sigma(E) \propto | \langle \psi_{B^*+\gamma} \mid M_\lambda \mid \psi_{A+x} \rangle |^2 \tag{11}$$

with M_λ the electromagnetic operator [18]. In general, the highest contribution comes from $E1$ transitions, with $M_{\lambda=1} = rY^{(1)}(\theta, \phi)$, since $E1$-transitions are the fastest electromagnetic transitions. It follows

$$\sigma(E) \propto \left| \int_0^\infty u_f(r)\ r\ u_i(r) dr \right|^2 \tag{12}$$

where $u_i(r)$ is the incident particle scattering wave function in the entrance channel, and $u_f(r)$ is the radial part of the nucleus B formed by $A + x$, see an example of calculation in Ref. [73]. This direct-radiative-capture process is a non-resonant process. Different computer codes can be used to calculate cross sections, e.g. the RADCAP code [74,75].

Obviously, this reaction mechanism does not apply directly to the ^{18}F(p, α)^{15}O reaction since no γ is emitted. However, we can estimate the direct capture process populating unbound excited states of ^{19}Ne*, see Ref. [14], decaying by the emission of an α particle: ^{18}F(p, γ)^{19}Ne*(α)^{15}O. In the Gamow window of the ^{18}F(p, α)^{15}O reaction, this reaction mechanism contributes less than one per hundred thousand to the total cross section, see Fig. 7.

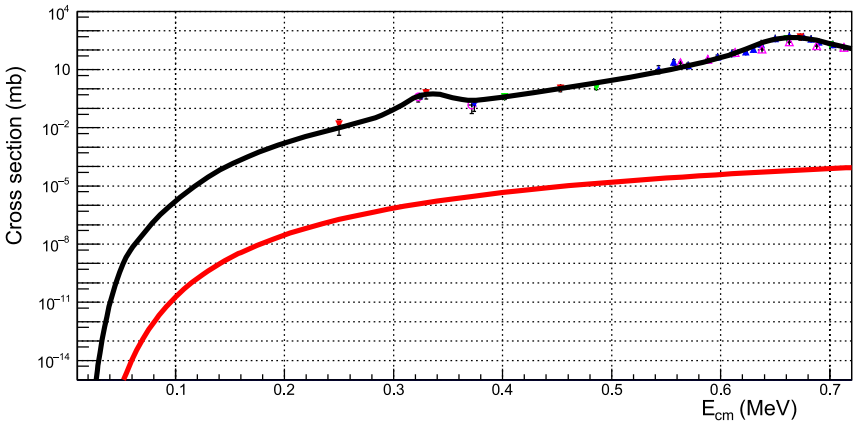

Fig. 7. The $^{18}F(p,\alpha)^{15}O$ reaction cross section is shown as a function of the energy in c.m. The points are measured values and the black line is a fit on the experimental points. The red line was calculated with the RADCAP code assuming a direct radiative capture mechanism, i.e. $^{18}F(p,\gamma)^{19}Ne^{*}(\alpha)^{15}O$. The latter reaction mechanism is negligible compared with the contributions of resonances in the compound nucleus.

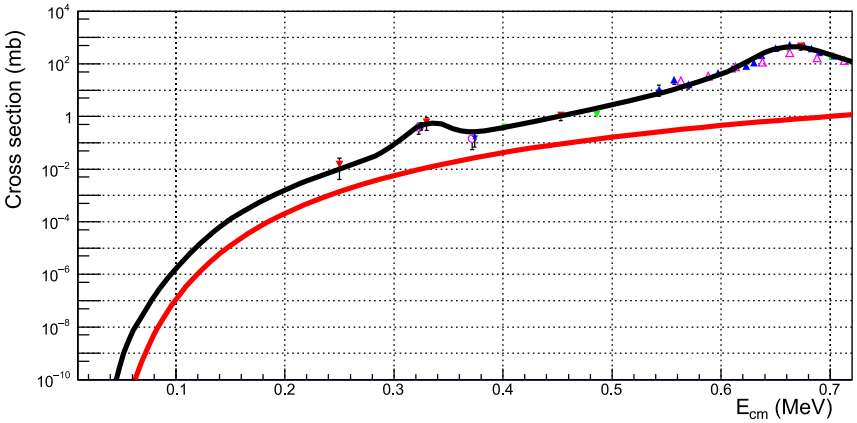

Fig. 8. The $^{18}F(p,\alpha)^{15}O$ reaction cross section is shown as a function of the energy in c.m. The points are measured values and the black line is a fit on the experimental points. The red line was calculated with the FRESCO code assuming a direct nuclear transfer mechanism and pure $^{18}F = ^{14}N + \alpha$ and $^{15}O = ^{14}N + p$ configurations. The latter reaction mechanism is negligible compared with the contributions of resonances in the compound nucleus.

4.5. Direct particle transfer

Reactions can proceed through the nuclear interaction directly to the final state. For example, in Ref. [62], it is shown that the ground state of ^{18}O is well described as an $\alpha + ^{14}C$ cluster structure, and the $^{18}O(p,\alpha)^{15}N$ reaction can be visualized as a ^{14}C nucleus picking up a proton, leaving the α cluster. In general, the corresponding astrophysical S factor varies gently with energy, but see the $^{8}Li(\alpha,n)^{11}B$ counterexample in Ref. [76].

In the case of the $^{18}F(p,\alpha)^{15}O$ reaction, the direct proton pickup cross section can be calculated by assuming $^{18}F = ^{14}N + \alpha$ and $^{15}O = ^{14}N + p$. The cross section is described by a single matrix element

$$\sigma(E) \propto | \langle \psi_{^{15}O} \mid V \mid \psi_{^{14}N+p} \rangle |^2 \tag{13}$$

where V is the nuclear potential. The model called *Distorted Wave Born Approximation* (DWBA) can be used to predict cross sections, see Section 7. Several computer codes are available to calculate the direct particle-transfer cross sections, the FRESCO code [77,78] for example. In the case of the $^{18}F(p,\alpha)^{15}O$ reaction, this mechanism is found negligible at astrophysical energies, see Fig. 8.

4.6. Indirect measurements

The determination of astrophysical cross sections using nuclear models requires the measurement of some parameters, i.e. spectroscopic properties. This way of determining astrophysical cross sections is called *indirect measurements* or *indirect methods*, see Ref. [79]. Several experimental methods can be used to determine these parameters: elastic scattering, $^{18}F(p,p)^{18}F$, knock-out reaction, $^{20}Ne(p,2p)^{19}Ne^{*}$, transfer reaction, $^{18}F(d,n)^{19}Ne^{*}$, fusion–evaporation reaction, $^{20}Ne + p \rightarrow ^{21}Na^{*} \rightarrow ^{19}Ne^{*} + p + n$, beta-delayed particle emission etc. In present article, we have chosen to present the experimental techniques that have been used to

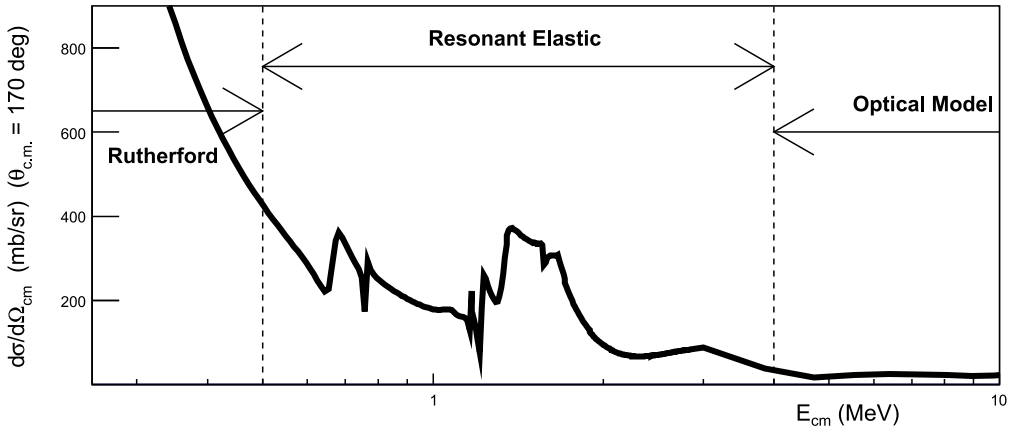

Fig. 9. Excitation function of the ^{18}F$(p,p)^{18}$F elastic scattering reaction calculated with R matrix, HSFB and DWBA formalisms. Depending on energy, different reaction mechanisms dominate: Rutherford scattering at very low energy, resonant elastic scattering around 1 MeV, HSFB and nuclear-optical model at higher energy.

determine the ^{18}F$(p,\alpha)^{15}$O reaction rate.

5. Resonant elastic scattering

5.1. Principle

The ^{18}F$(p,p)^{18}$F elastic scattering reaction occurs at all incident energies through different reaction mechanisms. Three different energy ranges can be considered, see Fig. 9. The domain of very low energies, $E_{c.m.} \lesssim 0.5$ MeV, is dominated by the Rutherford scattering. At energies $E_{c.m.} \gtrsim 4$ MeV, the cross section is fairly monotonous, the nuclear-optical model can be used to calculate the cross section. At intermediate energies ($0.5 \lesssim E_{c.m.} \lesssim 4$ MeV), resonances are observed. The intermediate energy domain is particularly interesting for nuclear spectroscopy and astrophysics.

According to the Rutherford elastic scattering formula, the differential cross section varies inversely proportional to the square of the energy. Deviations from this law are observed at intermediate energy. For example, the excitation function of the ^{14}N$(p,p)^{14}$N elastic scattering reaction measured at the angle of $\theta^{c.m.} = 180°$ is shown in Fig. 10 (top). Its cross section follows very well the Rutherford elastic scattering formula except for energies close to $E^{lab} \simeq 1.06$ MeV (in direct kinematics) where an anomaly is observed. Indeed, the energy of the anomaly, at $E^{c.m.} = 0.985$ MeV above the reaction threshold ^{14}N + p ($S_p = 7.297$ MeV), matches perfectly to the excitation energy $E_x = S_p + E^{c.m.} = 8.284$ MeV of the $3/2^+$ excited state in the ^{15}O compound nucleus. Therefore, two different reaction mechanisms should be invoked to explain the measured cross section. On the one hand (Fig. 10, bottom left), the two nuclei undergo Coulomb repulsion: they don't "touch" each other. On the other hand (Fig. 10, bottom right), the two nuclei merge and fuse to the compound nucleus ^{15}O which decays back to the entrance channel (elastic scattering). An anomaly (resonance) is observed when the incident energy matches the energy of a compound-nucleus excited state. This reaction mechanism is called *Resonant Elastic Scattering (RES)*. *RES* cross sections are generally high, typically several tens or hundreds of mbarn/sr. *RES* can be used for astrophysics studies, by measuring the properties of the compound-nucleus resonances.

Energy. The resonance energies, E_r, can be determined from the energies of the scattering anomalies. If the measurement is performed in inverse kinematics, the *c.m.* energy at the interaction point (reaction vertex) can be determined from the measured energy of the scattered particles in *lab*, see Fig. 11. Indeed, the energy of the scattered particles in *lab* is related to the *c.m.* energy at the reaction vertex by

$$E^{c.m.} = \frac{1}{4}\,\frac{1}{\cos^2(\theta^{lab})}\,\frac{m_p + m_t}{m_p}\,E^{lab} \tag{14}$$

with m_p and m_t the projectile and target mass. The *c.m.* angle is related to the *lab* angle by

$$\theta^{c.m.} = 180° - 2\,\theta^{lab} \tag{15}$$

with θ^{lab} in degrees.

Spin. The two reaction mechanisms, Rutherford scattering and compound nucleus formation, operate simultaneously and are indistinguishable. Amplitudes of probabilities should be added (instead of cross sections), resulting into interferences between the two contributions, see Fig. 10. Fig. 12 shows that the shape of resonances depends on the spin and parity of states, and so, resonances shape analysis can be used to constrain spin and parity of excited states. Angular distributions can also be used to determine the spin of states and they are useful for distinguishing between several overlapping resonances, see for example Ref. [81].
Widths. The widths and amplitudes of the measured scattering anomalies in the excitation function can be used to determine total width Γ_T and partial widths Γ_p, Γ_α, ... of resonances.

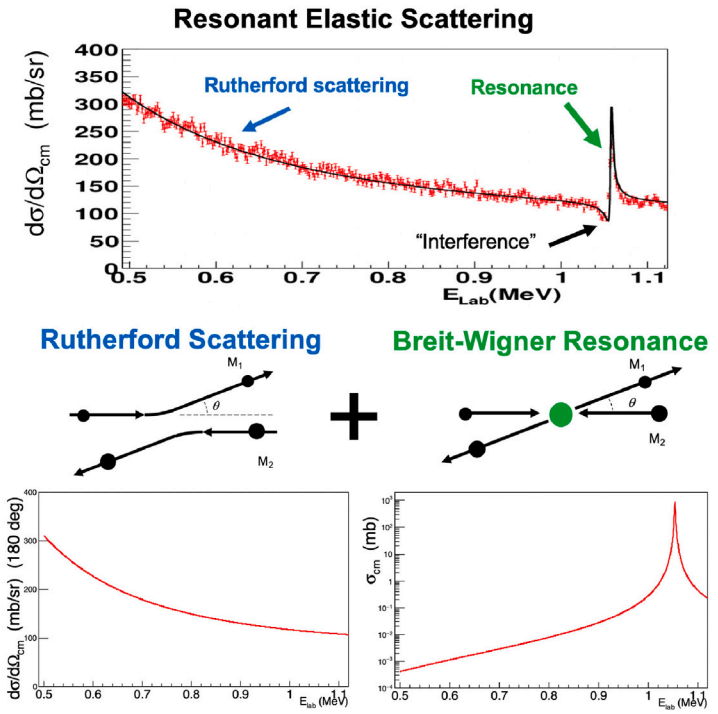

Fig. 10. Top: Excitation function of the ^{14}N(p, p)^{14}N reaction measured at 180 ° *c.m.* angle, as a function of the incident energy of the proton in the laboratory in direct kinematics, from Ref. [80]. The data follow very well the Rutherford elastic scattering formula (black line on the left side), except at energies $E^{lab} \simeq 1.06$ MeV where an anomaly is observed. It is interpreted as a resonance in the ^{15}O compound-nucleus. Bottom left: Rutherford elastic scattering. Bottom right: Resonance in the compound nucleus decaying to the elastic scattering channel.

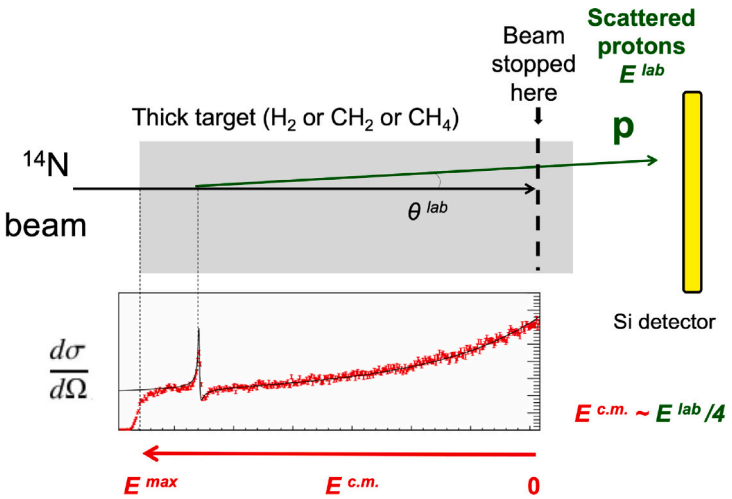

Fig. 11. This drawing illustrates the measurement of the ^{14}N(p, p)^{14}N excitation function in the *thick target inverse kinematics technique*. The center-of-mass energy at the reaction vertex is determined from the measured energy of the scattered particles. In the case of proton scattering reactions at forward angles, $E^{c.m.}$(vertex) $\approx \frac{1}{4} E^{lab}$(proton). The detected proton energies are a little less than the scattered energies because of energy loss in the target, which needs to be taken into account in the analysis. In the measured spectrum, the resonance observed in the left side of the spectrum has a width of 3.6 keV.

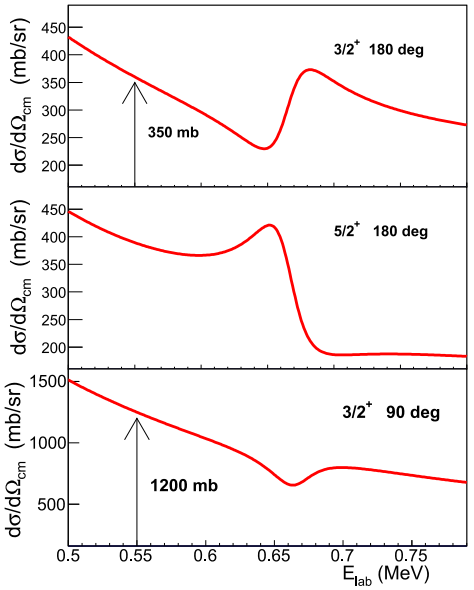

Fig. 12. Excitation functions of the ^{18}F$(p,p)^{18}$F elastic scattering reaction are calculated using the same properties of the state in the ^{19}Ne compound nucleus ($E_r = 0.6647$ MeV, $\Gamma_p = 15.2$ keV and $\Gamma_\alpha = 23.8$ keV). Top: $J^\pi = 3/2^+$ and $\theta^{c.m.} = 180$ deg. Middle: $J^\pi = 5/2^+$ and $\theta^{c.m.} = 180$ deg. Bottom: $J^\pi = 3/2^+$ and $\theta^{c.m.} = 90$ deg. Resonance shape analysis can be used to constrain spin and parity of the resonant states. Note that the larger is the angle the larger is the Rutherford contribution (1200 mb at 90 deg instead of 350 mb at 180 deg). In general, resonances are best seen at $\theta^{c.m.} = 180$ deg.

5.2. Theory

Here, we present a simple and heuristic example, the case of the s-wave scattering on a square-well potential of a spinless neutron, inspired by Ref. [82]. Let us assume the potential between the target nucleus and the neutron to be a square well with a potential depth V_0 and a radius $r = a$. The potential goes to infinity at $r = 0$, and it is zero from $r = a$ out to $r = \infty$. The radial part of the Schrödinger equation

$$-\frac{\hbar^2}{2\mu}\frac{d^2\phi(r)}{dr^2} + V_0\,\phi(r) = E\,\phi(r) \tag{16}$$

should be solved. In the external region ($r > a$), the general solution is

$$\phi(r) = B\,[e^{-ikr} - e^{2i\delta}e^{+ikr}] \tag{17}$$

where B is a constant, $k = \sqrt{2\mu(|E|)}/\hbar$, and δ is called the phase shift. It is possible to show (see Ref. [18]) that the cross section of the elastic scattering reaction is a function of δ

$$\sigma(E) = 4\,\frac{\pi}{k^2}\sin^2(\delta). \tag{18}$$

In the internal region ($r < a$), the solution is

$$\phi(r) = A\,\sin(K\,r) \tag{19}$$

where A is a constant and $K = \sqrt{2\mu(E+V_0)}/\hbar$. The function $\phi(r)$ and its derivative should be continuous at $r = a$, this gives

$$\delta = \arctan[\frac{k}{K}\tan(Ka)] - ka \tag{20}$$

that can be rewritten

$$\delta = \arctan[k\frac{\phi(a)}{\phi(a)'}] - ka. \tag{21}$$

The Schrödinger equation can be solved for bound states by imposing the following condition

$$\frac{d\mathrm{X}_\lambda}{dr}(r=a) = 0. \tag{22}$$

That gives

$$\mathrm{X}_\lambda(r) = (\frac{2}{a})^{1/2}\,\sin(K_\lambda\,r) \tag{23}$$

with

$$K_\lambda = (\lambda + \frac{1}{2})\,\frac{\pi}{a}. \tag{24}$$

These bound states form a complete set of states. It is possible to rewrite the quasi-bound internal wave function $\phi(r)$ in this base

$$\phi(r) = \sum_{\lambda} C_{\lambda} \, \mathrm{X}_{\lambda} \, (r) \tag{25}$$

where the coefficients C_{λ} can be obtained with the relation

$$C_{\lambda} = \int_0^a \mathrm{X}^*_{\lambda}(r) \; \phi(r) \; dr. \tag{26}$$

Using the Schrödinger equation for $\phi(r)$ and $\mathrm{X}_{\lambda}(r)$, one gets

$$-\frac{\hbar^2}{2\mu}\{\frac{d^2\phi}{dr^2}\mathrm{X}^*_{\lambda} - \phi\frac{d^2\mathrm{X}^*_{\lambda}}{dr^2}\} = (E - E_{\lambda})\phi\mathrm{X}^*_{\lambda} \tag{27}$$

which gives after integration

$$-\frac{\hbar^2}{2\mu}\,[\,\frac{d\phi}{dr}\mathrm{X}^*_{\lambda} - \phi\frac{d\mathrm{X}^*_{\lambda}}{dr}]_0^a \;=\; (E - E_{\lambda}) \int_0^a \phi\mathrm{X}^*_{\lambda} \, dr \tag{28}$$

which can be used in Eq. (26), giving

$$C_{\lambda} = \frac{\hbar^2/2\mu}{E_{\lambda} - E}\mathrm{X}^*_{\lambda}(a) \; \phi'(a). \tag{29}$$

Using this expression in Eq. (25), one gets

$$\frac{a \; \phi'(a)}{\phi(a)} = \frac{1}{\sum_{\lambda} \frac{\hbar^2/\mu a^2}{E_{\lambda} - E}} = \frac{1}{R} \tag{30}$$

where R is the R function, i.e. $\mathrm{R} = \sum_{\lambda} \frac{\gamma^2}{E_{\lambda} - E}$ with $\gamma^2 = \hbar^2/\mu a^2$ the reduced width.

Eq. (30) can be used in Eq. (21). In the approximation of a single term in λ, i.e. $R \;=\; \frac{\gamma^2}{E_{\lambda} - E}$, it gives

$$4 \, \sin^2(\delta) \;=\; \left| 2 \, \sin(ka) e^{ika} - \frac{\Gamma}{(E_{\lambda} - E) - i\frac{\Gamma}{2}} \right|^2 \tag{31}$$

with

$$\Gamma \;=\; 2 \, \gamma^2 \, ka \tag{32}$$

being the width of the resonance, and for the cross section (Eq. (18))

$$\sigma(E) = \frac{\pi}{k^2} \quad \left| 2 \, \sin(ka) e^{ika} - \frac{\Gamma}{(E_{\lambda} - E) - i\frac{\Gamma}{2}} \right|^2 \tag{33}$$

There are two terms in this expression. If the second term is neglected, then $\sigma(E) \to 4\pi a^2$ when k goes to zero, which is the geometric cross section. The first term corresponds to the elastic scattering onto a hard sphere (for which the potential is infinite for $r < a$ and zero for $r > a$). The second term corresponds to the Breit–Wigner resonance. The two terms may interfere since the two amplitudes are added before putting the sum to the square. Thus, the shape of the cross-section anomalies depends on the properties of the compound-nucleus states.

In the more general case, when there are several resonances involved, different spins and several reaction channels, the final expression is similar to the one obtained here, the R function becomes the R matrix. A detailed description of this formalism can be found in other articles, see for example Ref. [83]. Several codes can be used to calculate the scattering cross section according to the phenomenological R-matrix formalism, e.g. AZURE [68,69]. The R-matrix formalism can be used to predict, or to fit, the measured elastic scattering excitation function.

5.3. Projectile

The calculation of the ^{18}F$(p, \alpha)^{15}$O reaction cross section requires knowledge of the ^{19}Ne states properties. These can be partially obtained with the ^{18}F$(p, p)^{18}$F reaction, or with the ^{15}O$(\alpha, \alpha)^{15}$O reaction. These reactions can be measured in inverse kinematics with radioactive beams, e.g. H(^{18}F, $p)^{18}$F. Beam intensities as low as 10^4 pps can be used, inducing ≈10 counts per day in a 10 keV peak. To study the ^{18}F$(p, \alpha)^{15}$O reaction, it is also important to consider the ^{15}N$(\alpha, \alpha)^{15}$N mirror elastic scattering reaction, see Ref. [84].

5.4. Incident energy

To measure the excitation energy, E_x, of the important states in astrophysics, the energy of the incident beam must be adjusted to reach the *c.m.* energy $E^{c.m.} = E_x - S$ where S is the particle emission threshold. This typically gives 0.1–5 MeV proton or ^{4}He beams, or 0.1–5 MeV/u in inverse kinematics. In general, it is a bad idea to use higher energy beams combined with thick targets, as other reaction channels open up with the emission of several particles, especially inelastic scattering, polluting the measurement.

5.5. Target

All kinds of targets can be used: solid, e.g. $(CH_2)_n$, or gaseous, e.g. ^{4}He, thin (<1 μm) or thick (≈1 mm), composed of heavy or light elements, depending on the reaction.

5.6. Experimental setup

RES measurements are carried out using mainly two different types of experimental setup.

1. Either a thin target is used, and the energy of the incident beam is changed to measure the excitation function in small energy steps. For example, the ^{18}F$(p,p)^{18}$F reaction was studied at Holifield Radioactive Ion Beam Facility (ORNL) by Bardayan et al. [38] with the experimental setup shown in Fig. 2. They used a 0.39 μm thin polypropylene target and a ^{18}F beam accelerated to different energies, from 10 to 14 MeV. Since the beam was polluted by ^{18}O, a gas ionization chamber was used to identify the heavy recoil nucleus, event by event, see Fig. 13(a). The particles of the beam, which have not interacted with the target, were stopped in a material placed at zero degrees downstream the target. The emitted light particles, proton after the elastic scattering or alpha after the ^{1}H(^{18}F, α)^{15}O reaction, were detected at forward angles with a silicon detector array (SIDAR), in coincidence with the recoil ion. Results of the simultaneous elastic scattering and direct ^{18}F(p, α)^{15}O measurements are shown in Fig. 13(b). By measuring these two reactions simultaneously, it was possible to determine the properties of one important state for calculating the rate of the reaction.
2. Another option is to use a thick target. The measurement is made in inverse kinematics. The experiment works on the principle that the incident particles lose energy inside the thick target, making it possible to measure the excitation function over a wide energy range in a single measurement [85,86]. The scattered light particles lose very little energy in the thick target, because of their low mass and low charge, and escape from it. This *thick target inverse kinematics* (TTIK) technique (see Ref. [87] for the first experiment with thick target, [88] for the first experiment in inverse kinematics, and [89] with radioactive beam) is well suited to relatively low-intensity beams.
   The H(^{18}F, p)^{18}F reaction was measured several times with the TTIK technique. In the experiment performed at GANIL by Mountford et al. [44], a ^{18}F beam was produced at the SPIRAL1 facility with an intensity of 2×10^4 pps. The beam was first accelerated to 4 MeV/u, then it was electron stripped with a thin carbon foil to select a pure beam of $^{18}F^{9+}$ with a magnetic spectrometer, and slowed down to 2.3 MeV/u using a 5.5 μm gold degrader foil placed just upstream of the thick target. The slow beam was sent onto a 55 μm polypropylene $(CH_2)_n$ target, thick enough to stop the beam. The particles emitted in the H(^{18}F, p)^{18}F and H(^{18}F, α)^{15}O reactions were measured at forward angles with a Double Sided Silicon Strip Detector (DSSSD) located downstream of the target, see Fig. 14. The two reactions were measured simultaneously in the $E^{c.m.} = 0.5$–1.9 MeV energy range. The identification of the detected particles was based on the time of flight measured between a microchannel plate (MCP) detector located upstream of the target and the DSSSD.
   The ^{4}He(^{15}O, α)^{15}O reaction was also measured several times with the TTIK technique. The first attempt was made at the CRC Louvain-la-Neuve (LLN), Belgium, with a 15 mm thick helium gas cell at a 100 mbar pressure, see Ref. [90]. A second experiment was done at LLN with a 9.28×10^6 pps ^{15}O radioactive beam [91] and a 9-cm thick helium gas cell at 300 mbar. Another experiment was done with a 2×10^4 pps ^{15}O beam, ≈99% purity, produced at the Laboratory Nazionali di Legnero, Italy, and with a thick ^{4}He gas target (≈0.5 m and 467 mbar) separated by Havar window from the vacuum beam line [28]. In the latter experiment, the scattered α particles were measured with a DSSSD silicon detector placed inside the gas chamber, see Fig. 15. Particles identification was based on time-of-flight between the PPAC detectors and the silicon detector. Moreover, time-of-flight measurement allowed to separate inelastic scattering reactions from elastic scattering reactions. An energy resolution of 20–30 keV has been achieved in the *c.m.* frame. See also Ref. [92] for the ^{4}He(^{15}N, α)^{15}N mirror reaction.

5.7. Energy resolution

In the *TTIK* technique, according to Eqs. (14) and (15), if $\theta^{lab} = 0°$ and $m_t/m_p < 1$, then $E^{c.m.} \approx \frac{1}{4} E^{lab}$. The energy resolution in the *c.m.* is about 4 times smaller than the resolution in the *lab*, so it is possible to obtain high-energy resolution spectra, even with thick targets. The energy resolution of the scattered-protons spectrum can be estimated with $\sigma^{lab} = \sqrt{\sigma_{det}^2 + \sigma_\theta^2 + \sigma_{strag}^2}$, where σ_{det} is the energy resolution of the detector, σ_{strag} is the energy straggling in the target (including beam angle and energy resolution), and σ_θ is the energy resolution due to the uncertainty $d\theta$ in both the detection angle and the beam angle. In inverse kinematics, it can be derived that $\sigma_\theta = 2\tan(\theta^{lab})E^{lab}d\theta$. Therefore, the degradation of the energy resolution is minimal when $\theta^{lab} = 0°$. For this reason, and for maximizing the ratio between the nuclear (compound nucleus) and the Coulomb contribution in the differential cross section (see Fig. 12), the scattered protons are generally measured at forward angles in *lab*. With a high energy resolution silicon detector (FWHM ≈ 15 keV), one can get $\sigma^{c.m.} \approx \sigma^{lab}/4 \approx 4$ keV (if $\sigma_{strag} \ll \sigma_{det}$), see Fig. 11. Note also that the energy resolution varies as the square root of the energy, a resolution measured with an alpha source at 5 MeV will have to be doubled at an energy of 20 MeV.

In principle, it is possible to obtain an energy resolution much better than 1 keV by using a thin target and well-defined beam energy (using electrostatic accelerator). In 1992, Wüstenbeeker et al. [96] published the results of an ultra high energy resolution *RES* experiment. The goal of this experiment was to study the properties of the ^{8}Be ground state, an important state in nuclear

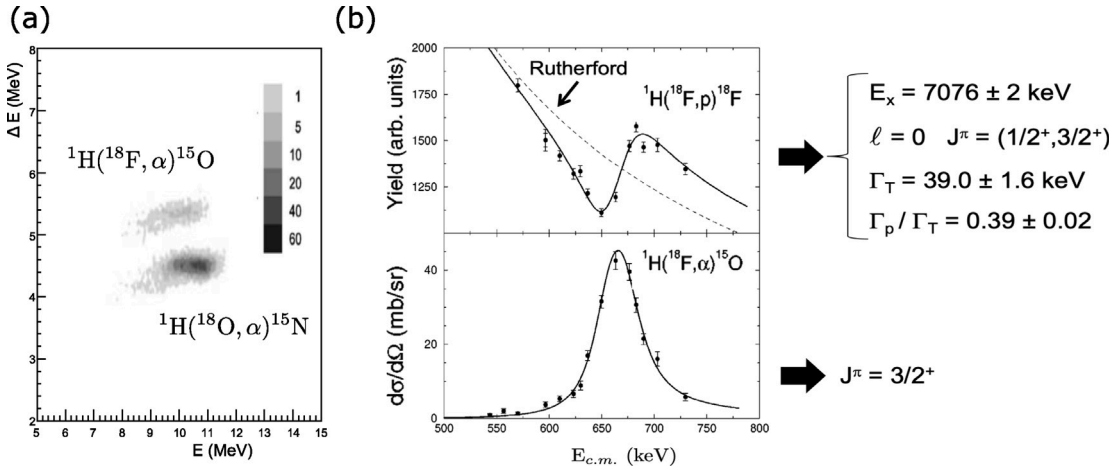

Fig. 13. The ^{1}H(^{18}F, p)^{18}F and ^{1}H(^{18}F, α)^{15}O reactions were measured simultaneously in the same experiment at ORNL [38,93,94]. A ^{18}F beam and a thin polypropylene target were used. The ^{18}F recoil nuclei were identified, event by event, with a gas ionization chamber, see Fig. 1. The light emitted particles, proton or alpha, and ^{15}O nuclei were detected in coincidence by a silicon detector array (SIDAR). (a) The energy lost in the first two anodes is shown in relation to the total energy deposited in the gaz ionization counter. This data was obtained under conditions necessitating a proton detection by SIDAR. This plot effectively differentiated between the scattering events of ^{18}F and ^{18}O. (b) *R*-matrix formalism was used to fit the two measured excitation functions simultaneously.

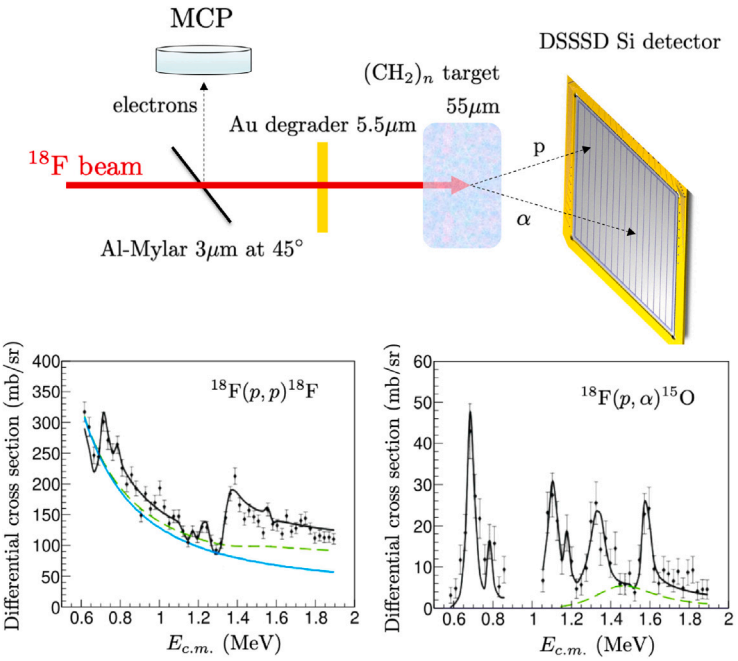

Fig. 14. (Top) Schematic layout of the experimental setup of Ref. [44]. The ^{18}F beam was stopped in a thick $(CH_2)_n$ polymer target. Particles were detected in a DSSSD detector located downstream the target (172° to 180° in the center of mass). The identification of the particles (protons and α-particles) was based on the time difference between beam ions traversing through the MCP detector and particles being detected in the DSSSD. (Bottom) The *R*-matrix formalism was used to fit the two measured ^{1}H(^{18}F, p)^{18}F and ^{1}H(^{18}F, α)^{15}O excitation functions simultaneously. The result is shown by the solid black line, calculated for the angle of 176° in the center of mass. The contribution of a new 1/2$^+$ broad resonance is shown in dashed green and the Rutherford scattering in pale blue.

astrophysics involved in the triple alpha reaction ^{4}He($2\alpha, \gamma$)^{12}C. They measured the $\alpha - \alpha$ scattering in kinematic coincidence for the angle pairs 45°/45° and 30°/60° using crossing beams technique. They achieved an outstanding resolution of 26 eV and observed that the nuclear resonance of the ^{8}Be ground state is divided into 2 main peaks separated by ~200 eV, see Fig. 16. This split has its origin in atomic physics, it comes from the fact that the ^{8}Be compound nucleus was produced with different charge states, each corresponding to different masses of the ion. The difference is admittedly small, but the resolution of the experiment was sufficient to observe this difference. The alpha width was measured at $\Gamma_\alpha = 11.14 \pm 0.50$ eV. In practice, high energy resolution spectra are difficult to achieve, as high intensity and long beam times are required. Indeed, the narrower the resonance is, the thinner the

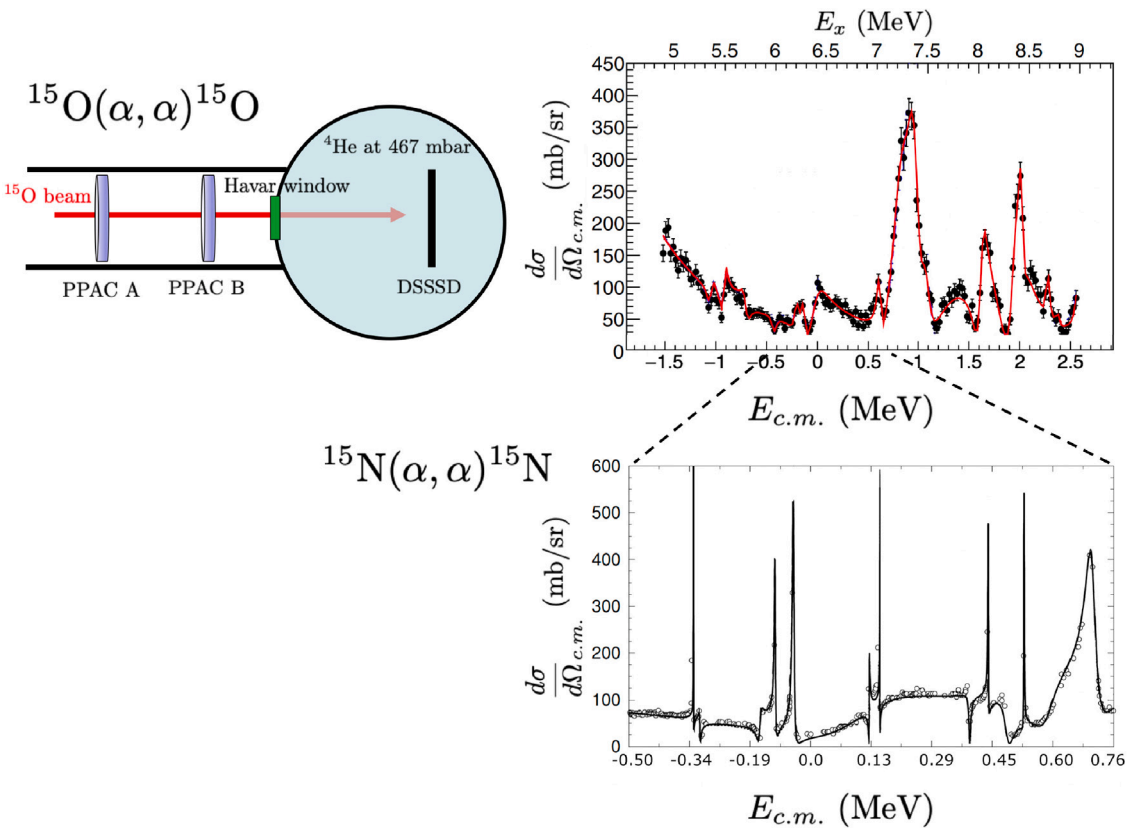

Fig. 15. (Top left) Schematic of the experimental apparatus used in Ref. [28]. In this experiment, the ^{4}He(^{15}O, α)^{15}O reaction was measured with a radioactive ^{15}O beam and a thick ^{4}He gas target. The scattered particles were measured with a DSSSD detector placed inside the gas chamber. Inelastic scattering reactions were separated from elastic scattering reactions with the time-of-flight measurement between PPAC detectors and the silicon detector. (Top right) The *R*-matrix formalism was used to fit the measured excitation function. (Bottom) The $^{15}N(\alpha,\alpha)^{15}N$ mirror reaction is shown for comparison. The experiment was performed in direct kinematics with a high energy resolution (0.1% of the beam energy) [84,95]. This excitation function corresponds to a small portion of the ^{4}He(^{15}O, α)^{15}O spectrum shown above. At this energy resolution, numerous narrow resonances can be observed.

effective target thickness is, and the lower the count rate is.

5.8. Data analysis

Several effects have to be taken into account in the analysis of *RES* experiments, especially in the *TTIK* technique.

Identification of scattered particles. The beam may not be pure, the target either, and different reactions are possible. The scattered particles must be identified by the usual means, with a $\Delta E - E$ matrix or an E versus time-of-flight matrix, see for example Fig. 17.

Energy loss correction. In the TTIK technique, the measured energies of the scattered particles have to be corrected for the energy lost inside the target, see Fig. 18(a).

Effective target thickness. Using a constant cross section, simulations show that the number of detected particles is not constant, it increases with the energy of the detected particles, as illustrated in Fig. 18(b). The effective target thickness increases with the energy of the detected particles. The differential cross section of the measured elastic scattering reaction can be calculated with

$$\left(\frac{d\sigma}{d\Omega}\right)^{c.m.} = \frac{\frac{dN_p}{dE}}{N_{\text{beam}}\frac{dN_{\text{target}}}{dE}d\Omega^{c.m.}} \tag{34}$$

where N_{beam} is the total number of incident ions, $d\Omega^{c.m.}$ is the solid angle of the detector in $c.m.$, with $d\Omega^{c.m.} = 4\cos(\theta^{lab})d\Omega^{lab}$, $\frac{dN_p}{dE}$ is the number of scattered protons or α particles per $E^{c.m.}$ unit (number of counts per bin in the center-of-mass spectrum), $\frac{dN_{\text{target}}}{dE}$ is the energy-dependent number of target atoms per $E^{c.m.}$ unit. The latter depends on the energy lost by the beam ions as a function of their position inside the target. It is usually obtained from a simulation code.

Background subtraction. The hydrogen targets are often compound targets (CH_2, CH_4...). Beam-induced reactions on other components of the target (carbon), such as fusion–evaporation reactions, must be subtracted from the measured spectrum. This is achieved by

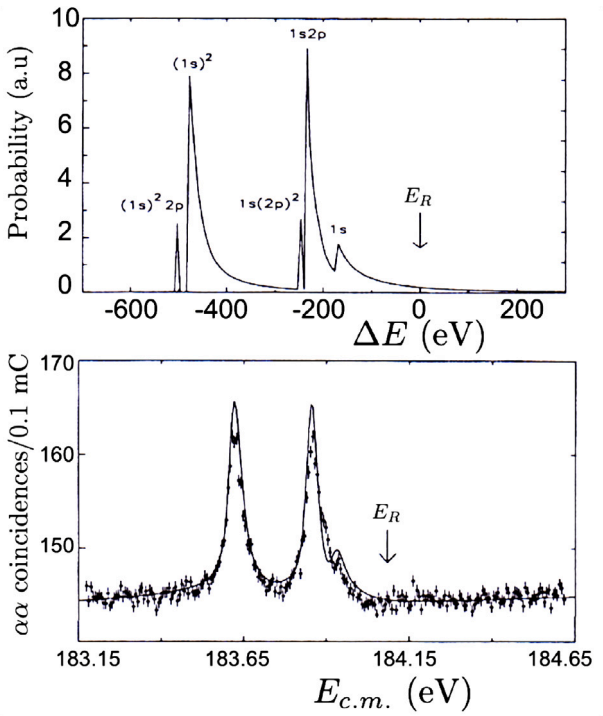

Fig. 16. (Top) Predicted ^{4}He(^{4}He, ^{4}He) ^{4}He population probabilities. (Bottom) Measured excitation function for the same reaction. Several peaks are observed at the resonance energy of the ^{8}Be compound nucleus ground state. These peaks correspond to the different masses of the ^{8}Be compound atom produced with different electronic excitation configurations.
Source: From Ref. [96].

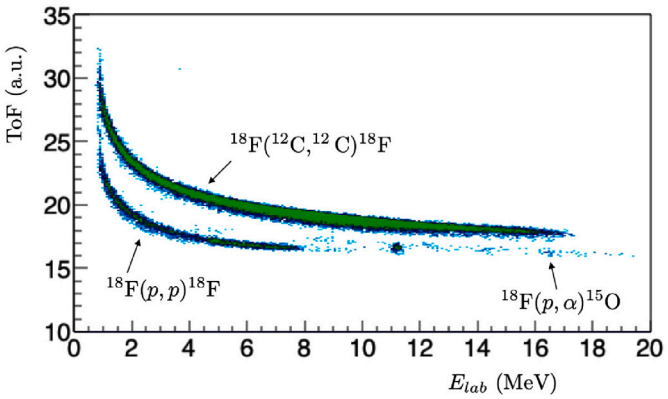

Fig. 17. Identification plot obtained in Ref. [44,97]. Time difference (ToF) measured between the MCP detector and the silicon detector (see Fig. 14) is shown against the energy of the particles measured in the silicon detector. Three extended spots can be observed: a spot corresponding to ^{18}F$(p,p)^{18}$F reactions, a spot corresponding to ^{18}F$(p,\alpha)^{15}$O reactions, and a spot from ^{18}F(^{12}C, ^{12}C)^{18}F reactions.

measuring the induced reactions on a pure carbon target under the same experimental conditions. This has the disadvantage of consuming beam time.

Another practical solution was proposed in Ref. [99], which does not require a background measurement. Among the events measured during the *RES* experiment, it is sufficient to select the events where 2 protons are detected in coincidence, which are mainly produced by fusion–evaporation reactions, and to reconstruct a spectrum of 1-proton events from these 2-proton events. Tests showed that this reconstructed spectrum is identical to the spectrum measured with a background target. This may not be true in all cases.

It has been shown in many studies (see for example Ref. [100]) that the background spectrum is a continuous spectrum, without peaks. Instead of subtracting the background spectrum from the measured spectrum, and inducing inevitable statistical fluctuations, it is possible to adjust a smooth function on the background spectrum and to subtract this function from the measured *RES* spectrum,

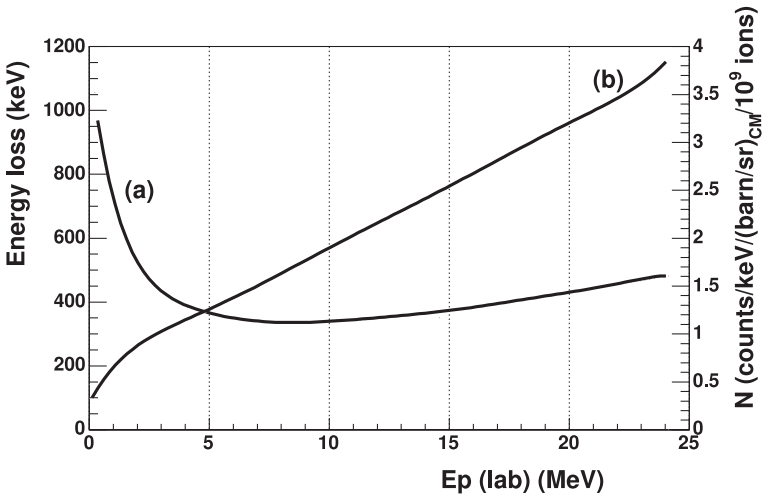

Fig. 18. Example of corrections applied in a thick target inverse kinematics experiment. (a) the energy lost inside the target by the scattered protons is plotted as a function of the measured proton energy in the laboratory frame (on the left axis). (b) the effective target thickness is shown as a number of counts measured in *lab* in keV^{-1} barns^{-1} steradian^{-1} per 10^9 incident ions (on the right axis). These functions were obtained from simulations. Here, the target is thick enough to stop the beam.
Source: From Ref. [98].

thus eliminating the statistical fluctuations.

Other aspects. Whenever possible, it is fruitful to combine different measurements. For example, Bardayan *et al.* [38] obtained the results shown in Fig. 13 (top right) for the ^{1}H(^{18}F, p)^{18}F reaction. Fitting this reaction allowed them to constrain the spin of the observed resonance to $J^\pi = 1/2^+$ or $3/2^+$. However, with the constrain of the ^{1}H(^{18}F, α)^{15}O excitation function measured simultaneously in the same experiment, see Fig. 13 (bottom right), the second value, i.e. $J^\pi = 3/2^+$, was assigned.

It can be difficult to fit the measured excitation function with multiple resonances using *R*-matrix code, especially if there is only a single reaction channel studies. Without sufficient constraints, non-physical results can be obtained [101]. It is often best to start with a simple set of realistic assumptions. A fictitious broad resonance at higher energy is often added to account for any contributions that are not taken into account in the fit.

It is recommended to measure, in the same experiment, another reaction whose states are accurately known, to obtain a correct energy calibration. The uncertainties associated with the measured parameters are often very difficult to estimate, especially when there are several resonances. The minimum value of χ^2 is preferably close to the number of degrees of freedom N_f, but this is rarely the case. This is often due to an imperfect energy calibration, normalization error or unsubtracted background. If χ^2 is significantly larger than N_f, it means that the error bars have been underestimated, or that something is missing in the fit, or there is a systematic error. In such a case, according to [102], the errors bars of the data should be multiplied by $\sqrt{\chi^2/N_f}$.

The uncertainties of the fitted parameters can be obtained by studying the evolution of χ^2. Indeed, the optimum value of the parameters is obtained by minimizing χ^2. The associated uncertainties correspond to $\chi_0^2 + \Delta\chi^2$, where χ_0^2 is the minimum value and $\Delta\chi^2$ the variance. For example, for an uncertainty of one sigma (one standard deviation, 68% of the data points) and for a single parameter to be adjusted, one find that $\Delta\chi^2 = 1$ for 1 degree of freedom, $\Delta\chi^2 = 2.3$ for 2 degrees of freedom, etc. The function *TMath::Prob* in the ROOT object-oriented data analysis code [103] can be used to calculate the $\Delta\chi^2$ variance. For example, for 105 degrees of freedom, *TMath::Prob*(111.35,105) = 100%–68% = 0.32, it follows that $\Delta\chi^2 = 111.35$. In reality, there is rarely just one parameter to fit. Estimating uncertainties with several parameters is challenging since correlations between the fitted parameters must be explored. Then, uncertainties are multi-dimensional ellipses in the parameters space around the χ^2 minimum. Some *R*-Matrix codes, such as AZURE [68,69], have this option for calculating uncertainties. With AZURE, $\Delta\chi^2$ variance must be set first, and a file with the uncertainties is generated after running the 'MINOS error analysis' option.

Strong correlations between parameters are sometimes observed. These correlations can be studied with the covariance matrix for all parameters allowed to vary in the fit [44,104]. If the off-diagonal elements are large, the individual uncertainties on parameters should be quoted along with the covariance matrix.

The *R*-matrix formalism deals with the coupling of discrete states to the continuum, i.e. the emission of particles from the nucleus. A rigorous derivation of the formula shows that this coupling induces an energy shift between the energy at which the resonance is observed and the energy of the state. This shift is called the *Thomas-Lane correction term* or simply *level shift*. *R*-matrix codes generally take this effect into account, it is not necessary to correct it by hand, the *R*-matrix level parameters are transformed into 'physical' pole energies and Breit–Wigner partial widths.

Sometimes, several emission channels are open from the same state, carrying different orbital angular momentum, ℓ, and different channel spin, s. For example, Fig. 19 shows results of *R*-matrix calculations in the case of the ^{7}Be(p, p)^{7}Be reaction. It is reported

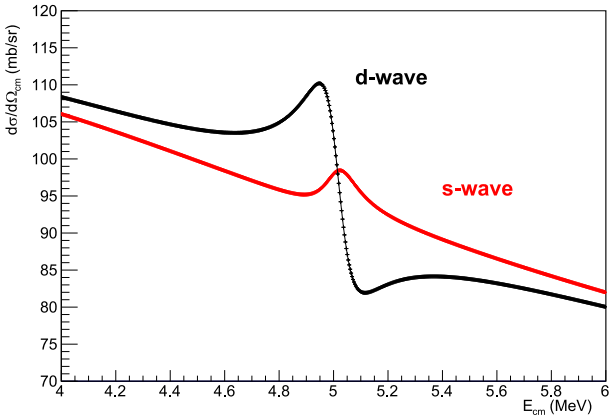

Fig. 19. Excitation function of the ^{7}Be(p, p)^{7}Be reaction calculated around the energy of the $J^{\pi} = 1^{-}$ resonance at $E_R \approx 4.9$ MeV. This resonance can be populated with two different angular momentum values, $\ell = 0$ or $\ell = 2$. Excitation functions are calculated using exactly the same parameters, with $\Gamma = 150$ keV for one channel and $\Gamma = 0$ keV for the other channel. The shapes of the resonances are very different.

in Ref. [105] the observation of a new resonance in ^{8}B at $E_R \approx 4.9$ MeV with $J^{\pi} = 1^{-}$. The ground state of ^{7}Be has $J^{\pi} = 3/2^{-}$. So, three emission channels are possible: $(s, \ell) = (1,0)$, $(1,2)$ and $(2,2)$. Since the experiment was not performed with a polarized beam, the two components with $\ell = 2$ are equally populated. The two cases $\ell = 0$ and $\ell = 2$ are compared in Fig. 19, using exactly the same parameters and just interchanging the partial widths, $\Gamma = 150$ keV for one channel and $\Gamma = 0$ keV for the other channel. The shapes of the resonances are very different. In principle, one would have to fit a partial width for each decay channel. In the case of the ^{18}F(p, α)^{15}O reaction, ^{19}Ne$(3/2^{+}) \rightarrow {}^{18}F(1^{+}) + p(1/2^{+})$ for example, there are 3 emission channels: $(s, \ell) = (3/2,0)$, $(1/2,2)$ and $(3/2,2)$. One might think that the highest angular momentum decay channels, e.g. $\ell = 2$, is negligible, due to the lower penetrability through the Coulomb and centrifugal barrier, but this is not always true since spectroscopic factors must also be taken into account.

5.9. Limitations

The *RES* technique has some specific application fields. It requires beam intensity larger than $\sim 10^{4}$ pps to measure a resonance peak of 5 keV width and $\approx$0.1 b/sr cross section in one day, and incident energy less than $\sim$5 MeV/u since many reaction channels generally open up at higher energies. Only states located above the particle emission threshold can be studied.

Radioactive beams are often contaminated. There is therefore a need for some means of subtracting the background caused by the contaminant. One solution is to measure the *RES* of the contaminant, if it can be produced as a pure beam, and subtract that component from the measured spectrum. Another solution is to measure the precise time of each measured event and correlate it with the arrival time of the particles in the beam.

In the *TTIK* technique, as a first approximation, the energy lost by the light particles scattered in the target can be neglected (or taken as a constant value, see Fig. 18). Since resonances always occur at the same *c.m.* energy, resulting in scattered particles of the same energy regardless of their position in the target, it is possible to use a beam whose energy is relatively degraded. This is true as long as the energies in the center of mass are equally present in the target, giving up the high and low energy sides of the measured excitation function.

When a very thick target is used, it is generally not possible to distinguish between elastic and inelastic scattering. This distinction can be made when a very large gas target (several tens of centimeters) is used and the time-of-flight of the scattered particles is measured [106]. Another solution is to use a medium thickness target, which can sometimes separate the two components on the basis of the measured energy [107].

The number of counts in a resonance peak depends on the partial and total widths of the resonance. The narrower the resonance, the fewer the number of counts in the measured peak, the longer the beam time required. In a certain energy range above the threshold, the resonance widths are generally very narrow, too narrow to be observed by this technique. In practice, with charged particles, only resonances with a width larger than $\approx$100 eV can be studied with the *TTIK* technique. It is not possible to observe the shape of the resonance when the resonance is narrower than the experimental energy resolution. For charged particles, the effective target thickness is a function of the energy. This is not the case with neutron beams.

Another limitation of the method is that the energy lost in the target by the scattered particles is a little uncertain, leading to some uncertainty in the measured energy of the resonances.

6. Particle–particle correlation

6.1. Principle

The *particle–particle angular-correlation (PPAC) technique* is a classical technique [17,108]. When two particles are emitted sequentially, energy and angular correlations between the two particles can be used to determine excitation energies, to constrain

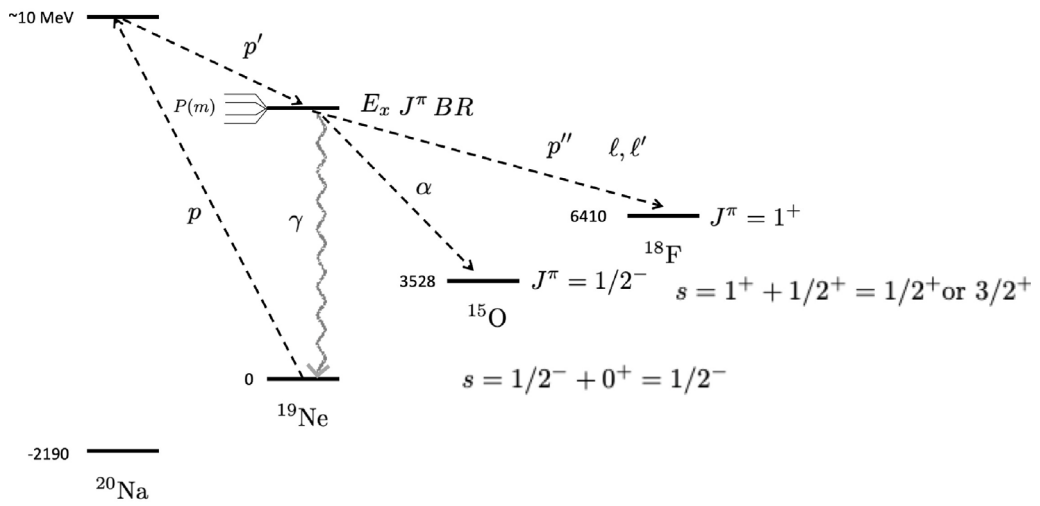

Fig. 20. Schematic representation of the ^{19}Ne$(p, p')^{19}$Ne* reaction, followed by the ^{19}Ne$^*(p'')^{18}$F or ^{19}Ne$^*(\alpha)^{15}$O particle emissions. The parameter $P(m)$ represents the population of the various magnetic substates. The different values s of the outgoing channel spin are given.

spins and parities in a model-independent way, to determine branching ratios BR, partial widths, and, possibly, the degree of polarization of the states. The technique has been used with different types of nuclear reactions, e.g. inelastic scattering, transfer [109–114].

6.2. Theory

The astrophysical reaction ^{18}F$(p, \alpha)^{15}$O has been studied using the inelastic scattering reaction ^{19}Ne$(p, p')^{19}$Ne* [112] and the charge exchange reaction ^{19}F$(^3$He, $t)^{19}$Ne* [113,115], followed by the emission of one proton in ^{19}Ne$^*(p'')^{18}$F or one α-particle in ^{19}Ne$^*(\alpha)^{15}$O. A schematic representation of the inelastic scattering reaction is shown in Fig. 20. A general and convenient formalism for predicting or interpreting the particle–particle correlations is presented in Ref. [17,116–118]. It is analogous to the collinear γ-ray angular correlation method [119]. When two particles are emitted sequentially in a nuclear reaction, for example the p' proton and α particle in the ^{19}Ne$(p, p')^{19}$Ne$^*(\alpha)^{15}$O reaction, the angular-correlation function $W(\theta^{c.m.})$ is defined as the probability of the α particle to be emitted in the $\theta^{c.m.}$ angle relatively to the beam axis, in the center of mass of the ^{19}Ne* nucleus, which obviously depends on the p' angle of emission.

The double-differential cross section, for detecting p' in the solid angles $d\Omega_{p'}$ and α in coincidence in $d\Omega_\alpha$, is

$$\left(\frac{d^2\sigma}{d\Omega_{p'}d\Omega_\alpha}\right)^{c.m.} = \left(\frac{d\sigma}{d\Omega_{p'}}\right)^{c.m.} \times \frac{\Gamma_\alpha}{\Gamma_T} \times \frac{W(\theta^{c.m.})}{4\pi} \tag{35}$$

where Γ_α and Γ_T are the α and total width of the emitting state. The α branching ratio is obtained after integration over 4π

$$BR_\alpha = \frac{\int_{4\pi} \frac{d^2\sigma}{d\Omega_{p'}d\Omega_\alpha} d\Omega_\alpha}{\frac{d\sigma}{d\Omega_{p'}}} = \frac{\Gamma_\alpha}{\Gamma_T} \int_0^\pi \frac{W(\theta^{c.m.})}{4\pi} 2\pi sin(\theta^{c.m.}) d\theta^{c.m.} = \frac{\Gamma_\alpha}{\Gamma_T} \tag{36}$$

It can be shown that the angular-correlation function can be expressed as

$$W(\theta^{c.m.}) = \sum_{m,\ell,\ell',s,K,r} P(m) A(J, \ell, \ell', s, m, K)(2 - \delta_{\ell,\ell'}) X^r(\ell, \ell') Y(s) P_K(cos(\theta^{c.m.})) \tag{37}$$

where

- $J, \ell, \ell', s, m, J^\pi$ are different quantum numbers defined in Fig. 20.
- $P(m)$ represents the population of the magnetic substates of the emitting state. By definition, the quantum number m can take $(2J + 1)$ values between $-J$ and $+J$. The $P(m)$ value depends on the reaction mechanism and on the angle between the first emitted particle and the beam angle.
- $A(J, \ell, \ell', s, m, K)$ is a coefficient that can be calculated. It is a product of Clebsch–Gordan and Racah coefficients [17].
- $\delta_{\ell,\ell'}$ is the Dirac function, equal to 1 when $\ell = \ell'$, otherwise 0.
- $X^r(\ell, \ell') = \frac{\langle \ell' \rangle}{\langle \ell \rangle}$ represents the mixing between the two possible orbital angular momentum ℓ and ℓ' carried by the decay particle. By definition, $-\infty < X < +\infty$. For parity conservation reasons, ℓ' is limited to $\ell' = \ell$ or $\ell' = \ell + 2$. The exponent r takes the values 0, 1 and 2 [116].
- $Y(s)$ represents the relative contribution to the angular correlation from each channel spin.

- $P_K(cos(\theta^{c.m.}))$ corresponds to the Legendre polynomial of order K, i.e. $P_0 = 1$, $P_2 = 0.5(3x^2 - 1)$, $P_4 = 0.125(35x^4 - 30x^2 + 3)$....
- K is an integer whose maximum value is given by the relation $K_{max} = min(\ell + \ell', 2J)$. For reasons of symmetry, only even values of K are to be considered. In the case where only one angular momentum is possible, $K_{max} = min(2\ell, 2J)$.

In summary, the angular distribution must be of the form

$$\left(\frac{d\sigma}{d\Omega_\alpha}\right)_{c.m.} = \sum_{K=0,even}^{K_{max}} a_K P_K(cos(\theta^{c.m.})) \tag{38}$$

where a_K are coefficients, P_K are Legendre polynomials and K_{max} is related to the spin and parity of the state. This formula can be used to predict or to fit the measured angular-correlation functions, thus constraining the spin and parity of the emitting states.

6.3. Projectile and incident energy

The reaction must populate excited states with maximally aligned spins in order to get very pronounced angular distributions. This is likely to occur efficiently via the formation of a compound nucleus, whose spin is necessarily in the plane perpendicular to the beam axis, and therefore fully aligned. The astrophysical ^{18}F(p, α)^{15}O reaction was studied in four different *PPAC* experiments. In all cases, it is likely that the formation of the compound nucleus was the main reaction mechanism.

The ^{19}F(^{3}He, t)^{19}Ne$^*(\alpha)^{15}$O charge exchange reaction was studied twice. A 8.3 MeV/u (10 MeV/u) ^{3}He beam was used in Ref. [113,115]. These experiments were performed in direct kinematics.

The ^{19}Ne$(p, p')^{19}$Ne$^*(\alpha)^{15}$O inelastic scattering was also studied twice [112,120]. These experiments were performed in inverse kinematics. The radioactive ^{19}Ne beam was produced with a mean intensity of 8×10^7 pps (2×10^7 pps) and accelerated to 9 MeV/u (10 MeV/u). At that incident energy, the main reaction mechanism is the formation of the compound nucleus, i.e. ^{19}Ne+$p \rightarrow {}^{20}$Na$^* \rightarrow p'+{}^{19}$Ne*. An interesting advantage of the fusion–evaporation mechanism is that the ^{19}Ne* excited states are populated approximatively in proportion to the $(2J+1)$ statistical factor (with J the spin of the ^{19}Ne populated state after proton evaporation). The inelastic-scattering cross section to populate the excited state is generally large ($\sigma > 1$ mb) if the incident energy $E_{inc}^{c.m.}$ is greater than $E_{inc}^{c.m.} \gtrsim E_x + 2$ MeV. In these experiments, a stable ^{19}F beam was used to calibrate the detectors and to measure the targets thickness, through the study of the inelastic scattering reaction ^{1}H(^{19}F,p')^{19}F$^*(\alpha)^{15}$N, since excited states in ^{19}F above both α and proton thresholds are known.

6.4. Target

In the direct kinematics experiments, e.g. ^{19}F(^{3}He, t)^{19}Ne$^*(\alpha)^{15}$O, the target should be thin enough to allow the emitted particles, usually of very low-energy, to leave the target and to be detected. The thickness of the target obviously has an impact on energy resolution. In the charge-exchange experiments [113,115], 80–200 μg/cm^2 CaF_2 targets were used.

In inverse kinematics, e.g. H(^{19}Ne, p')^{19}Ne$^*(\alpha)^{15}$O, it is possible to use thick targets because the emitted particles are boosted at forward angles. A good idea is to use a relatively thin hydrogen target combined with a thick (hydrogen-free) target to stop the beam [112]. The light particles emitted in the reactions usually have enough energy to pass through the thick target without too much energy loss. It is thus possible to measure all particles emitted in the forward direction, zero degree included. The price to pay is a loss of energy resolution. A thin target can also be combined with a magnetic spectrometer to select the light ejectiles and to reject the beam particles [120].

6.5. Experimental setup

It is important to note that, if the spin of the emitting nucleus is not aligned, i.e. if the magnetic substates m are equally populated, the angular correlation function is constant, i.e. $W(\theta) = 4\pi$, and then, it is not possible to determine the spin of the state from the angular distribution. Due to the axial symmetry of the experiment, the alignment refers to the spin alignment parallel to the beam axis. In the case of a capture reaction, when the axial symmetry of the reaction is preserved by detecting the first emitted particle at zero degree (in the beam axis), the smallest magnetic substates m are the most populated [115,119]. For example, the magnetic substates population $P(m)$ was measured in the case of the ^{19}Ne$(p, p')^{19}$Ne* reaction with the proton p' detected at zero degree, see Fig. 21. The population probability is significant only for the values $m = \pm 1/2$ with $P(|m| = 1/2) \approx 90\%$. Such a large value has the effect of increasing the amplitude of the angular distributions, which makes the analysis much simpler and the obtained results less ambiguous.

The setup of the inelastic-scattering experiment [112] is shown in Fig. 22. Excited states in ^{19}Ne were populated by the ^{1}H(^{19}Ne,p')^{19}Ne* inelastic-scattering reactions occurring in a plastic $(CH_2)_n$ target. Scattered protons, p', were detected at zero degree with a $\Delta E - E$ telescope of silicon detectors located 50 cm downstream of the target covering a solid angle of 5 msr. Scattered protons were detected at 0° for three reasons: (i) the best energy resolution for the excited states in ^{19}Ne* is obtained for this angle as the reaction is made in inverse kinematics, (ii) due to the axial symmetry of this experiment, the analysis of the proton–particle angular correlation is simplified, (iii) a strong alignment of the populated states in^{19}Ne* [119] is expected. A 250 μm-thick aluminium foil, placed between the target and the telescope, was used as a beam catcher. The intense radioactive beam was stopped inside this catcher while the scattered protons lost less than 20% of their energy after passing through it. The states located above the particle emission thresholds ($S_p = 6.411$ MeV and $S_\alpha = 3.529$ MeV) emit particles which were measured with a

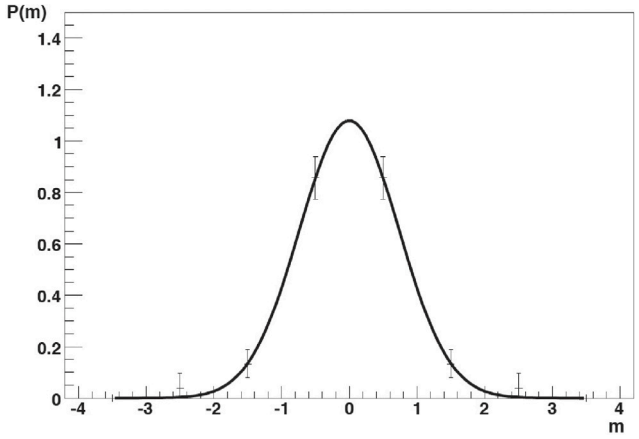

Fig. 21. Measured distribution of the magnetic substates population $P(m)$ as a function of the magnetic substates m of the ^{19}Ne* states populated in the reaction ^{19}Ne$(p, p')^{19}$Ne* at $E = 9$ MeV/u and with the p' proton detected at zero degree.
Source: From Ref. [121].

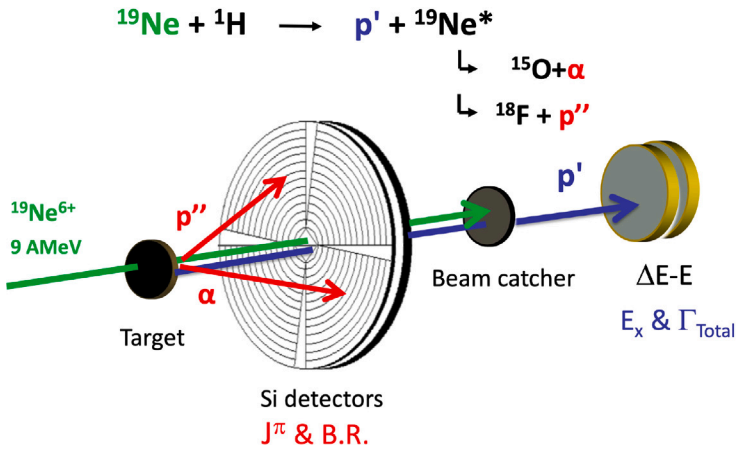

Fig. 22. Drawing of the experimental setup used in Ref. [121] to measure the ^{1}H(^{19}Ne, p')^{19}Ne*$(\alpha)^{15}$O and Ne*$(p'')^{18}$F reactions.

telescope of annular stripped silicon detectors (CD-PAD). This telescope was positioned between the target and the beam catcher, 10 cm downstream of the target. It covered laboratory angles between 4.3° and 21.6°. It is important to note that, in this case, the forward kinematic boost allows to measure a large part of the angular distribution with a single detector.

In the charge-exchange experiment of Ref. [113], the ^{19}Ne excited states were populated through the ^{19}F(^{3}He, t)^{19}Ne* reaction. The triton ejectiles were measured at the angle of 12° in lab using a magnetic spectrometer (Enge Split-pole type [122]). The angular acceptance was 1.7–3.3 msr. The excitation energy spectrum was measured with an energy resolution of 85 keV FWHM. Proton and α particles were measured in coincidence with six DSSSD detectors placed around the target at backward angles, allowing to measure the angular distributions between 90 and 172° in the center of mass. The identification of the particles was easily done from the determination of the Q energy of the reaction, which differs greatly between a proton emission and an α-particle emission.

6.6. Data analysis

Excitation energy. The excitation energy spectrum is derived from the measured energy of the ejectiles, i.e. from protons in ^{1}H(^{19}Ne, p')^{19}Ne* and from triton in ^{19}F(^{3}He, t)^{19}Ne*, since these are two-body kinematics reactions. If a coincidence is imposed with another particle, some states appear more clearly, others disappear, and any background is greatly reduced. Fig. 23 shows the example of the ^{1}H(^{19}Ne, p')^{19}Ne* inelastic scattering reaction measured in coincidence with the protons from ^{19}Ne* $\rightarrow^{18}$F+p''. The requirement of another proton detected in coincidence was used to see only the states located above the proton emission threshold and to suppress the background induced by reactions of the beam in the beam catcher (see Fig. 22). This spectrum was analyzed with a multiple peak-fitting program. Six peaks (labeled A to E) are required to fit the proton spectrum. Gaussian shapes were used for all peaks, except for the broad resonance at $E_{c.m.} \approx 1.4$ MeV (labeled E in Fig. 23) for which an energy-dependent Breit–Wigner shape [123] was used instead.

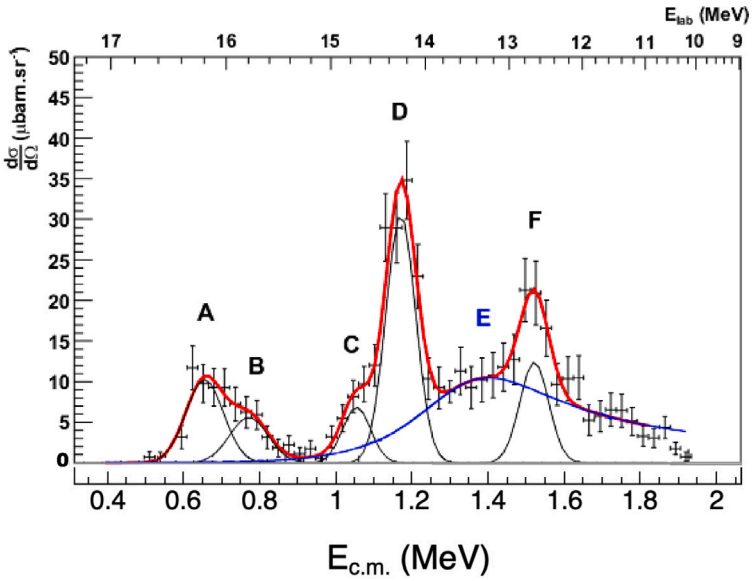

Fig. 23. The measured differential cross section for the ^{1}H(^{19}Ne, p')^{19}Ne* reaction, with the proton p' detected at zero degree, is presented as a function of the center-of-mass energy in the system ^{19}Ne* $\rightarrow$^{18}F+p'' (lower axis) and the proton measured energy in the laboratory (upper axis) corrected for energy losses in the beam catcher. The energy resolution in excitation energy of ^{19}Ne is 30 keV FWHM. This figure was conditioned with the detection of another proton coming from the emission channel ^{19}Ne*(p'')^{18}F. Gaussian-shaped peaks were used to fit the five observed narrow peaks. The E broad peak (in blue) was fitted with a Breit–Wigner shape using an energy-dependent proton width. The existence of this broad resonance had been predicted before it was observed [124,125].
Source: From Ref. [112].

Branching ratios and widths. It is possible to measure the width of resonances directly, by measuring the width of peaks, when the experimental energy resolution is lower than the resonance width. When multiple decay channels are possible, for example proton and alpha emitted from the same state in ^{19}Ne*, the branching ratio can be measured accurately by counting the number of protons and the number of α-particles detected, then correcting these numbers for particle detection efficiency taking into account the angular distributions of emitted particles.

Spin assignment. The general principle of the *PPAC* analysis is as follows. The first particle is measured at an angle, and the angular distribution of the second particle is measured relative to the beam axis in the center of mass of the emitter nucleus. For example, the angular distributions of the protons p'' from Ne*(p'')^{18}F are shown in Fig. 24 for the six observed resonances. These distributions are very different from each other, which shows that these states have different spins and that they were produced with strongly aligned spins. Then, the angular distributions are fitted with a Legendre polynomial in $cos(\theta_{c.m.})$. In the case of an excited state in ^{19}Ne with, for example, $J^{\pi} = \frac{3}{2}^{+}$ spin, two values of ℓ are possible, $\ell = 0$ and $\ell' = 2$. It follows that $K_{max} = min(\ell + \ell', 2J) = min(2, 3) = 2$, and according to Eq. (37), the angular distribution should be in the form

$$\left(\frac{d\sigma}{d\Omega_{\alpha}}\right)_{J^{\pi}=\frac{3}{2}^{+}} = a + b \times cos^{2}(\theta_{c.m.}) \tag{39}$$

with a and b two free parameters. This is a parabolic form in $cos(\theta)$, which is well observed in Fig. 24 for states A, B and D. It is therefore possible to assign a spin $J^{\pi} = \frac{3}{2}^{+}$ to these states. It would have been isotropic for the spin $J = \frac{1}{2}$, parabolic for $J = \frac{3}{2}$, biquadratic for $J = \frac{5}{2}$ and so on.

Usually, the fit coefficients are not completely free, they are linked to each other, which further constrains the fit. In the current example, it is possible to show that

$$\left(\frac{d\sigma}{d\Omega_{\alpha}}\right)_{J^{\pi}=\frac{3}{2}^{+}} = N(a_0 + 3(1 - a_0)cos^{2}(\theta_{c.m.})) \tag{40}$$

with N and a_0 two constants. It is possible to show that a_0 can be expressed as a function of the constants $P(m = 1/2)$, $Y(s = 1/2)$ and $X(0, 2)$.

6.7. Limitations

Several precautions must be taken when analyzing the data.

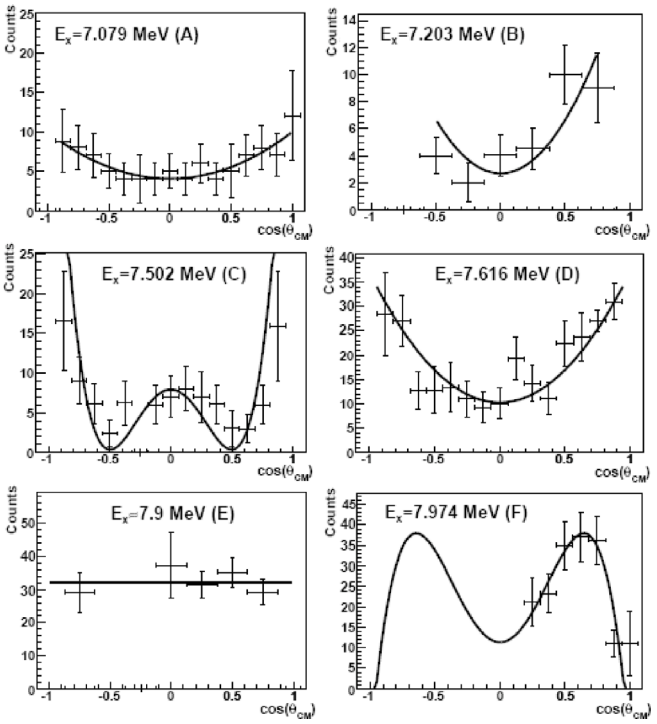

Fig. 24. Center-of-mass angular distributions of the protons emitted from $^{19}Ne^{*} \rightarrow ^{18}F+p''$, measured for the 6 excited states populated in the $^{1}H(^{19}Ne, p')^{19}Ne^{*}$ reaction (see Fig. Fig. 23) [112]. Lines correspond to the best fits obtained in the analysis. These results show that the angular distribution can be used to constrain the spin of the states. Note that part of the angular distribution of levels E and F was beyond the angular coverage of the detectors.

- It is necessary to determine the excitation energy of the recoil nucleus. Indeed, different excited states of $^{18}F^{*}$ can be populated in the case of the $^{1}H(^{19}Ne, p')^{19}Ne^{*}(p'')^{18}F^{*}$ reaction. To determine the excitation energy, the $^{19}Ne^{*}$ excited state is first selected, e.g. by selecting protons p' of a certain energy measured at a certain angle from the $^{1}H(^{19}Ne, p')^{19}Ne^{*}$ reaction. The excitation energy of $^{18}F^{*}$ can be determined from the measurement of the energy and angle of the second proton, p'', and if possible, of the $^{18}F^{*}$ daughter nucleus measured in coincidence.
- It is also necessary to measure possible background, particle–particle coincidences coming for example from fusion–evaporation reactions with carbon atoms present in the target.
- There is another problem that can be a serious limitation of the method in some cases. Indeed, it is possible that particle number 2 is emitted before particle number 1. For example, the $^{1}H(^{19}Ne, \alpha)^{16}F^{*}(p)^{15}O$ reaction can be confused with the $^{1}H(^{19}Ne, p)^{19}Ne^{*}(\alpha)^{15}O$ reaction, where, in both cases one proton and one alpha are emitted in coincidence. This leads to the results shown in Fig. 25, where the measured energy of the alpha particles is shown against the measured energy of the protons. Vertical bands can be observed, corresponding to ^{19}Ne states populated by inelastic scattering, and leaning bands are also observed, corresponding to ^{16}F states populated by the other reaction. The two series of bands overlap, they cannot be disentangled easily.
- There is also an obvious limit of this kind of experiments: only states above the particle emission threshold can be measured (see the alpha emission threshold S_{α} in Fig. 25).
- Moreover, the branching ratio for particle emission must be large enough, which means there is a white area just above the threshold (see Fig. 25) where no state is visible since they decay mostly by γ-ray emission.
- It should be noted that, when the density of states is high, it is difficult, if not impossible, to obtain angular distributions for individual states.
- If the emitting state is a long-lived state, the spin alignment can be modified by the interactions of the nucleus with an extra-nuclear field (environmental effect) [126].

7. Nuclear transfer reaction

7.1. Principle

A nuclear transfer reaction is a reaction in which one or several nucleons are transferred from one nucleus to another one. It is said to be a *stripping* reaction when the projectile loses particle(s), e.g. $^{18}F(d, n)^{19}Ne^{*}$ [31,111,127], and a *pick-up* reaction when the

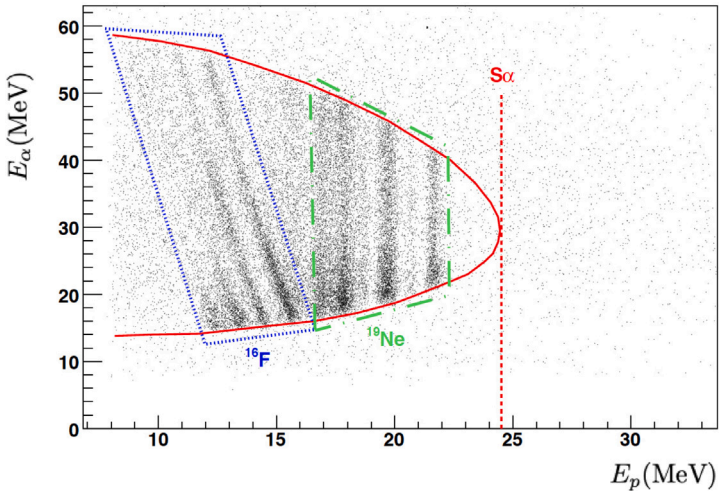

Fig. 25. The measured energy of the alpha particle is shown as a function of the measured energy of the proton. Vertical bands correspond to states populated in the ^{1}H(^{19}Ne, p')^{19}Ne*(α)^{15}O inelastic scattering reaction. Leaning bands are ^{16}F states from the ^{1}H(^{19}Ne, α)^{16}F*(p)^{15}O reaction populated in the same experiment. The red line corresponds to the kinematics limits. The red dashed line shows the alpha emission threshold in ^{19}Ne.
Source: Experimental results from Ref. [121].

projectile gains particle(s), e.g. ^{20}Ne$(p,d)^{19}$Ne* [70] or ^{20}Ne(^{3}He, ^{4}He)^{19}Ne*[128] . When transfer takes place in both directions, for example in the ^{19}F$(p,n)^{19}$Ne* reaction, or in the ^{19}F(^{3}He, t)^{19}Ne* reaction [27], where a neutron is exchanged for a proton, this type of reaction is called a *charge exchange reaction*. In the general case, it is called a multi-nucleon transfer reaction, e.g. ^{6}Li(^{16}O, ^{19}Ne*)^{3}H [129]. Transfer reactions are widely used in astrophysics [130], and the ^{18}F$(p,\alpha)^{15}$O reaction has been studied several times in this way. The transfer reaction ^{2}H(^{18}F, $p\alpha$)^{15}N [131] was used to study the ^{18}F$(n,\alpha)^{15}$N reaction, mirror of the ^{18}F$(p,\alpha)^{15}$O reaction (this was the second physical case studied with a radioactive beam, see Ref. [132] for the first experiment).

The astrophysical reaction ^{18}F$(p,\alpha)^{15}$O looks very similar, for example, to the nuclear transfer reaction ^{18}F$(d,n)^{19}$Ne*, which is followed by the spontaneous emission ^{19}Ne$^{*} \rightarrow {}^{15}$O $+ \alpha$. This similarity is not only apparent, the cross section of the latter reaction is proportional to the cross section of the former reaction. Thus, transfer reactions can be used to study astrophysical reactions [111]. The major advantage of transfer reactions is that these have much larger cross sections than astrophysical reactions. The disadvantage is that theoretical models are needed to analyze transfer reactions.

Transfer experiments can be analyzed with a large variety of theoretical models (DWBA, CC, CCBA, CDCC, CRS, ADWA, PWAI, THM, ANC, etc.) [133]. The Distorted-Wave Born Approximation (DWBA) is the most frequently used analysis to transfer reaction measurements. The Trojan Horse Method (THM) is a method that applies very well to nuclear astrophysics. To illustrate the interest of nuclear transfer reactions in astrophysics, DWBA and THM methods are presented hereafter in more details.

7.2. Theory

The ^{18}F$(d,n)^{19}$Ne* transfer reaction is much weaker than the ^{18}F$(d,d)^{18}$F elastic scattering, so it is possible to start the theoretical modelling by describing the elastic scattering and then to treat the transfer reaction as a small perturbation.

Elastic scattering

For incident energies well above the Coulomb barrier, it is not possible to use the R-matrix formalism to describe elastic scattering reaction, due to the high density of states, see Fig. 9 for the ^{18}F$(p,p)^{18}$F case. Another theoretical formalism has to be used. It is assumed that the ^{18}F$(d,d)^{18}$F elastic scattering reaction can be treated as a stationary state. The wave function of the deuteron $\chi_d(\vec{r})$ satisfies the time-independent Schrödinger equation

$$\frac{\hbar^2}{2\mu}\left[\Delta + k_d^2\right]\chi_d(\vec{r}) = V(r)\chi_d(\vec{r}) \tag{41}$$

where $V(r)$ is the potential describing the elastic scattering, k_d is the momentum of the deuteron, r is the distance evaluated relatively to the scattering center and μ is the reduced mass. Optical potentials, such as real and imaginary Woods–Saxon potentials, can be used for $V(r)$.

It is possible to show [134] that the Schrödinger equation can be rewritten with the *integral equation*

$$\chi_d(\vec{r}) = e^{+ik_d z} - \frac{\mu}{2\pi\hbar^2}\int \frac{e^{+ik_d|\vec{r}-\vec{w}|}}{|\vec{r}-\vec{w}|}\, V(w)\ \chi_d(\overrightarrow{k_d},\vec{w})d^3w \tag{42}$$

Here, the Schrödinger equation is not solved since the wave function $\chi_d(\vec{w})$ inside the integral is still unknown. The first term corresponds to the incident plane wave, it describes the deuteron before scattering, and thus the second term is the scattered wave

function $\chi_{sc}(\vec{r})$.

After elastic scattering, the deuteron is measured at angle θ with a momentum $\vec{k_d}'$. At a great distance from the target, $|\vec{r}-\vec{w}| \approx r - \frac{\vec{r}}{r}\vec{w}$, and it comes[1]

$$\chi_{sc}(\vec{r}) \underset{r\to+\infty}{\longrightarrow} -\frac{\mu}{2\pi\hbar^2}\frac{e^{+ik_d r}}{r}\int e^{-i\vec{k_d}'\vec{w}}\ V(w)\ \chi_d(\vec{k_d},\vec{w})d^3w \tag{43}$$

The flux of scattered deuterons measured in the solid angle $d\Omega = dS/r^2$ per time unit is equal to $\chi^2_{sc}(r)v'_d dS$ with v'_d the velocity of the scattered deuterons. The scattering cross section $d\sigma$ is the ratio between the scattered flux and the incident flux on the target, the latter being proportional to the incident velocity v_d. It follows

$$\left(\frac{d\sigma}{d\Omega}\right)_{^{18}\mathrm{F}(d,d)^{18}\mathrm{F}} = \frac{\mu^2}{4\pi^2\hbar^4}\frac{k'_d}{k_d}\ |T_{^{18}\mathrm{F}(d,d)^{18}\mathrm{F}}|^2 \tag{44}$$

with the nuclear matrix element

$$T_{^{18}\mathrm{F}(d,d)^{18}\mathrm{F}} = \int e^{-i\vec{k_d}'\vec{w}}\ V(w)\ \chi_d(\vec{k_d},\vec{w})d^3w \tag{45}$$

which is a function of θ only, due to the axial symmetry of the problem.

Distorted Wave Born Approximation

We suppose now that the interaction potential between the incident nucleus and the target nucleus can be written as $V(r) = V_1(r)+V_2(r)$, with V_1 describing the elastic scattering reaction, and V_2 is the interaction between the target nucleus and the transferred particle, which is a weak perturbation describing the transfer reaction. It is possible to show [136], in the case of the $^{18}\mathrm{F}(d,n)^{19}\mathrm{Ne}^*$ transfer reaction, that Eq. (45) can be rewritten

$$T_{^{18}\mathrm{F}(d,n)^{19}\mathrm{Ne}^*} = \int \chi_2^{(-)}(\vec{k_2},\vec{w_2})\ \Psi_n^*\ \Psi_{^{19}\mathrm{Ne}^*}^*\ V_2\ \Psi_d\Psi_{^{18}\mathrm{F}}\ \chi(\vec{k_1},\vec{w_1})\ d^3w_1 d^3w_2 \tag{46}$$

where the function $\chi(\vec{k_1},\vec{w_1})$ is the exact solution of the Schrödinger equation, and $\chi_2^{(-)}(\vec{k_2},\vec{w_2})$ describes the elastic scattering in the exit channel, i.e. $^{19}\mathrm{Ne}^*(n,n)^{19}\mathrm{Ne}^*$, and $\Psi_d,\ \Psi_{^{18}\mathrm{F}},\Psi_n^*,\ \Psi_{^{19}\mathrm{Ne}^*}^*$ are the internal wave functions and complex conjugate of the wave functions, V_2 describing the $^{18}\mathrm{F} + p = {}^{19}\mathrm{Ne}^*$ interaction.

If $V_2 \ll V_1$, the exact solution $\chi(\vec{k_1},\vec{w_1})$ inside the integral (obtained for $V(r)$) can be approximated by the incoming elastic scattering solution $\chi_1^{(+)}(\vec{k_1},\vec{w_1})$. This first-order approximation is known as the Distorted Wave Born Approximation (DWBA). The corresponding nuclear matrix element is

$$T^{DWBA}_{^{18}\mathrm{F}(d,n)^{19}\mathrm{Ne}^*} = \int \chi_2^{(-)}\ \Psi_n^*\ \Psi_{^{19}\mathrm{Ne}^*}^*\ V_2\ \Psi_d\Psi_{^{18}\mathrm{F}}\ \chi_1^{(+)}\ d^3w_1 d^3w_2 \tag{47}$$

It follows that the transfer cross section can be calculated with

$$\left(\frac{d\sigma}{d\Omega}\right)^{DWBA}_{^{18}\mathrm{F}(d,n)^{19}\mathrm{Ne}^*} = \frac{\mu\mu^*}{4\pi^2\hbar^4}\frac{k_n}{k_d}\ |T^{DWBA}_{^{18}\mathrm{F}(d,n)^{19}\mathrm{Ne}^*}|^2 \tag{48}$$

where μ and μ^* are the reduced masses for the entrance and exit channels.

Spectroscopic factors

In Eq. (48), it was assumed that projectile d and residual nucleus $^{19}\mathrm{Ne}^*$ present a pure single-particle configuration. In other words, it was assumed that $^{19}\mathrm{Ne}^*$ is perfectly described as a $^{18}\mathrm{F}_{g.s.}$ core plus one proton p orbiting around it in a given orbit, e.g. $^{18}\mathrm{F}_{g.s.} \otimes \pi_{2s1/2}$. The same for $d = p+n$. Generally, one particular single-particle configuration represents only a part of the total wave function, for example in the previous case the wave function could also be described as a proton orbiting around an excited core nucleus.

Spectroscopic factor is defined as the overlap between the initial and final configurations. It follows that the experimental cross section of a transfer reaction is proportional to these spectroscopic factors, for example

$$\left(\frac{d\sigma}{d\Omega}\right)^{Measured}_{^{18}\mathrm{F}(d,n)^{19}\mathrm{Ne}^*} = C^2S_p(d)\ \ C^2S_p(^{19}\mathrm{Ne}^*)\ \ \left(\frac{d\sigma}{d\Omega}\right)^{DWBA}_{^{18}\mathrm{F}(d,n)^{19}\mathrm{Ne}^*} \tag{49}$$

where $C^2S_p(d)$ is the proton spectroscopic factor of the incident deuteron, and $C^2S_p(^{19}\mathrm{Ne}^*)$ is the proton spectroscopic factor for the populated state in the residual nucleus.

Generally, the spectroscopic factor of the incident particle is already known, or calculated, e.g. $C^2S_p(d = n+p) = 1$ ($C^2S_p(d) = C^2S_n(d) = 1.55$ was also used in [111]), $C^2S_\alpha(^7\mathrm{Li}) = 1$ [137], $C^2S_p(^3\mathrm{He}) = 4.42$ [138,139].

Experimentally, the spectroscopic factors of the residual nucleus, $C^2S_p(^{19}\mathrm{Ne}^*)$, can be obtained for each state populated in transfer reaction, by renormalizing the calculated DWBA cross sections to the measured ones.

A number of considerations need to be taken into account:

[1] Max Born obtained this equation in 1926. It allowed him to interpret the wave function in terms of probability amplitude [135].

- It is assumed that the particle is transferred directly from the initial to the final state. In the case of the ^{18}F$(d,n)^{19}$Ne* stripping transfer reaction, the projectile d is composed of the particles $n+p$. It is assumed that the proton p is transferred directly from the projectile d to the target ^{18}F, forming the nucleus ^{19}Ne* =^{18}F + p, see Fig. 26.
- In Eq. (49), the isospin formalism has been explicitly used, where C^2 is the square of the isospin Clebsch–Gordan coupling coefficient. For example, for the α spectroscopic factor of ^{7}Li = $t+\alpha$, $C = \langle T(t)T(\alpha)T_z(t)T_z(\alpha)|T(^7\text{Li})T_z(^7\text{Li})\rangle = \langle 1/2\ 0\ 1/2\ 0\ |\ 1/2\ 1/2\rangle = 1$, and for the proton spectroscopic factor of ^{18}F =^{17}O + p, $C = \langle 1/2\ 1/2\ 1/2 - 1/2\ |0\ 0\rangle = 0.5$. In some publications, C^2S is written S.
- Different definitions on spectroscopic factor (also called relative reduced width or spectroscopic strength) can be found in the literature, which can lead to some confusion. Spectroscopic factor is not an observable, which means it is a model-dependent parameter. This may also explain why sometimes different values are published in the literature for the same state. It is therefore difficult to obtain accurate values of spectroscopic factors, but relative values between several measured states are often accurate.
- For stripping reactions, some studies explicitly use the spin statistical factor

$$\left(\frac{d\sigma}{d\Omega}\right)^{Measured} = C^2S_p\ C^2S_t\ \frac{2J_f+1}{2J_i+1}\left(\frac{d\sigma}{d\Omega}\right)^{DWBA} \tag{50}$$

  where C^2S_p and C^2S_t are the projectile and target spectroscopic factors, and J_f and J_i are the spins of the populated states and target. In fact, it depends on what is included in the calculated DWBA cross section (e.g. DWUCK [140] code uses this relationship).
- It is common to report the $(2J_f+1)C^2S_t$ value instead of C^2S_t, especially when the spin of the populated state is not known.
- It is possible that several single-particle configurations are involved in the same transfer reaction, in which case they must be taken into account in the fitting of the experimental cross section, for example

$$\left(\frac{d\sigma}{d\Omega}\right)^{Measured}_{^{18}\text{F}(d,n)^{19}\text{Ne}^*} = C^2S_p(d)\ \left(C^2S_{\pi 2s1/2}(^{19}\text{Ne}^*)\ \left(\frac{d\sigma}{d\Omega}\right)^{DWBA}_{\pi 2s1/2} + C^2S_{\pi 1d5/2}(^{19}\text{Ne}^*)\ \left(\frac{d\sigma}{d\Omega}\right)^{DWBA}_{\pi 1d5/2}\right) \tag{51}$$

  where $C^2S_{\pi 1d5/2}(^{19}\text{Ne}^*)$ and $C^2S_{\pi 2s1/2}(^{19}\text{Ne}^*)$ are the proton spectroscopic factors for populating the $1d5/2$ and the $2s1/2$ single-particle orbits. The contribution of each configuration, and so the spectroscopic factors, can be determined by fitting the measured angular distribution with both parameters.
- According to the principle of time-reversal symmetry, the spectroscopic factors C^2S_p(d) and $C^2S_p(^{19}\text{Ne}^*)$, obtained with the ^{18}F$(d,n)^{19}$Ne* reaction, are the same as those obtained with the time-reversal reaction ^{19}Ne$^*(n,d)^{18}$F, not to be confused with the ^{19}Ne$(n,d)^{18}$F* reaction, which gives different spectroscopic factors $C^2S_p(^{19}\text{Ne}_{gs})$. The latter reaction probes the ground state of ^{19}Ne on the basis of the ^{18}F* excited states.
- The spectroscopic factor is related to the components in the initial- and final-state wave functions [141,142], and therefore to the structure of the states. It can be broken down into different pieces

$$C^2S = c^2\ \times\ (cfp)^2\ \times\ n \tag{52}$$

  where n is the number of nucleons in the nuclear shell where particle transfer takes place, (cfp) is the coefficient of fractional parentage due to the anti-symmetrization between the nucleons and the core nucleus [143], and c is the probability amplitude of the wave function. Let us take simple examples to illustrate this.

  - In the case of the ^{16}O$(d,p)^{17}$O$^*(5/2^+)$ reaction, assuming the populated state is perfectly described as ^{16}O$_{g.s.}\otimes\nu(1d5/2)$, then $n=1$, $cfp\ ((1d5/2)^0 \rightarrow (1d5/2)^1) = 1$ and $c=1$, and so $C^2S(1d5/2)=1$.
  - In the case of the ^{20}O$(d,p)^{21}$O$^*(5/2^+)$ reaction, if ^{20}O is described as $(1d5/2)^4$ and the populated state as $a(1d5/2)^4(1d3/2) + b(d5/2)^2(2s1/2)^2(1d3/2)$, then $n=1$ (only one neutron in $1d3/2$), $cfp\ ((1d3/2)^0 \rightarrow (1d3/2)^1) = 1$ and $c=a$, so $C^2S(1d3/2)=a^2$.
  - In the case of the ^{18}O$(d,p)^{19}$O$^*(5/2^+)$ reaction, if ^{18}O is described as $(1d5/2)^2_{0^+}$ and the populated state as $(1d5/2)^3_{5/2^+}$, then $n=3$ (three neutrons in $1d5/2$), $cfp\ ((1d3/2)^2 \rightarrow (1d3/2)^3) = \sqrt{(2)}/3$ [143], and $c=1$, so $C^2S(1d5/2)=2/3$.
  - In the case of the ^{17}O$(t,d)^{18}$O$^*(0^+)$ reaction, assuming ^{18}O is described as $(1d5/2)^2_{0^+}$ and ^{17}O as $(1d5/2)^1_{5/2^+}$, then $n=2$ (two neutrons in $1d5/2$), $cfp\ ((1d5/2)^1 \rightarrow (1d5/2)^2) = 1$ and $c=1$, so $C^2S(1d5/2)=2$.
  - In the case of the ^{18}F$(d,n)^{19}$Ne$^*(1/2^+)$ reaction, assuming ^{18}F$_{g.s.}$ is described as $\pi(1d5/2)\otimes\nu(1d5/2)$ and $\Psi(^{19}\text{Ne}^*) = c_1[^{18}\text{F}_{g.s.}\otimes\pi_{2s1/2}] + c_2[^{18}\text{F}_{g.s.}\otimes\pi_{1d5/2}]$, then $C^2S(2s/2) = c_1^2\times 1\times 1 = c_1^2$ and $C^2S(1d5/2) = c_2^2\times 1\times 2 = 2c_2^2$

- As seen in the previous examples, spectroscopic factors can be greater than 1. When all the spectroscopic factors are added up, over all excited states of a nucleus, for populating or depopulating a single-particle shell, the total number of particles that this shell can contain is obtained, i.e. 2j + 1, this is called the *sum rule*.

Partial widths

How can we link the spectroscopic factors measured in the ^{18}F$(d,n)^{19}$Ne* transfer reaction with the ^{18}F$(p,\alpha)^{15}$O astrophysical reaction? The partial width of a resonance is one of the important parameters needed to calculate the BW cross section.

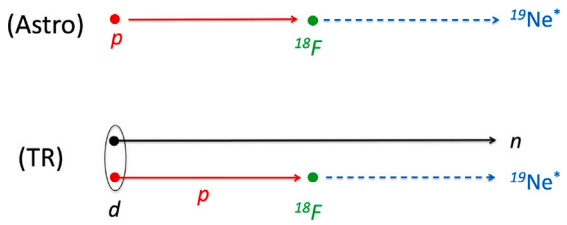

Fig. 26. The $^{18}\mathrm{F}(d,n)^{19}\mathrm{Ne}^*$ (TR) transfer reaction is measured in order to determine the rate of the $^{18}\mathrm{F} + p \rightarrow {}^{19}\mathrm{Ne}^*$ (Astro) astrophysical reaction. In the direct transfer model (one-step transfer), the projectile d is seen as composed of the particles p and n. The particle p is transferred directly from the nucleus d to the nucleus $^{18}\mathrm{F}$, forming the compound nucleus $^{19}\mathrm{Ne}^* = {}^{18}\mathrm{F}_{g.s.} + p$.

In the R-matrix formalism, see Section 5.2, it was shown that in the case of one neutron and a square potential well of radius a without centrifugal barrier ($\ell = 0$), the partial width is (Eq. (32))

$$\Gamma = 2\,\gamma^2\,ka \tag{53}$$

where γ^2 is the reduced width. This can be generalized to the emission of any kind of particle [16–18,66], or a cluster of particles, with the relationship

$$\Gamma(E) = 2\gamma^2 P_L(E) \tag{54}$$

where $P_L(E)$ is the penetrability of the Coulomb, nuclear and centrifugal barriers, which can be calculated [16]. In the case of the neutron, $P_{L=0,E\rightarrow 0}(\text{neutron}) = ka$ [17].

The reduced width, $\gamma^2 = \hbar^2/ma^2$, contains the information regarding the nuclear structure of the resonance. In Section 5.2, it was also shown that the wave function of the neutron at the surface of the potential well is $\mathrm{X}^2_\lambda(r=a) = \frac{2}{a}$ (Eq. (23)) and the radial wave function $\mathrm{X}^2_\lambda(r) = R^2(r)r^2$, it comes

$$\gamma^2 = \frac{\hbar^2}{2ma}a^2R^2(a) \tag{55}$$

The partial width $\Gamma(E)$ is proportional to the probability to find the particle at the surface ($r = a$) of the nucleus, i.e. $a^2R^2(a)$. It is possible to show that this relationship is valid for any kind of particle [17].

The radial wave function of the particle, $R(r)$, can be computed numerically, for example with the code WSPOT [144] or BIND [145], assuming a pure single-particle wave function and using a Woods–Saxon nuclear potential. Fig. 27 shows the example of the $E_x = 7.076$ MeV state in ^{19}Ne, described as $^{18}\mathrm{F}_{g.s.} \otimes \pi_{2s_{1/2}}$. Then, the single-particle width, Γ_{sp}, can be calculated at the resonance energy, E_r, using the radial wave function, $R_{sp}(a)$, calculated at the surface $r = a$ of the nucleus

$$\Gamma_{sp}(E_r) = \frac{\hbar^2 a}{\mu}R^2_{sp}(a)P_L(E_r) \tag{56}$$

where m, used in a potential well, has been changed to μ, the reduced mass, valid for a real physical system. However, the resonance is not necessarily described by a pure single-particle structure. The single-particle strength may be distributed over several states of the residual nucleus. It is therefore necessary to weight the calculated single-particle wave function with a normalization coefficient, that is the spectroscopic factor C^2S. It is often assumed that $R(r)^2 = C^2S\ R^2_{sp}(r)$. It follows that the experimental partial width can be calculated from the spectroscopic factor [145]

$$\Gamma_{\text{expt}}(E) = C^2S \times \Gamma_{sp} = \frac{\hbar^2}{ma}\ P_L(E) \times C^2S \times a^2R^2(a) \tag{57}$$

Transfer reactions can be used to determine spectroscopic factors, which can then be used to determine partial widths and cross sections of astrophysical reactions.

7.3. Projectile

Light particles ($p, d, t,{}^3$He, ^{4}He, ^{6}Li, ^{7}Li) are often used in transfer experiments because (i) it is easier to obtain beams or targets containing these particles, (ii) there is no need to take excited states into account, (iii) there is less chance of multi-step transfer.

Several factors are involved in the choice of the projectile.

– *Spectroscopic factor*. The particle of interest should be transferred to determine the corresponding spectroscopic factor. For example, a proton should be transferred, e.g. with the (d,n) reaction, in order to determine C^2S_p, the proton spectroscopic factor. In the case of the $^{18}\mathrm{F}(p,\alpha)^{15}\mathrm{O}$ reaction, two partial widths are needed for each resonance, the proton width, Γ_p, and the α width, Γ_α, the γ width being negligible in the Gamow window. It is not possible to measure the proton and α spectroscopic factors in the same transfer reaction experiment. This also means that, if the astrophysical reaction involves a radioactive nucleus, then a radioactive beam (or target) should be used. The proton spectroscopic factor of the $^{18}\mathrm{F}(p,\alpha)^{15}\mathrm{O}$ reaction can only be determined by measuring a proton transfer reaction to the ^{18}F nucleus, and the α spectroscopic factor by α transfer to ^{15}O. It is also possible to use the mirror symmetry property of the nuclear interaction to measure C^2S_n the neutron spectroscopic factors, via the $^{18}\mathrm{F}(d,p)^{19}\mathrm{F}^*$ reaction for example [146], to deduce $C^2S_p = C^2S_n$ the proton spectroscopic factors.

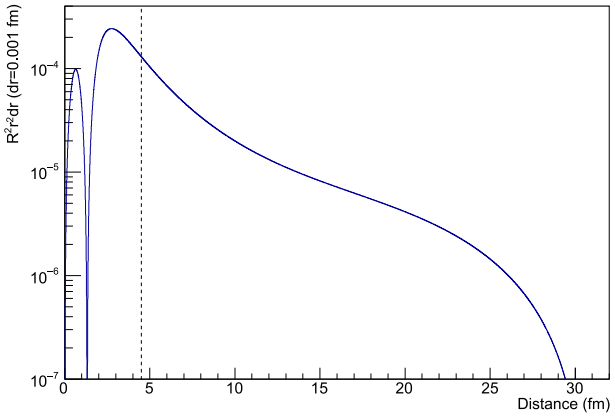

Fig. 27. The calculated proton wave function in ^{19}Ne*(E_x = 7.076 MeV) is shown as a function of the distance. It is assumed to be a pure $^{18}\mathrm{F}_{g.s.} \otimes \pi_{2s_{1/2}}$ structure. This state is unbound for proton emission, which poses some difficulties for calculating the wave function. In the present calculation, the outer part of the nucleus at distances greater than 30 fm, corresponding to an elastic scattering wave function, has been removed, and the inner part is renormalized to 1, i.e. $\int_0^\infty R^2_{sp}(r)r^2dr = 1$. The dashed line shows the position of the nucleus surface, i.e. $a = 1.25(A_p^{1/3} + A_{^{18}\mathrm{F}}^{1/3}) = 4.5$ fm. Calculations made with the DWUCK code [140].

– *Spin*. The choice of the projectile is strongly related to the spin of the state of interest. The (d, n) reaction, for example, generally has a positive Q-value, which makes low transferred angular momentum easier than in the (^{4}He, t) reaction. The reaction (^{4}He, t) on the contrary, has a large negative Q-value, which makes it easier to populate states with a high transferred angular momentum. This is illustrated in Fig. 28, where cross sections were calculated for different transfer reactions as a function of the beam energy. These reactions populate the same excited state E_x = 6.289 MeV of ^{19}Ne, but assuming different spin values. To summarize, if the excited state has a spin corresponding to a large $L = 4$ transferred angular momentum, it is better to use the (^{4}He, t) reaction which has the highest cross section, whereas $L = 0$ states are better populated in the (d, n) reaction. Angular momenta $L = 0$ are generally the most important for astrophysical reactions. It is the same for transfer reactions, i.e. $L = 0$ for the transferred particle, if a surrogate transfer reaction is used, e.g. $^{18}\mathrm{F}(d, n)^{19}\mathrm{Ne}(\alpha)^{15}\mathrm{O}$ to study the $^{18}\mathrm{F}(p, \alpha)^{15}\mathrm{O}$ reaction. Other transfer reactions are possible, such as $^{22}\mathrm{Na}(3^+)(p, \alpha)^{19}\mathrm{Ne}$, but in this case the states of interest ($1/2^+$ and $3/2^+$) are better populated with $L = 2$ for the transferred tritium.

7.4. Incident energy

The beam energy is chosen according to several criteria.

– The beam energy is chosen to optimize direct transfer compared with other reaction mechanisms. At low energy ($E \lesssim$ 15 MeV), the cross section is generally dominated by fusion–evaporation reactions, see Fig. 29. At high energy ($E \gtrsim$ 30 MeV/u, depending on the transferred angular momentum), many other reaction channels are open inducing an increase of the multi-step transfer contribution and a reduction of the direct transfer cross section. The optimum beam energy is determined by performing compound-nucleus calculations (with TALYS for example) and direct-transfer calculations (with FRESCO for example) and by choosing the energy where the compound-nucleus represents typically less than 1% of the direct-transfer cross section, depending on the spectroscopic factor aimed to be measured. In the case of the $^{18}\mathrm{F}(d, n)^{19}\mathrm{Ne}^{*}$ reaction, from the results presented in Figs. 29 and 30, it is clear that the energy of E_{lab} = 16.7 MeV ($E_{c.m.}$ = 14.9 MeV, or $E_{^{18}\mathrm{F}}$ = 150 MeV in inverse kinematics) [31,111,127] is optimum to study the $L = 0$ ($3/2^+$) states close to the proton emission threshold S_p = 6.410 MeV. At this energy, the direct transfer dominates the compound nucleus mechanism.
– For a precise choice of the beam energy, angular-momentum matching comes also into play. The cross section is a function of the transferred angular momentum. Indeed, the transfer reaction occurs at the radius r_t of the nucleus, and the angular momentum of the transferred particle is $L = \Delta p \times r_t$, where Δp is the transferred momentum, it follows that the greater the beam energy, the greater the transferred angular momentum, L, see Fig. 30.
– The beam energy must be chosen so that the reaction mainly takes place at the surface of the nucleus. This can be calculated with a DWBA code.

7.5. Target

Thin targets are often used in order to obtain good energy resolution and to separate the different levels in the excitation energy spectrum. For hydrogen and deuterium, a solid CH_2 or CD_2 plastic target is often used. It is a good idea to measure the contribution of the carbon atoms using a pure carbon target, and to subtract it from the measured spectrum. Another solution is to use a pure hydrogen target (gas, liquid or solid) [70,147].

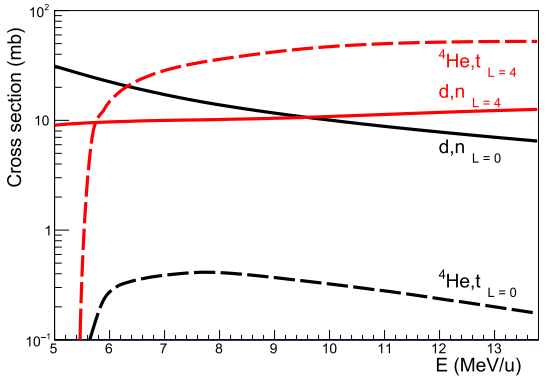

Fig. 28. The total cross sections for one-proton transfer reactions is calculated as a function of the incident energy. Low angular momentum states ($L = 0$, in black) are well populated with the (d, n) reaction (Q = −1 MeV/u), and higher angular momentum states ($L = 4$ in red) is well populated with the (^{4}He, t) reaction (Q = −4.9 MeV/u). The calculations were done for the transfer of one proton from the ^{18}F ground state to the E_x = 6.289 MeV excited state of ^{19}Ne, using the FRESCO code [77,78].

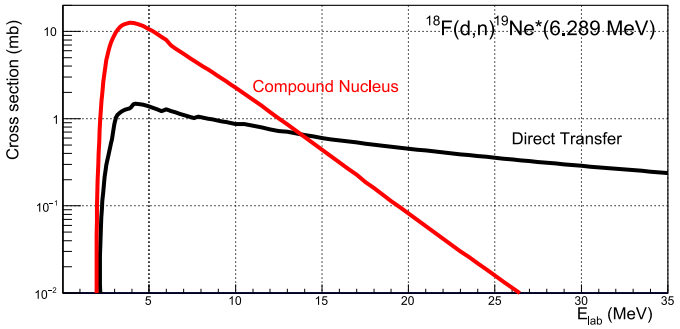

Fig. 29. The calculated cross sections for the ^{18}F$(d, n)^{19}$Ne*(E_x = 6.289 MeV, $J^\pi = 3/2^+$, $L = 0$) reaction are presented as a function of the incident energy in the laboratory. Black line: direct transfer mechanism (using FRESCO code with a spectroscopic factor equal to 0.01). Red line: compound nucleus formation ^{18}F+$d \rightarrow {}^{20}$Ne$^* \rightarrow {}^{19}$Ne$^* + n$ (TALYS code [148]).

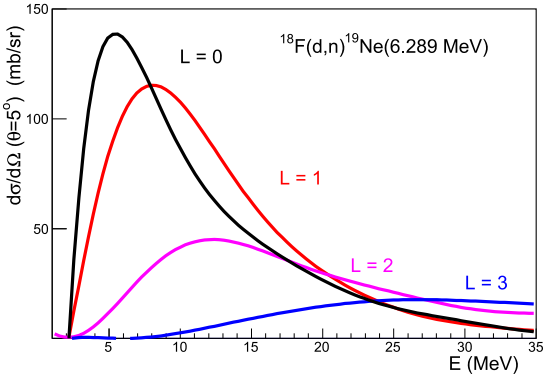

Fig. 30. The differential cross sections at the angle of 5° in laboratory of the ^{18}F$(d, n)^{19}$Ne* reaction populating the E_x = 6.289 MeV state are calculated for different transferred angular momenta as a function of the beam energy. The optimum energy increases with the transferred angular momentum.

7.6. Experimental setup

Several aspects need to be taken into account:

– The detection system should be optimized to measure the reactions products at the angles where the cross section is the highest. The maximum of the angular distribution is always located at forward angles in the center-of-mass system (see Fig. 32), corresponding in the laboratory system to forward angles in normal kinematics, and to backward angles in inverse kinematics.

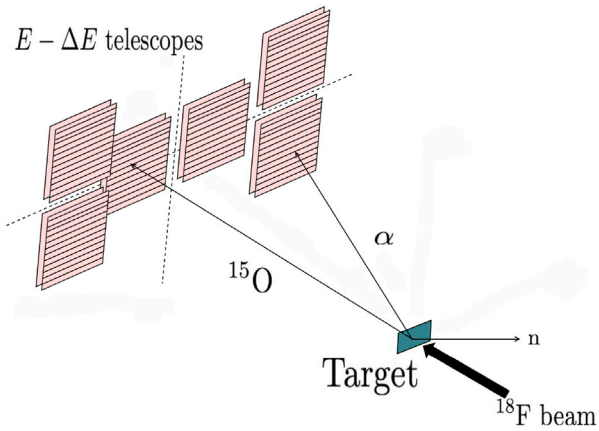

Fig. 31. Experimental setup used in the ^{2}H(^{18}F, n)^{19}Ne* transfer reaction. A set of silicon detectors was placed downstream of the target to measure the products of the ^{19}Ne$^{*}(\alpha)^{15}$O breakup reaction.
Source: From Ref. [111].

- Magnetic spectrometers, such as the SPLIT-POLE spectrometer [122], have been used extensively with stable beams for transfer measurements, in particular because they offer excellent energy resolution. As the intensity and optical quality of radioactive beams are generally lower than those of stable beams, large-acceptance spectrometers can be used.
- In most experiments involving radioactive nuclei, the reaction is measured in inverse kinematics with a radioactive beam. In this configuration, the energy of the ejectiles is strongly angle-dependent, which means that ejectiles have to be measured with good angular resolution in order to maintain a correct energy resolution. Moreover, at backward angles the energy separation between excited states in the laboratory is less than in the center of mass due to the kinematic compression [149]. For example, in the $d(^{18}\mathrm{F}, p)^{19}\mathrm{F}^{*}$ reaction at a bombarding energy of 16.7 MeV, excited states separated by 1 MeV in the center of mass are separated by 360 keV in the laboratory at $\theta_{lab} = 170°$ ($\theta_{c.m.} = 4°$). For this reason, the ISS and the SOLARIS solenoidal spectrometers have been developed at HIE-ISOLDE and FRIB [150,151]. They are designed so that charged light particles emitted during nuclear reactions are transported with high efficiency by a solenoidal magnetic field to a set of position-sensitive silicon detectors mounted on its axis. Measurement of the particle energies and interaction positions in the silicon array allows the Q value of the reaction to be determined with a 20–150 keV resolution, without the problem of kinematic compression. Obviously, this technique works for charged ejectiles only.
- In the case of the ^{2}H(^{18}F, n)^{19}Ne* reaction, the neutron would have to be measured at the rear angles, which is an additional complication. One good idea is to measure the breakup products, i.e. $^{19}\mathrm{Ne}^{*} \rightarrow {}^{15}\mathrm{O} + \alpha$ and $^{19}\mathrm{Ne}^{*} \rightarrow {}^{18}\mathrm{F} + p$. Fig. 31 shows the experimental setup used in the [111,127] experiment. Silicon detectors ($\Delta E - E$) were placed at the front angles (2.5–8.5° lab) to measure the ^{15}O nuclei (62 μm-thick ΔE), and at the higher angles (10.5–16.5° lab) to measure the α particles in coincidence. In this way, it was possible to reconstruct the ^{19}Ne* energy spectrum, the angular distributions of the populated states, and the partial widths for certain states [127].

7.7. Data analysis

The analysis is a matter of reconstructing the experimental cross section, angular distribution if it is possible, from the measured particles energies and angles, and analyzing it with DWBA calculations. There are several aspects to point out.

Energy spectrum. There are at least three ways of reconstructing the energy spectrum.

- The energy spectrum is obtained from the measured energies of the ejectiles, e.g. the energy of the triton particles in the reaction $^{19}\mathrm{F}(^{3}\mathrm{He}, t)^{19}\mathrm{Ne}^{*}$ [14,152].
- If the energy of the ejectile cannot be measured accurately (e.g. neutron ejectile) or the energy resolution is not good enough to distinguish the different excited states, the energy of populated states can be determined accurately by measuring the emitted γ-rays, e.g. $^{19}\mathrm{Ne}^{*}(\gamma)^{19}\mathrm{Ne}_{g.s.}$, detected in coincidence (or not) with the ejectiles or the recoil nucleus, see examples in Ref. [27]. This is possible only if the γ branching is high enough, which is not the case for all states in the $^{18}\mathrm{F}(p, \alpha)^{15}\mathrm{O}$ reaction. The result is both the good γ-ray energy resolution and the ejectiles angular distribution. It is also possible to measure only the γ rays, in which case the total cross section of the transfer reaction is measured [153,154]. In latter case it is not possible to check from the angular distribution that the transfer reaction is indeed direct, nor to deconvolute the different contributions when several transferred angular momenta are involved.
- The energy spectrum can be obtained from the breakup particles, e.g. $^{19}\mathrm{Ne}^{*} \rightarrow {}^{15}\mathrm{O} + \alpha$. The first step is to identify and measure the particles emitted in coincidence (using a $\Delta E - E$ telescope). Then, the relative energy of the breakup particles is

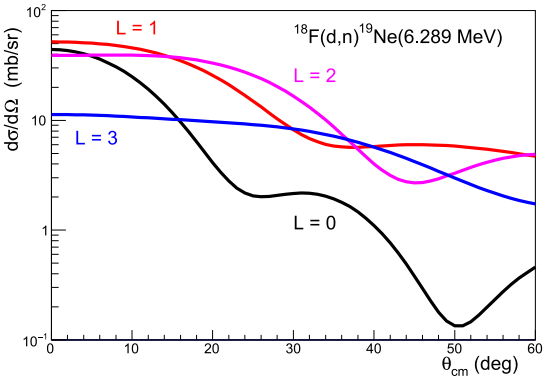

Fig. 32. Angular distributions of the n ejectiles produced in the transfer reaction ^{18}F$(d,n)^{19}$Ne* at E$_d$ = 16.7 MeV populating the E$_x$ = 6.289 MeV state. These distributions are calculated for different orbital angular momenta, and so, different spin and parity of the populated state.

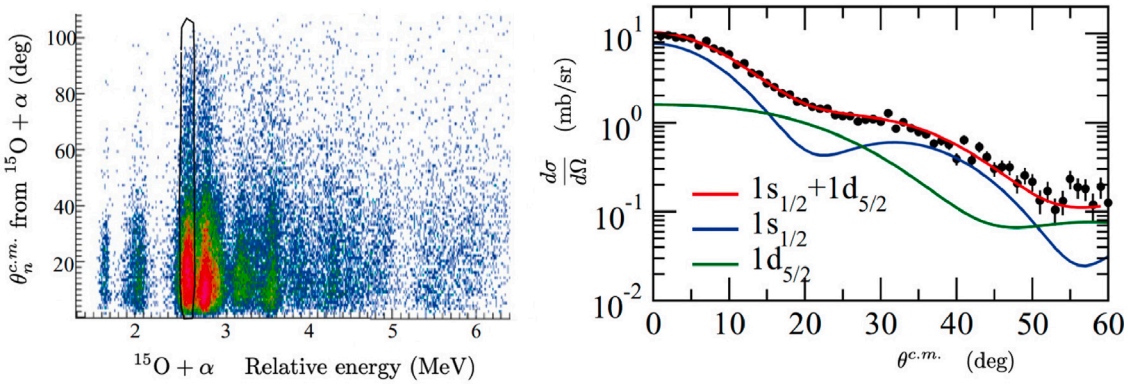

Fig. 33. (Left) In the ^{2}H(^{18}F, n)^{19}Ne$^* \rightarrow ^{15}$O + α breakup measurement [31,111], the angle of the neutron is shown as a function of the ^{15}O + α relative energy. States can be selected with a graphical cut. (Right) The neutron angular distribution for the 6289 keV state in ^{19}Ne. The measured angular distribution (black points) was reproduced using two transferred angular momenta ($L = 0$ s-wave, and $L = 2$ d-wave) and the corresponding two spectroscopic factors were used as free parameters to fit the data. Note that the neutron angle was not measured, it was reconstruct from momentum conservation.

reconstructed to a good approximation by

$$E_{rel} = \frac{E_\alpha E_{15_O} + m_\alpha c^2 E_{15_O} + m_{15_O} c^2 E_\alpha}{m_\alpha c^2 + m_{15_O} c^2} - \frac{\cos\theta \sqrt{E_\alpha^2 + 2m_\alpha c^2 E_\alpha}\sqrt{E_{15_O}^2 + 2m_{15_O} c^2 E_{15_O}}}{m_\alpha c^2 + m_{15_O} c^2} \tag{58}$$

where E_α, E_{15_O}, cos θ are the energies and relative angle between them in the laboratory. The NPTool Monte Carlo simulation and data analysis code [155,156] can also be used to analyse the data.

Then, the neutron energy, E_n, is determined from momentum conservation. The Q energy of the reaction is obtained with $Q = E_{rel} + E_n - E_{\text{beam}}$. The good events with $Q = 665$ keV, corresponding to the ^{2}H(^{18}F, α+^{15}O)n reaction, are selected [111]. Finally, the energy spectrum is calculated from the relation $E_x = S_\alpha + E_{\text{rel}}$ where $S_\alpha = 3529$ keV is the α emission threshold in ^{19}Ne.

Angular distribution. The angular distribution of the ejectiles is a function of the transferred angular momentum L, and therefore, of the spin of the state, as it is shown in Fig. 32. It is possible to determine the angular momentum of the transferred particle by comparing the experimental angular distribution with different theoretical solutions for different L. For example, a $L = 0$ proton transfer to the ground state of ^{18}F($J^\pi = 1^+$) lead to spin-parity $1/2^+$ or $3/2^+$ in ^{19}Ne. In some cases, the excited state can be populated by several angular momenta of the transferred particle. For example, the E$_x$ = 6.289 MeV state in ^{19}Ne*, which is expected to be $J^\pi = 3/2^+$, can be populated by $L = 0$ and $L = 2$ in the ^{18}F$(d,n)^{19}$Ne* transfer reaction. In this case, mixing contributions must be considered

$$\left(\frac{d\sigma}{d\Omega}\right)^{\text{exp}}_{^{18}\text{F}(d,n)^{19}\text{Ne}^*} = C^2S_{L=0}\left(\frac{d\sigma}{d\Omega}\right)^{DWBA}_{L=0} + C^2S_{L=2}\left(\frac{d\sigma}{d\Omega}\right)^{DWBA}_{L=2} \tag{59}$$

where $C^2S_{L=0}$ and $C^2S_{L=2}$ are the spectroscopic factors for the different transferred angular momentum, see Fig. 33. This is clearly related to the structure of this state: $\Psi(^{19}\text{Ne}^*) = c_1[^{18}\text{F}_{g.s.} \otimes \pi_{2s1/2}] + c_2[^{18}\text{F}_{g.s.} \otimes \pi_{1d3/2}]$, as discussed herebefore.

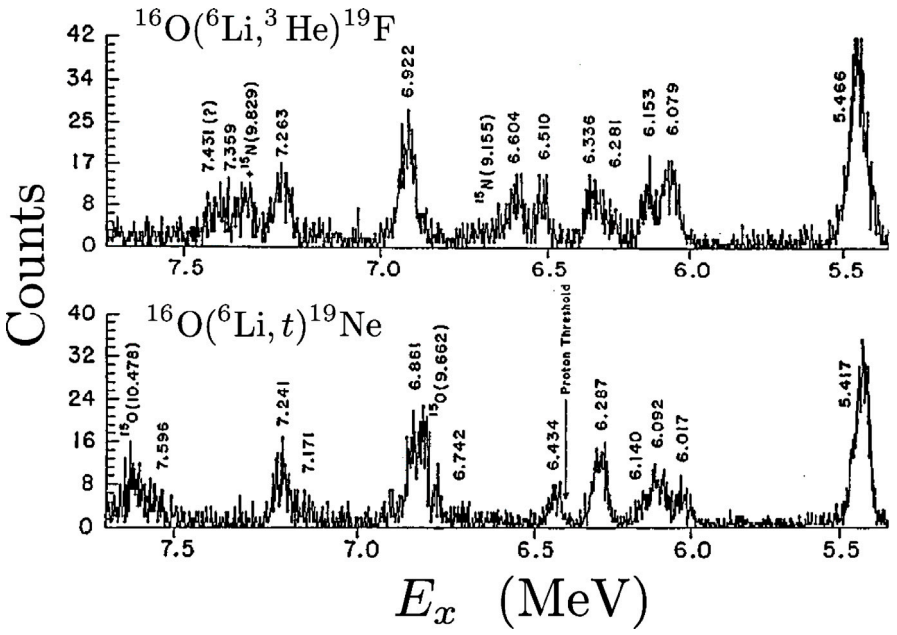

Fig. 34. Comparison between the excitation energy spectrum measured in the ^{16}O(^{6}Li, ^{3}He)^{19}F transfer reaction (a tritium cluster transfer reaction) and the one measured for the ^{16}O(^{6}Li, t)^{19}Ne mirror reaction. One would expect the two spectra to be almost identical, given the mirror symmetry of the nuclear force. This comparison is used to constrain the spins of the ^{19}Ne states, since many states are known in ^{19}F.
Source: From Ref. [14].

Spins. The spin of the states can be obtained by measuring the angular distribution of the ejecta, as discussed above. It can also be constrained by a comparison between the spectrum measured for one reaction and the spectrum measured for the mirror reaction. The Utku et al. article [14] is considered to be an important reference about the ^{18}F(p, α)^{15}O reaction. It has made a particular impression by comparing the spectrum measured for the ^{16}O(^{6}Li, ^{3}He)^{19}F reaction with the one measured for the ^{16}O(^{6}Li, t)^{19}Ne mirror reaction. One would expect the two spectra to be virtually identical, given the mirror symmetry of the nuclear force: the most populated states on one side should correspond to the most populated states on the other. This similarity between the two spectra can indeed be seen in Fig. 34. The ^{19}F states are well known, so it could be easy to constrain the ^{19}Ne mirror states. It turns out that the exercise is particularly difficult in this case, as the density of states is high close to the threshold and the states are difficult to separate.

Optical model potentials. The DWBA calculation requires knowledge of the optical potentials of the various reaction channels. It is advisable to measure the elastic scattering in the entrance channel during the experiment, so that the optical potential can be determined precisely in the same experimental conditions, i.e. for these isotopes at the same beam energy. The most common problem is the difficulty of knowing precisely the optical potential in the output channel, especially if this involves a radioactive isotope and an excited state of that nucleus. Tables of potentials are available giving a wide range of examples [157], and it is usually possible to guess a good set of parameters.

Partial widths. The partial widths of the excited states populated by transfer reactions can be determined from their measured spectroscopic factors. However, it is also possible to determine branching ratios, and therefore constrain partial widths, by measuring their decay products. For example, in Ref. [14], the ^{19}F(^{3}He, t)^{19}Ne* transfer reaction was measured in coincidence with the ^{19}Ne* $\rightarrow^{15}$O + α and ^{19}Ne* $\rightarrow^{18}$F + p breakup channels. The t ejectiles were measured with a QDDD magnetic spectrometer. Decay products were measured with silicon detectors placed at 90°, 110° and 145° around the target, and the measured angular distributions were fitted with a linear combination of $L = 0, 2, 4$ Legendre polynomials to deduce the total yield of decays proton and α particles for each triton group and thereby its $\frac{\Gamma_p}{\Gamma}$ and $\frac{\Gamma_\alpha}{\Gamma}$ decay branching ratios.

Transfer of clusters. DWBA can also be used for multi-particle transfer, see the example of the ^{15}N(^{7}Li, t)^{19}F α transfer reaction [137,158]. Without going into detail, the cluster of particles is treated as a single particle. The wave function of the cluster is calculated with a Woods–Saxon potential and the number of nodes N of the wave function is determined from the energy condition $2N + L = \sum_i 2n_i + l_i$, where the sum runs over the transferred nucleons with (n_i, l_i) taken from the shell model [137,159].

7.8. Limitations

The transfer reaction is applied extremely often in nuclear structure studies, but it has some limitations which are presented below.

- In many experiments, the targets are not pure, and the transfer spectrum is contaminated by peaks from transfer reactions on contaminants. It is recommended to plan background measurements with different targets.
- In general, DWBA calculation codes are unable to handle unbound states. Furthermore, unbound states are states whose energy is not well defined (resonance). Very often, the wave function is calculated assuming a bound state with a very low binding energy. This method gives a good estimate of the spectroscopic factors for states that are very close to the particle emission threshold [160].
- Breakup reactions can produce a continuous background in the measured excitation energy spectrum [161], starting from a certain energy threshold, which is superimposed on the discrete peaks produced by the direct transfer reaction. For example, in the ^{16}O(^{6}Li, t)^{19}Ne* reaction, there could be a continuous contribution from the ^{6}Li $\rightarrow$ t+^{3}He breakup reaction.
- Transfer reactions can occur in several steps. For example, the (^{7}Li, t) reaction can occur in one step with the direct transfer of one α particle, or in two steps with a transfer of one neutron (^{7}Li, ^{6}Li) followed simultaneously by the transfer of a ^{3}He nucleus (^{6}Li, t). In general, it is not possible to know whether the transfer reaction is direct, which is a condition for the validity of the Eq. (49). A good agreement between the shape of the experimental and theoretical angular distribution is a good argument to justify that the reaction is direct. It can also be stated that, on the basis of theoretical predictions, the measured cross section should be mainly direct at certain beam energies. Alternatively, the compound nucleus or multi-step transfer cross section can be calculated and subtracted from the measured cross section to deduce the direct transfer cross section.
- A given transfer reaction cannot populate all the excited states of the recoil nucleus [162]. For example, ^{19}Ne states are populated by the ^{20}Ne(p, d)^{19}Ne* pick-up reaction [70]. Since the ^{20}Ne ground state is composed of 10 protons and 10 neutrons placed mainly on the s, p and d nuclear shells, then the pick-up of one neutron from one of these shells cannot produce a ^{19}Ne excited state with, for example, a $7/2^{-}$ spin. The spectroscopic factor for this transfer reaction is predicted to be zero or very small. If this state is observed in the transfer experiment, it probably means that the transfer occurred in a multi-steps process, or through the formation of the compound nucleus. The DWBA analysis is therefore not valid.
- In general, if the measured spectroscopic factor is very small, there is room for doubt about the accuracy of the measurement, since the transfer model is based on the description of the state as consisting of a core nucleus and the transferred particle, which is contradicted by the measurement.
- As shown in Eq. (57), the width of a state associated with the particle emission is proportional to the spectroscopic factor of that particle and to the probability of finding the particle on the surface of the nucleus at $r = a$

$$\Gamma(E) \propto C^2S \times a^2R^2(a) \tag{60}$$

  Similarly, the cross section of the transfer reaction is proportional to the spectroscopic factor and to the probability of finding the particle at the position where the particle transfer occurs, $r = r_t$.

$$\frac{d\sigma}{d\Omega}_{\text{transfer}} \propto C^2S \times r_t^2R^2(r_t) \tag{61}$$

  The position, r_t, depends on the beam energy of the transfer reaction. To explore the radial dependence of the transfer cross section [163,164], we might plot the nuclear matrix element, i.e. Eq. (47). It is not easy to extract this element in usual codes because they work in finite range, in which case the DWBA transfer amplitude depends on the so-called non-local kernels, which are functions of both the entrance and exit projectile–target coordinates.
  A simpler way of testing the radial dependence of the transfer reaction is to study the region of sensitivity with respect to the relevant overlap function. For the ^{18}F(d, n)^{19}Ne* transfer reaction, we are interested in the region of sensitivity with respect to the ^{18}F + p coordinate. In the FRESCO code, one can use the variable RSMIN for the ^{19}Ne =^{18}F + p overlap that restricts the radial integration to $r >$ RSMIN. In this way, one can infer the region of sensitivity with respect to this variable. The results are shown in Fig. 35 for two different beam energies. One can notice that, at the energy of 12.6 MeV the transfer reaction takes place mostly on the surface of the nucleus. The cross section is divided by 2 with RSMIN = 6.2 fm. It happens much further inside the nucleus at the energy of 60 MeV ($r_t \approx 2$ fm). The cross section is divided by 2 with RSMIN = 2.2 fm. The spectroscopic factor determined at 12.6 MeV with the transfer reaction can be used directly to calculate the width of the state, but it is likely that a factor still needs to be applied to correct for the not-so-well-defined surface of the nucleus.
- The exact equivalence between the spectroscopic factor determined by transfer reaction, and the spectroscopic factor used in astrophysics, was questioned [165]. Systematic uncertainties must be taken into account. Typically, differences of a few % are observed when using different codes, differences of 15% for different optical potentials or different potentials for bound states, and differences of the order of 20% for different calculation parameters in the DWBA calculations, which gives a final uncertainty of the order of 30%. It is found that the relative values between several states measured in the same experiment are reliable with accuracy better than 25%, and absolute measured values with accuracy $\geq$30%, see Ref. [111,137].
- For bound states or sub-threshold resonances (state below threshold with resonance tail seen above threshold), it is possible to perform the transfer reaction at low beam energies, below the Coulomb barrier. In this case, the transfer reaction probes a part of the wave function located further away from the nucleus surface, which always follows an asymptotic function that does not depend on potential models parameters, i.e. the $W(r)$ Whittaker W-function [166]. It is convenient to parametrize

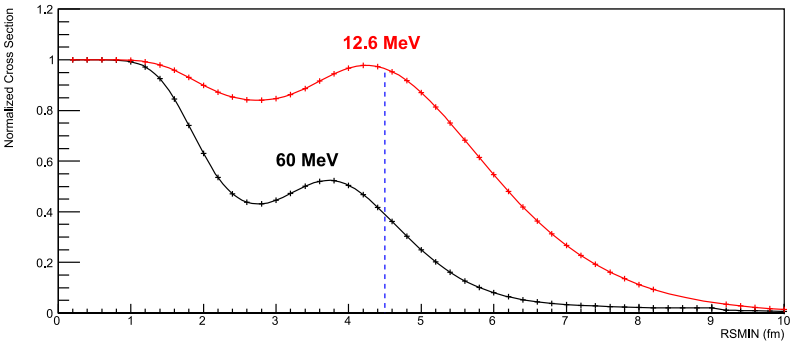

Fig. 35. The normalized total cross section is shown as a function of the RSMIN parameter. This is calculated with the FRESCO code for the ^{18}F$(d,n)^{19}$Ne* transfer reaction to the $3/2^+$ state at E_x = 6289 keV in ^{19}Ne at two beam energies, 60 MeV and 12.6 MeV. The RSMIN parameter is used to set the overlap form factor to zero inside the interval $r <$ RSMIN in the ^{19}Ne $=^{18}$F + p system [163,174]. The radius of the ^{19}Ne nucleus is shown with the vertical dashed line. The effect of the RSMIN parameter becomes noticeable (significant reduction of the cross section) at RSMIN = 1.7 fm at an incident energy of 60 MeV, and at 5.2 fm at 12.6 MeV. This shows that the transfer reaction occurs mostly at the surface of the nucleus ($r \approx 5$ fm) at 12.6 MeV, and much deeper inside ($r \approx 2$ fm) at 60 MeV.

this dependence by an Asymptotic Normalization Coefficient (ANC), such that

$$C^2S \times r^2R(r)^2 = (ANC)^2W(r)^2. \tag{62}$$

The ANC coefficient can then be used directly in R-Matrix code to calculate the astrophysical cross section. The advantage is that it is a less-model-dependent way of determining the cross section.

– In principle, mirror nuclei share the same mirror structure, thus the spectroscopic factors for two mirror states are identical. It is therefore possible to measure the spectroscopic factor of a state by studying its mirror state, if this proves to be easier experimentally. In practice, the equality of the two spectroscopic factors is not necessarily true [167]. It has been shown that the coupling of discrete states to the continuum, to particle emission, can induce a modification of the structure of the state and therefore of its spectroscopic factor by a factor larger than a factor 2 [167,168].

8. Trojan Horse method

8.1. Principle

The Trojan Horse Method (THM) was first proposed in 1986 by G. Baur [169]. The experimental method has been developed mainly by the group of C. Spitaleri in Laboratori Nazionali del Sud (Catania, Italy) to determine astrophysical cross sections in the Gamow window, and used to study twenty or so cases [79,170–173]. It was recently applied for the first time to radioactive beams [30], to study the ^{18}F$(p,\alpha)^{15}$O case.

The principle of the THM is illustrated in Fig. 36. To date, this method has only been applied to (particle,particle) reactions (no γ-ray), which is the case for the ^{18}F$(p,\alpha)^{15}$O astrophysical reaction. The cross section of the latter reaction was determined by measuring the three-body reaction $d(^{18}\mathrm{F},n\,\alpha)^{15}$O. The transferred nucleon, one proton in the present case, is hidden inside the Trojan Horse (TH) nucleus ($d = p+n$). Within certain conditions, called *Quasi-Free* (QF) reaction mechanism, the $d(^{18}\mathrm{F},n\,\alpha)^{15}$O reaction can be regarded as a two-step process. First, the d projectile approaches the ^{18}F nucleus and breaks up within the nuclear field of the nucleus. The proton reacts with ^{18}F forming the compound-nucleus ^{19}Ne*, whereas the neutron does not interact, it is a *spectator* of the reaction. Then, ^{19}Ne* decays to α+^{15}O. At least two of the three outgoing particles are measured in coincidence in the exit channel, in the present case it was α and ^{15}O [30]. The measured energies and angles are used to reconstruct the center-of-mass energy of ^{19}Ne*, and the p+^{18}F reaction energy. The cross section of the QF reaction is proportional to the ^{18}F$(p,\alpha)^{15}$O cross section. As the beam energy is greater than the Coulomb barrier, the QF reaction is not affected by Coulomb suppression or electron scattering effects, therefore with much higher cross section than the direct measurement of the ^{18}F$(p,\alpha)^{15}$O reaction.

8.2. Theory

The TH reaction is a transfer reaction that is carried out under specific conditions, by selecting events measured under certain kinematic conditions and at a precise beam energy. The THM has been applied in nuclear astrophysics to determine cross sections at very low energies, or to determine the strengths of unknown resonances relatively to known resonances.

Determining cross sections at low energies. In the theoretical description of the *Plane Wave Impulse Approximation* (PWIA) [79,171,175,176], it is possible to show that the three-body breakup cross section is related to the two-body cross section

$$\left(\frac{\mathrm{d}^3\sigma}{\mathrm{d}E_{^{15}\mathrm{O}\alpha}\mathrm{d}\Omega_\alpha\mathrm{d}\Omega_{^{15}\mathrm{O}}}\right)^{c.m.}_{^{18}\mathrm{F}(d,\alpha\ n)^{15}\mathrm{O}} = K|\Phi(\mathbf{p}_{pn})|^2\left(\frac{\mathrm{d}\sigma}{\mathrm{d}\Omega}\right)^{\text{c.m. HOES}}_{^{18}\mathrm{F}(p,\alpha)^{15}\mathrm{O}} \tag{63}$$

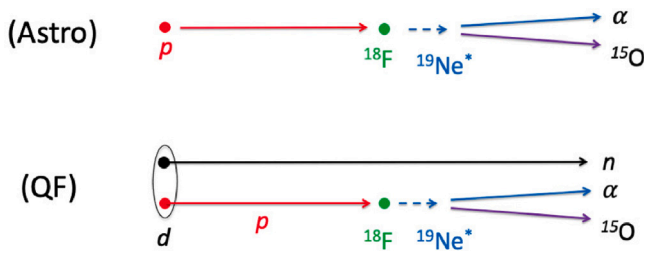

Fig. 36. (ASTRO) The ^{18}F(p, α)^{15}O astrophysical reaction proceeds through the formation of the compound-nucleus ^{19}Ne*. (QF): Quasi-Free mechanism. Particle p is hidden inside the Trojan Horse projectile d ($d = p + n$), and impinges upon nucleus ^{18}F to form compound-nucleus ^{19}Ne*. Particle n does not interact, it is a *spectator* of the reaction.

where

- K is a kinematic factor. It is a function of the masses, momenta, and angles of the outgoing particles.
- The term $\Phi(\mathbf{p}_{pn})$ is the momentum distribution of the $p+n$ inter-particle motion inside the TH nucleus (d before reaction). Indeed, even if the beam energy is well defined, this does not mean that the measurement is made at a single reaction energy in the center of mass. This is because, inside a bound nucleus, the nucleons are naturally agitated, this is the Fermi motion. The proton–neutron momentum distribution measured and calculated inside the deuteron nucleus are shown in Fig. 37. Quantum mechanics tells us that this internal momentum, of particles p and n inside d, is on average equal to zero, with a dispersion typically of the order of
$$p_{pn}^{lim} \approx \sqrt{2\mu_{pn}\mathrm{BE}(p+n)} \approx 45 \text{ MeV/c} \tag{64}$$
where μ_{pn} is the reduced mass of $p+n$ system, and BE($p+n$) the binding energy of d. This internal motion has to be added to the incident projectile velocity v_p. This implies that the effective energy of the proton when it interacts with ^{18}F, $E^{c.m.}_{p^{18}\mathrm{F}}$, is not limited to one single incident energy. In reality, a wider range of incident energies is explored in the same experiment using a single beam energy. The larger is the binding energy, the larger is the energy window. Since the transferred particle in the TH reaction is "virtual", its energy and velocity are not related by the classical equation of motion $E_p = 1/2\ m_p\ v_p^2$. Such a physical system is called to be *off the energy shell* (OES).
- The term $\left(\frac{\mathrm{d}\sigma}{\mathrm{d}\Omega}\right)^{\mathrm{HOES}}_{^{18}\mathrm{F}(p,\alpha)^{15}\mathrm{O}}$ is the *half-off-energy-shell* differential cross section for the astrophysical two-body reaction ^{18}F(p, α)^{15}O. It is *half* since the initial momentum is off-shell and the final momentum is on-shell.

The astrophysical differential cross section can be deduced from
$$\left[\frac{\mathrm{d}\sigma}{\mathrm{d}\Omega}(E^{c.m.}_{^{15}\mathrm{O}\alpha}, \theta^{c.m.})\right]^{\mathrm{astro}} \propto P_{\ell}(E^{c.m.}_{^{18}\mathrm{F}p}) \left[\frac{\mathrm{d}\sigma}{\mathrm{d}\Omega}(E^{c.m.}_{^{15}\mathrm{O}\alpha}, \theta^{c.m.})\right]^{\mathrm{HOES}} \tag{65}$$
where $P_{\ell}(E^{c.m.}_{^{18}\mathrm{F}p})$ is the penetrability function through the Coulomb barrier of the system ^{18}F + p. And so, the total cross section is
$$\sigma(E^{c.m.}_{^{18}\mathrm{F}p})^{\mathrm{astro}} = \int \left[\frac{\mathrm{d}\sigma}{\mathrm{d}\Omega}(E^{c.m.}_{^{18}\mathrm{F}p}, \theta^{c.m.})\right]^{\mathrm{astro}} \mathrm{d}\Omega \propto P_{\ell}(E^{c.m.}_{^{18}\mathrm{F}p}) \int \left[\frac{\mathrm{d}\sigma}{\mathrm{d}\Omega}\right]^{\mathrm{HOES}} \mathrm{d}\Omega \tag{66}$$
Usually, the measured astrophysical cross section is normalized to high energy where $P_L(E^{c.m.}_{^{18}\mathrm{F}p}) \simeq 1$.

Determining the resonance strength. Each resonance in the ^{18}F(p, α)^{15}O reaction contributes to the rate of the reaction in proportion to the strength of the resonance
$$\omega\gamma \equiv \frac{(2J_r+1)}{(2J_{^{18}\mathrm{F}}+1)(2J_p+1)} \frac{\Gamma_{^{15}\mathrm{O}\alpha}\Gamma_{^{18}\mathrm{F}p}}{\Gamma_T} \tag{67}$$
where $\Gamma_{^{15}\mathrm{O}\alpha}$, $\Gamma_{^{18}\mathrm{F}p}$ and Γ_T are the partial and total widths of the resonance. In the case of an isolated resonance, the Breit–Wigner formula can be used to calculate the THM reaction [175,177] and then, the number of counts N_r measured in the resonance is
$$N_r \propto \int |M(x)|^2 \frac{\Gamma_{^{15}\mathrm{O}\alpha}(x)}{(x-E_r)^2 + \frac{\Gamma_T^2(x)}{4}} \mathrm{d}x \propto \frac{\Gamma_{^{15}\mathrm{O}\alpha}(E_r)}{\Gamma_T(E_r)} |M(E_r)|^2 \tag{68}$$
where

- E_r is the resonance energy
- $M(x)$ is called *generalized form factor*, or *direct transfer reaction amplitude*, and can be calculated [177].

Then
$$\omega\gamma \propto \frac{(2J_r+1)}{(2J_{^{18}\mathrm{F}}+1)(2J_p+1)} \frac{N_r}{|M(E_r)|^2} \Gamma_{^{18}\mathrm{F}p} \tag{69}$$

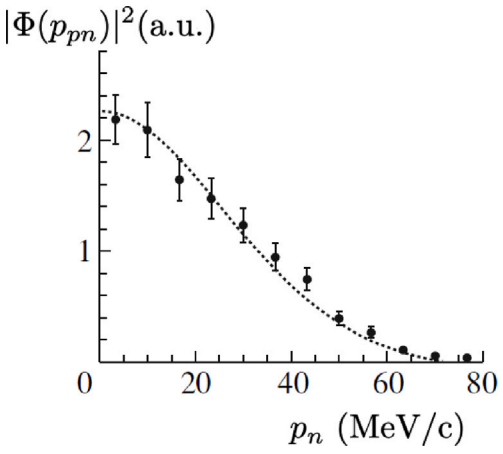

Fig. 37. Experimental proton–neutron momentum distribution inside the deuteron nucleus (dots) extracted from the ^{2}H(^{11}B, α ^{8}Be)n reaction compared with the predicted distribution (dotted curve). The maximum of the (L = 0) distribution is observed at the spectator momentum p_n = 0 MeV/c. The dispersion is $p_{pn}^{lim} \approx 45$ MeV/c.
Source: From Ref. [172].

Table 2
List of possible Trojan Horse nuclei.

TH nucleus	Structure	Binding energy (MeV)
^{2}H	$p+n$	2.22
^{3}H	$d+n$	6.26
^{3}He	$p+d$	5.49
^{6}Li	$d+\alpha$	1.47
^{14}N	$d+^{12}$C	10.27
^{16}O	$\alpha+^{12}$C	7.16

If several isolated resonances are measured in the same experiment, and if one of the resonances is known, it is possible to determine the strengths of the unknown resonances by measuring their peak integral relatively to the known one

$$(\omega\gamma)_i = (\omega\gamma)_j \frac{N^i}{N^j} \frac{(2J_{r_i}+1)}{(2J_{r_j}+1)} R_{ij} \tag{70}$$

where

$$R_{ij} = \frac{|M(E_r^j)|^2}{\Gamma^j_{^{18}\mathrm{F}p}} \frac{\Gamma^i_{^{18}\mathrm{F}p}}{|M(E_r^i)|^2} \tag{71}$$

It is possible to show that the dependence on unknown spectroscopic factors are completely removed in these ratios, and that R_{ij} can be calculated using the *R matrix* formalism [175,177]. In this way, the strength of an unknown resonance can be determined from the number of counts measured in this resonance.

8.3. Experimental setup

Fig. 38 shows a typical experimental setup that could be used to study the^{18}F(p, α)^{15}O reaction with the $d(^{18}\mathrm{F}, n\ \alpha)^{15}$O TH reaction. Two out of the three reaction products must be detected with typical energy and angular resolution of 1% and 0.1–0.2° respectively. After the reaction, the ^{15}O recoiling nucleus is detected at small angles. In a typical THM experiment, α and ^{15}O particles are measured in coincidence with position sensitive detectors. The detector angles are chosen to maximize the quasi-free contribution. Usually, particles are identified using a ΔE-E telescope of detectors or using kinematics conditions (θ versus angle). Energy losses are measured in an ionization chamber or in a thin silicon detector.

8.4. Beam and target

The intensity of the beam is of the order of a few nAe with stable beams, or larger than 10^5 pps with radioactive beams (5 and 3–4 $\times 10^5$ ^{18}F ions/s in Ref. [30,178]).

Target thickness is typically 10–1000 μg/cm^2. Several good TH candidates are presented in Table 2. In the ^{18}F(p, α)^{15}O reaction, a suitable TH nucleus should have a proton structure, then d and ^{3}He are good candidates.

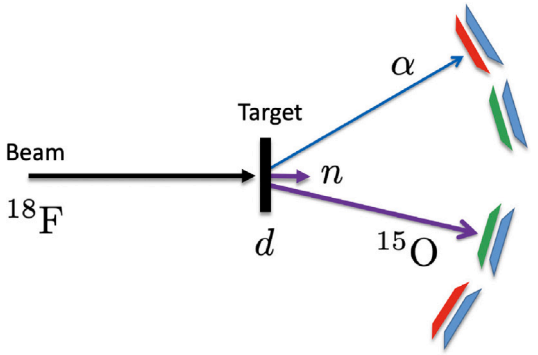

Fig. 38. Typical experimental setup used in Trojan Horse experiments, here applied to the $d(^{18}\mathrm{F}, n\ \alpha)^{15}\mathrm{O}$ reaction. Particles α are identified using a ΔE-E telescope of position sensitive silicon detectors (in red), whereas ^{15}O nuclei are measured with an ionization chamber (in green) and a silicon detector. Beam tracking detectors (PPAC) were placed upstream the target in order to reconstruct the incident angle with a good resolution (0.14° in [30]).

8.5. Incident energy

The incident energy $E^{lab}_{^{18}\mathrm{F}}$ of the ^{18}F projectile is chosen to be large enough to pass through the Coulomb barrier in the ^{18}F+d entrance channel, thereby the proton (inside d) is brought into the interior of ^{18}F to induce the $d(^{18}\mathrm{F}, n\ \alpha)^{15}\mathrm{O}$ reaction

$$E^{lab}_{^{18}\mathrm{F}} \gtrsim \frac{m_d + m_{^{18}\mathrm{F}}}{m_{^{18}\mathrm{F}}} \times 0.6\ \mathrm{MeV} \times \frac{Z_d\ Z_{^{18}\mathrm{F}}}{(A = 18)^{1/3}} \tag{72}$$

It is supposed that the neutron (inside d) is "spectator" to the reaction between p and ^{18}F, see Fig. 36. This assumption is often referred to as a quasi-free scattering or *quasi-free condition* (QF). Experimentally it means that only events with small momentum transferred to the spectator particle should be selected, i.e. $\Delta p_n \approx 0$. Therefore, the fraction of the beam energy pertaining to the proton is (in direct kinematics when d is the beam)

$$E^{lab}_{p} = \frac{m_p}{m_d} E^{lab}_{d} \tag{73}$$

and the energy available in the center of mass of p+^{18}F is

$$E^{c.m.}_{p^{18}\mathrm{F}} = \frac{m_{^{18}\mathrm{F}}}{m_p + m_{^{18}\mathrm{F}}} E^{lab}_{p} = \frac{m_{^{18}\mathrm{F}}}{(m_p + m_{^{18}\mathrm{F}})} \frac{m_p}{m_d} E^{lab}_{d} \tag{74}$$

A part of that energy is used to break up the TH nucleus d into $p + n$, what remains is the effective center-of-mass energy

$$E^{c.m.}_{p^{18}\mathrm{F}}(\mathrm{effective}) = E^{c.m.}_{p^{18}\mathrm{F}} - \mathrm{BE}(p + n) \tag{75}$$

with $\mathrm{BE}(p + n)$ the binding energy of the TH.

The energy of the beam is chosen such as $E^{c.m.}_{p^{18}\mathrm{F}}(\mathrm{effective}) = E_G$, the Gamow energy in the two-body reaction. It follows that the beam energy needed to induce the 3-body reaction to study the 2-body astrophysical reaction is

$$E^{lab}_{d} = \frac{m_d(m_p + m_{^{18}\mathrm{F}})}{m_{^{18}\mathrm{F}}\ m_p}(E_G + \mathrm{BE}(p + n)) \tag{76}$$

or, in inverse kinematics (the TH nucleus is at rest)

$$E^{lab}_{^{18}\mathrm{F}} = \frac{m_p + m_{^{18}\mathrm{F}}}{m_p}(E_G + \mathrm{BE}(p + n)) \tag{77}$$

To determine the astrophysical reaction rate, it is necessary to know its cross section for all energies within the Gamow window. In the THM, it is not necessary to change the beam energy to measure the whole Gamow window. The entire measurement is done in a single experiment, thanks to the off-the-energy-shell effect. Different examples of reactions, beams and energy windows are given in Table 3.

Moreover, with the THM it is also possible to study sub-threshold resonances. This is due to the fact that the TH reaction can have energy threshold located below the astrophysical reaction threshold, see for instance the case of ^{13}C(^{6}Li, n^{16}O)d in Fig. 39.

8.6. Monte Carlo simulations

Monte Carlo simulations are used to determine and to optimize several important parameters of the experiment, including the angles of the detectors, detection efficiency, particles energies, space phase normalization etc. The object-oriented data analysis code ROOT [103] can be used to simulate easily the three-body space phase of the reaction through the *TGenPhaseSpace* C++ utility class. For instance, in the case of the reaction ^{6}Li(^{6}Li, $\alpha\alpha$)^{4}He, simulations show that the first α-particle can be detected at 60° with energy ≈14.6 MeV in coincidence with the second one at 73° with energy ≈12.5 MeV, in agreement with experiment, see Fig. 40.

Table 3
Different examples of reactions of astrophysical interest studied with the THM.

Astrophysical reaction	Trojan Horse reaction	E_{beam}^{lab} (MeV)	E_G[a] (MeV)	Energy window[b] (MeV)	Ref.
^{6}Li(d, α)^{4}He	^{6}Li(**^{6}Li**, $\alpha\alpha$)^{4}He	6.0	0.03	[−2.9,+1.2]	[179–182]
^{13}C(α, n)^{16}O	^{13}C(**^{6}Li**, n^{16}O)d	7.82	2.5	[−1.1,+3.8]	[183]
^{12}C(^{12}C, α)^{20}Ne	^{12}C(**^{14}N**, α^{20}Ne)d	30	2.6	[−4.6,+3.5]	[184]
^{18}F(p, α)**^{15}O**	**d**(^{18}F, α^{15}O)n	47.9	0.3	[−3.1,+2.3]	[30,178,185]
^{18}O(p, α)^{15}N	**d**(^{18}O, α^{15}N)n	54	0.6	[−3.9,+2.9]	[177,186,187]

[a] From Eqs. (76) and (77).
[b] From Eq. (64) and Monte Carlo simulations.

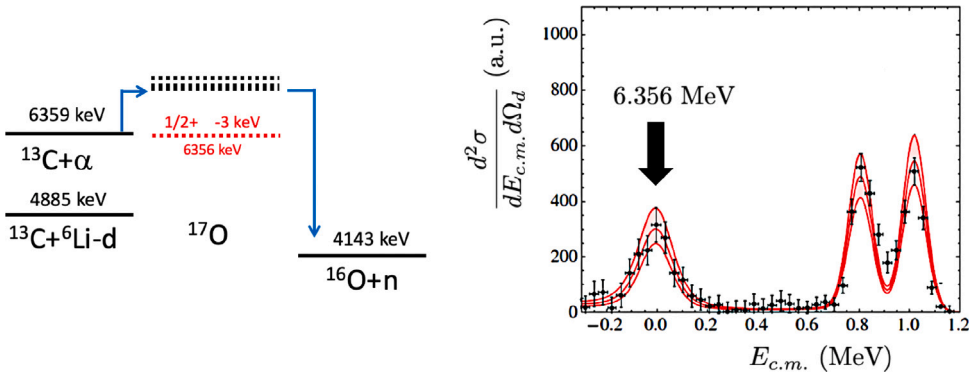

Fig. 39. Left: Energy diagram. The energy threshold of the Trojan Horse reaction ^{13}C(^{6}Li, n^{16}O)d is located under the energy threshold of the astrophysical reaction ^{13}C(α, n)^{16}O. This latter reaction is extremely important since it provides neutrons in the astrophysical s-process. At low energy, this reaction proceeds mostly through the tail of the sub-threshold resonance $J^{\pi} = \frac{1}{2}^{+}$, E_x = 6.356 MeV, E_r = −3 keV. Right: Measured spectrum with the Trojan Horse reaction ^{13}C(^{6}Li, n^{16}O)d. The sub-threshold resonance is clearly visible.
Source: From Ref. [183].

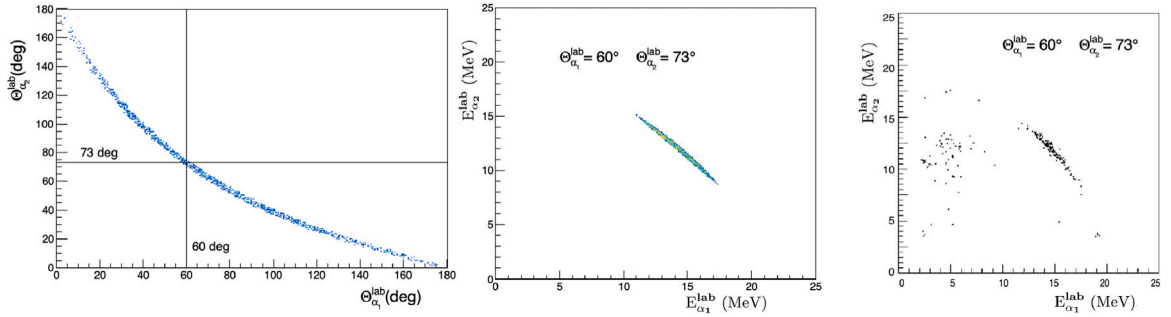

Fig. 40. Left: Monte Carlo simulation of the reaction ^{6}Li(^{6}Li, $\alpha_1\alpha_2$)α_s. The angle of α_2 is shown as a function of the angle of α_1 after selecting the quasi-free events (α_s is at rest in lab). Center: Energy E_{α_2} as a function of the energy E_{α_1} for the particles selected at $\Theta_{\alpha_1} = 60°$ and $\Theta_{\alpha_2} = 73°$. Right: Data from Ref. [181], this is in agreement with the simulations.

8.7. Data analysis

There are 3 main steps in the analysis of THM data.

1. *Selection of the three-body reaction*
   The objective of the first step is to select events corresponding to the TH reaction.

   – In most experiments only 2 particles are detected, in the case of the $d(^{18}\mathrm{F}, n\ \alpha)^{15}$O experiment it was α and ^{15}O. The heavy recoil nucleus (^{15}O) is identified in charge Z, and sometimes in mass A, using a ΔE-E plot, see one example in Fig. 41 (left).
   – For these selected events, energy of ^{15}O is plotted versus the energy of particles b detected in coincidence, see Fig. 41 (center). The events corresponding to the $d(^{18}\mathrm{F}, n\ \alpha)^{15}$O reaction can be singled out by comparison with a Monte Carlo simulation of the TH process, taking into account detection thresholds, energy losses and the kinematics of the TH

reaction.
- For these selected events, the reaction Q value is determined. A cut is made on the Q value to choose the ground state of ^{15}O, see Fig. 41 (right).

2. *Selection of the Quasi-Free events*
In the previous step, the events corresponding to the $d(^{18}\mathrm{F}, n\ \alpha)^{15}\mathrm{O}$ reaction have been selected. The objective of the second step is to select the events of QF-type mechanism. Indeed, the measured events may have been produced by different reaction mechanisms: Quasi-Free mechanism (QF), Compound Nucleus formation (CN), Two-Step Transfer. The idea now is to select the events that proceed through the QF mechanism only. This is an essential step since the aforementioned equations are valid only under the assumption that the neutron of the $d(^{18}\mathrm{F}, n\ \alpha)^{15}\mathrm{O}$ reaction acts as a spectator to the ^{18}F+p reaction. This selection is accomplished in several steps by a thorough study of the data.

- The CN produces three exit channels that can mix with the QF data. In the $d(^{18}\mathrm{F}, n\ \alpha)^{15}\mathrm{O}$ reaction, the CN formation: $d + {}^{18}\mathrm{F} \rightarrow {}^{20}\mathrm{Ne}^*$ can be followed by these two-step sequential emissions:
$$\begin{cases} {}^{20}\mathrm{Ne}^* \rightarrow \mathrm{n} + {}^{19}\mathrm{Ne}^* \rightarrow \mathrm{n} + \alpha + {}^{15}\mathrm{O} \\ {}^{20}\mathrm{Ne}^* \rightarrow \alpha + {}^{16}\mathrm{O}^* \rightarrow \mathrm{n} + \alpha + {}^{15}\mathrm{O} \\ {}^{20}\mathrm{Ne}^* \rightarrow {}^{15}\mathrm{O} + {}^{5}\mathrm{He}^* \rightarrow \mathrm{n} + \alpha + {}^{15}\mathrm{O} \end{cases}$$
producing the same particles as in the QF mechanism.
The second and third exit channels can be distinguished by examining the 2D relative energy matrix: n–^{15}O versus $n-\alpha$. For the not-measured neutron, energies and angles can be deduced from the reaction kinematics and conservation laws. This relative energy matrix will produce the excitation energy spectra of the compound nuclei, ^{16}O* and ^{5}He*, if this reaction mechanism is indeed present. This matrix can be used to cut any contributions from these channels. For example, Fig. 42 shows the matrix of the ^{2}H(^{18}O, α^{15}N)n TH reaction. The $\mathrm{E}_{\alpha-^{15}\mathrm{N}}$ relative energies is plotted versus $\mathrm{E}_{\alpha-n}$. Several horizontal lines can be observed. These lines correspond to different resonances populated in ^{19}F*, as expected. In contrast, no vertical line is observed. So, in this example there is no visible contribution from the ^{5}He compound nucleus.
- The occurrence of CN in the α+^{15}O channel cannot be ruled out by studying the relative energy correlation matrix because the same excited states of ^{19}Ne are formed through QF and CN. In the previous example, the problem is now to distinguish between the two reaction channels
$$\begin{cases} d + {}^{18}\mathrm{F} \rightarrow \mathrm{n} + {}^{19}\mathrm{Ne}^* \rightarrow \mathrm{n} + \alpha + {}^{15}\mathrm{O} \\ d + {}^{18}\mathrm{F} \rightarrow {}^{20}\mathrm{Ne}^* \rightarrow \mathrm{n} + {}^{19}\mathrm{Ne}^* \rightarrow \mathrm{n} + \alpha + {}^{15}\mathrm{O} \end{cases}$$
and possibly, contributions from other reaction channels, like multi-step transfer reactions.
A way to select the QF reactions is through the study of the reaction yield as a function of the spectator particle momentum p_{pn} after reaction ($p_{np} = p_n$ in inverse kinematics). The QF contribution is expected to be dominant only in a small part of the total phase-space. To select the QF contribution, a cut is used to select data with relative momentum $p_{pn} \lesssim p_{pn}^{lim}$ (Eq. (64)), see Fig. 43 (left).
Several corrections have to be applied to the data in order to compare the experimental momentum distribution p_{pn} with the expected one. (i) Data corresponding to a slice of the $E^{c.m.}_{\alpha\ ^{15}\mathrm{O}}$ energy (the energy of a resonance for example) are selected. For these data, it can be assumed that the HOES differential cross section (see Eq. (63)) is constant. (ii) Monte Carlo simulations are performed to determine geometrical detection efficiencies of the experimental setup. Then, data are normalized by the phase-space to remove pure kinematics effects, and are also corrected for detection thresholds. (iii) Data are corrected by the modulation given by the angular distribution.
These corrections produced the momentum distribution shown on Fig. 43 (right). The fact that the shape of the measured momentum distribution follows the shape of the neutron momentum distribution inside the deuteron is a good evidence for the occurrence of the QF mechanism, and that it is dominant.

3. *Determination of the two-body reaction cross section*
The events of the three-body reaction corresponding to QF mechanism have been selected according to the steps described in the previous paragraphs. The objective of the third step is to reconstruct the two-body reaction cross section. It follows that: (i) the p +^{18}F relative kinetic energy $E^{c.m.}_{p\ ^{18}\mathrm{F}}$ can be deduced from the measured $E^{c.m.}_{\alpha\ ^{15}\mathrm{O}}$ using the energy conservation law. (ii) Angular distributions of the outgoing particles α+^{15}O can be extracted for different center-of-mass energy $E^{c.m.}_{p\ ^{18}\mathrm{F}}$.
They have to be normalized by a Monte Carlo simulation of the experimental setup. (iii) For each energy step, a fit of the angular distributions can be made using a polynomial of Legendre functions. These distributions can be used to evaluate the spin and parity of the observed resonances, see Fig. 44 for some examples. (iv) The experimental two-body cross section $(\frac{d\sigma}{d\Omega})^{\mathrm{HOES}}$ is derived according to Eq. (63). (v) Usually, a smooth background is subtracted to take into account possible four-body contribution. (vi) The two-body HOES differential cross section is integrated in the whole angular range to obtain the astrophysical reaction cross section, see Eq. (66). It is assumed that in the region where no experimental angular distribution is available, their trend is given by the fit function. Finally, the astrophysical cross section is normalized at higher energy with some direct measurement data.

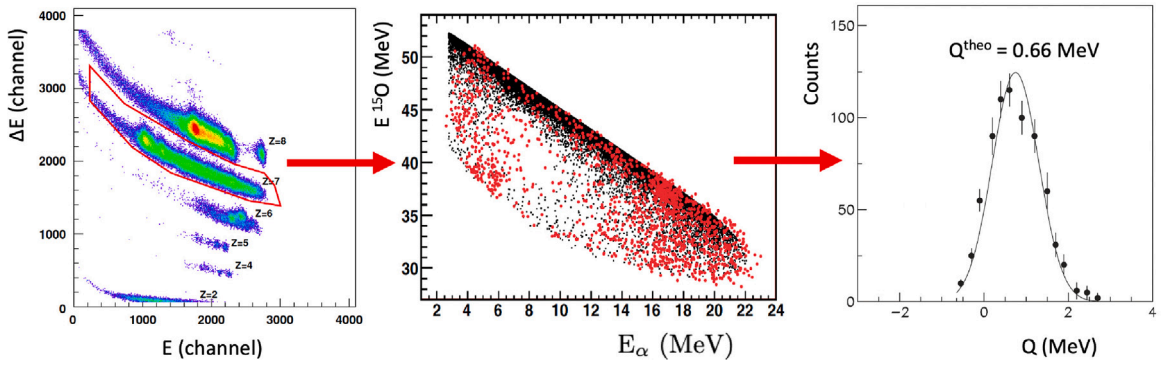

Fig. 41. The first steps of the THM data analysis is illustrated here. (Left) In the case of the ^{2}H(^{18}O, α^{15}N)n Trojan Horse reaction, a cut was made on the ΔE-E plot to select the heavy residues identified in charge Z (here ^{15}N, Z = 7), and sometimes in mass A, when the resolution is good enough, from Ref. [187]. (Center) Energy of heavy residue is shown versus energy of the particles detected in coincidence, here in the case of the ^{2}H(^{18}F, α^{15}O)n reaction, from Ref. [178]. Black points are experimental data, red ones are from a Monte Carlo simulation. It seems to be no contamination from other reactions. (Right) The measured Q value of the selected ^{2}H(^{18}F, α^{15}O)n events. If needed, a cut is made on the Q value to select the ^{15}O ground state. In the present case, there is only one peak.

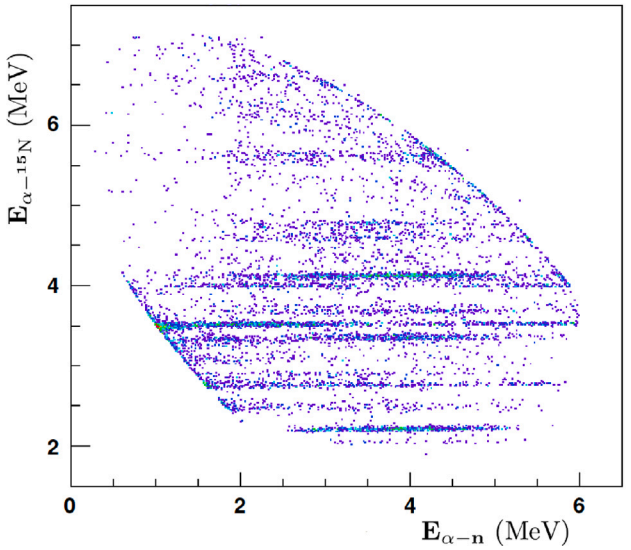

Fig. 42. In the measurement of the d(^{18}O, α^{15}N)n TH reaction, the relative energies $E_{\alpha-^{15}N}$ is plotted versus $E_{\alpha-n}$. Several horizontal lines can be observed, these correspond to different resonances populated in the $^{19}F^{*} = \alpha + ^{15}N$ compound nucleus. In contrast, no vertical line is observed. So, there is no contribution from the $^{20}F^{*} \rightarrow {}^{15}N + {}^{5}He^{*} \rightarrow n + \alpha + {}^{15}N$ compound-nucleus channel.
Source: From Ref. [187].

The results obtained for the ^{18}F(p, α)^{19}Ne reaction are presented in Fig. 45. The astrophysical S factor obtained in a THM experiment [30] (green points) is compared with results obtained in direct measurement [38] (blue points). It shows that the TH experiment has made it possible to determine the astrophysical S factor at low energies [188], where it is very difficult to measure directly. As can be seen, however, energy resolution is relatively limited.

8.8. Limitations

The Trojan Horse Method has some specific limitations [189]. (i) Radiative captures, such as (p, γ) reactions, cannot be studied with this method since in that case the recoiling nucleus is confused with the beam. (ii) Energy resolution is often limited, at best ≈50 keV in c.m. (iii) The background subtraction is quite arbitrary. (iv) Reservations have been expressed about the reliability of THM due to cross-section modifications caused by off-shell effects and final-state interactions.

9. Beta-delayed particle emission

Among the experimental techniques used in nuclear astrophysics, radioactive decay is sometimes used to study the properties of the populated states in the daughter nucleus. This method is very interesting in nuclear astrophysics when the states populated by

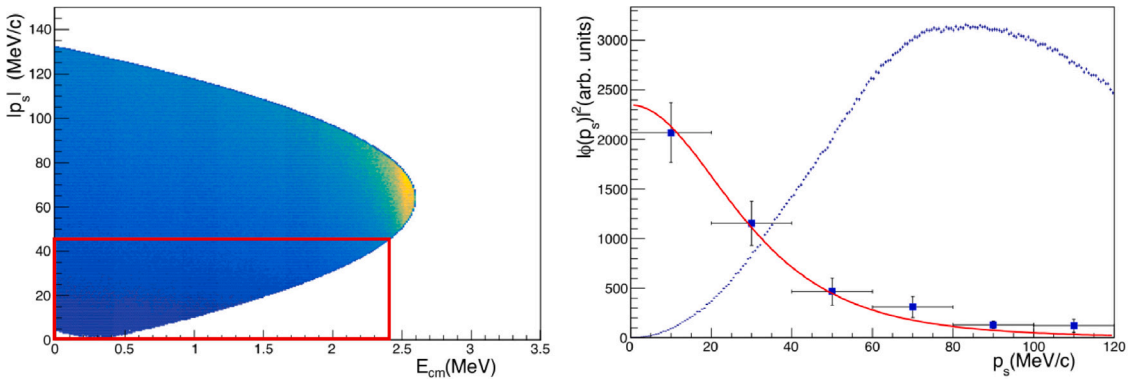

Fig. 43. Left: Monte Carlo simulation of the $d(^{18}\mathrm{F}, \alpha^{15}\mathrm{O})n$ reaction at E^{lab} = 47.9 MeV, showing the phase-space available for the momentum of the spectator particle $|p_s|$ (neutron) versus the center-of-mass energy $E_{c.m.}$ of the system α + ^{15}O. The part of the phase space where the quasi-free mechanism is expected to dominate (red box, $|p_s| \lesssim 45$ MeV/c) represents only a part of the total available space phase. Right: Measured spectator particle momentum p_s (solid dots from Ref. [30]) compared to the Monte Carlo phase space (dotted line). The shape of the measured momentum distribution follows the shape of the internal motion of the neutron in the deuterium nucleus (the red line). This proves the predominance of the quasi-free reaction mechanism in the phase space selected in the data.

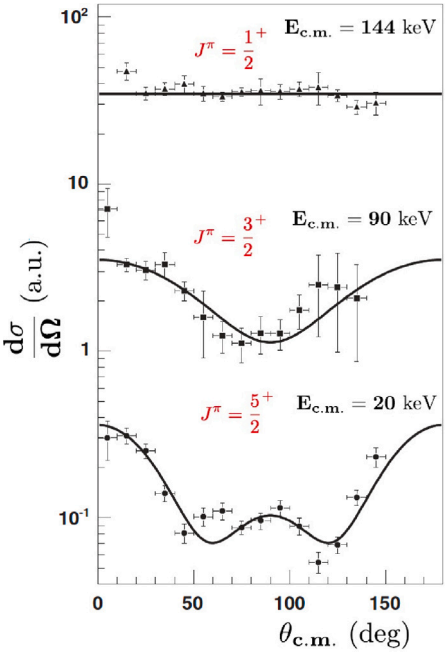

Fig. 44. Experimental angular distributions obtained in the $^{18}\mathrm{O}(d, \alpha n)^{15}\mathrm{N}$ Trojan Horse reaction [177]. Differential cross sections are shown as a function of c.m. angle between α and ^{15}N, after selecting the events within certain energy ranges corresponding to three resonances in ^{18}O+p. The full lines come from the fitting of the distributions. The best fit for the 90 keV resonance is achieved with $L = 1$ ($\chi^2 = 0.67$), meaning a spin $\frac{3}{2}$ for the 8.084 MeV excited state of ^{19}F. The $J^\pi = \frac{1}{2}^+$ assignment for the 144 keV resonance was confirmed, the angular distribution for that level being isotropic.

beta decay are also the states possibly populated by proton or α capture reaction. The astrophysical $^{18}\mathrm{F}(p, \alpha)^{15}\mathrm{O}$ reaction has never been studied using this method. The most favorable ($L = 0$) transferred angular momentum for this reaction $^{18}\mathrm{F}(1^+) + p(1/2^+)$ corresponds to $1/2^+$ and $3/2^+$ spin states in ^{19}Ne. The ^{19}Ne states can also be populated by the radioactive decay of the parent nucleus ^{19}Na, see Fig. 46. The rules in the Gamow–Teller β-decay select states with spin $J \pm 1$ relatively to the spin of the parent nucleus. In the case of ^{19}Na, the spin of the ground state being $J = 5/2^+$, beta decay leads to the preferential population of the $3/2^+$, $5/2^+$ and $7/2^+$ spin states of ^{19}Ne. It would have been interesting to study the $3/2^+$ states of ^{19}Ne populated by the β^+ decay of ^{19}Na, since these resonances are of high interest in astrophysics, but the ^{19}Na parent nucleus is not bound for proton emission [98], so the study is not feasible. Fig. 47 gives an overview of many feasible cases of potential interest for nuclear astrophysics. To take another interesting example, the $^{30}\mathrm{P}_{1+}(p_{1/2^+}, \gamma)^{31}\mathrm{S}$ reaction is important in astrophysics [190,191]. This reaction occurs mainly through ($L = 0$) resonances in ^{31}S, with $3/2^+$ and $1/2^+$ spin. These states can be populated by the β^+ decay of ^{31}Cl, which explains

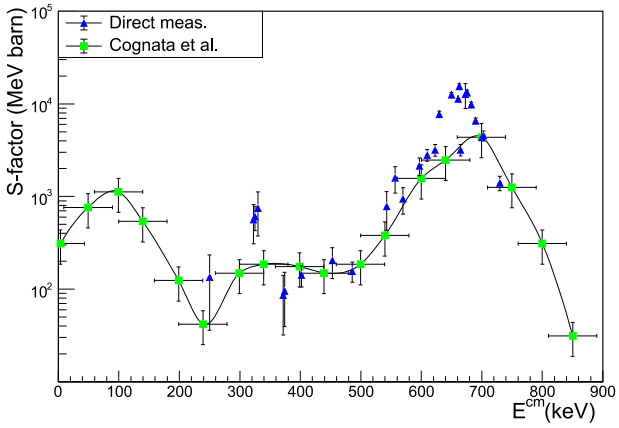

Fig. 45. Astrophysical S factor of the ^{18}F(p, α)^{19}Ne reaction. The astrophysical S factor obtained in a THM experiment [30,188] (green points) is compared with results obtained in direct measurements (blue points). The line is a guide for the eyes. The TH measurement makes it possible to determine the astrophysical S factor at low energies, where direct measurements are almost impossible.

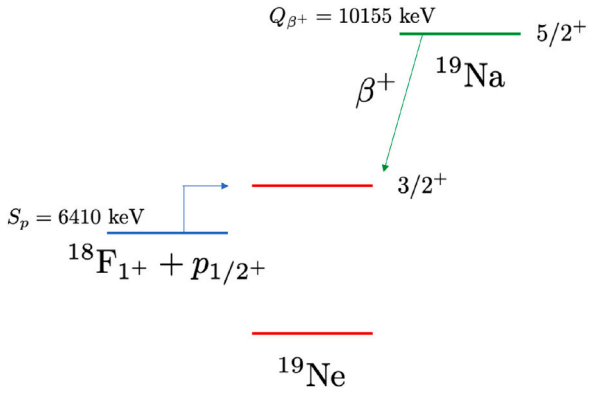

Fig. 46. The ^{18}F(p, α)^{15}O astrophysical reaction occurs through resonances in ^{19}Ne. The lowest transferred angular momenta ($L = 0$) are generally the most favorable, due to the centrifugal barrier, so the $3/2^+$ and $1/2^+$ spin states in ^{19}Ne are the most important. The radioactive decay of ^{19}Na leads to the preferential population of $3/2^+$, $5/2^+$ and $7/2^+$ spin states (Gamow–Teller decay). It would therefore be possible to study the $3/2^+$ states via radioactive decay. However, ^{19}Na is unbound, so this study is not feasible.

why the ^{30}P box is shown in red color in Fig. 47. Excited states important in astrophysics can be populated directly by β decay, as discussed above, e.g. ^{19}Na(β^+)^{19}Ne* if ^{19}Na was bound. Excited states can also be populated indirectly by β-delayed particle emission, e.g. ^{20}Mg(β^+)^{20}Na(p)^{19}Ne*. This latter decay has indeed been used to study the excited states of ^{19}Ne, but it did not allow to populate the important states for the ^{18}F(p, α)^{15}O reaction, since only low energy states (E_x < 4.1 MeV) were observed in this study [192]. Fig. 47 also confirms that the ^{18}F(p, α)^{15}O reaction cannot be studied by beta-delayed proton emission, but only by beta-delayed two-proton emission, with the purple ^{18}F box. Other more complex β-delayed emission, such as three-protons emission, can also be used in nuclear astrophysics. There are many potentially interesting solutions, but they need to be studied on a case-by-case basis.

The main problem with β-decay measurement is that the β-delayed particles are emitted at low energy, sometimes at the limit of detection. Moreover, the measured signal is often very polluted by β radiations. There are many ways of measuring β decay. Without going into details, two types of measurement can be carried out: either the radioactive nuclei are implanted in a solid material, a silicon detector for example, and the charged particles emitted by the β decay are measured with a good-resolution detector, or the radioactive nuclei are implanted in an active target detector, e.g. AstroBox2 [191], which is used to slow down and stop the nuclei, and also to measure the emitted particles. Using a gaseous detector improves the signal-to-noise ratio, since it is less sensitive to beta radiations.

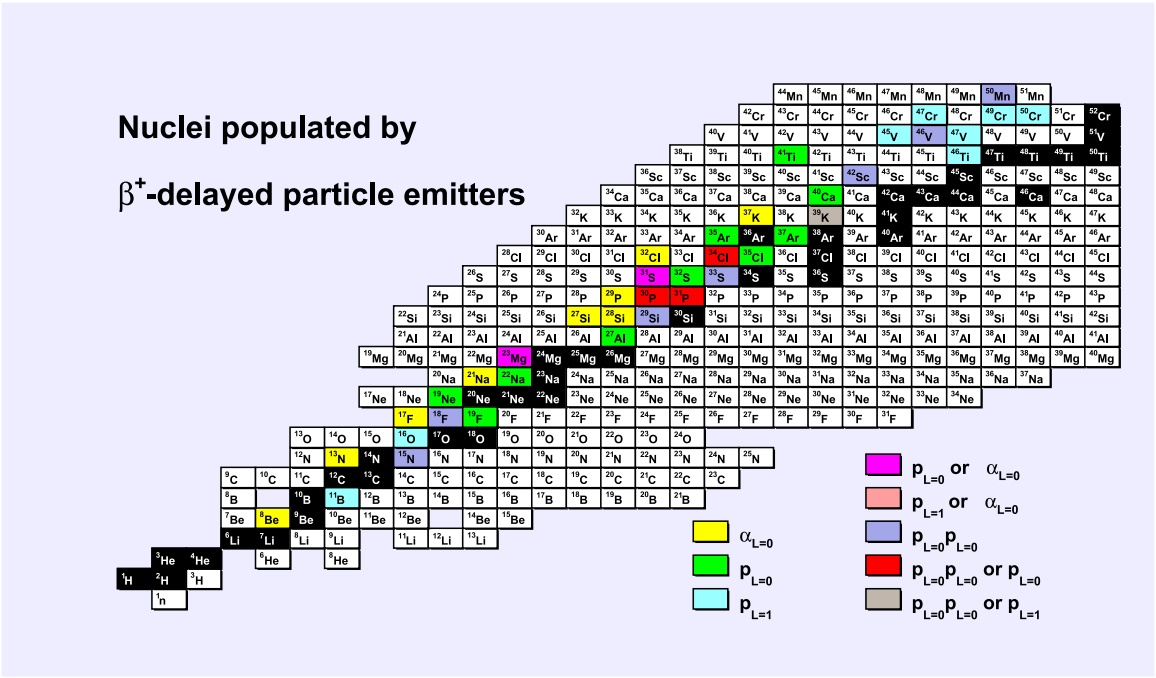

Fig. 47. Set of nuclei that can be studied in an astrophysical context by measuring the β^+-delayed particle emission. For example, ^{45}V is in light blue in this chart, meaning that the $^{45}V(p,\gamma)^{46}Cr$ reaction could be studied via the measurement of the $^{46}Mg(\beta^+)^{46}Cr(p)^{45}V$ decay. Note that the $^{18}F(p,\alpha)^{15}O$ reaction can be studied by measuring the $^{20}Mg(\beta^+)^{20}Na(p)^{19}Ne(p)^{18}F$ decay.

10. Conclusion

Several experimental techniques have been used to study the astrophysical $^{18}F(p,\alpha)^{15}O$ reaction for over two decades. Some aspects remain unknown and are still being discussed, leading to uncertainties in the rate of this reaction of up to a factor of 3 under the thermodynamic conditions of novae [23]. Fig. 48 shows the evolution of the reaction rate for two temperatures as a function of years. Note that the value has not changed much since the 2000s. Note also that the uncertainty on the rate, when estimated, has not changed much. There are two main reasons for this: on the one hand, some states still do not have a firm spin assignment. In particular, a doublet of $3/2^+$ ($\ell_p = 0$) states has been predicted in the Gamow window. Measurements at very high energy resolution have revealed three states in the first 50 keV above the proton threshold, none of which are $3/2^+$ states according to their angular distribution. The reaction rate depends very much on the position of these $3/2^+$ states. On the other hand, the signs of interference between the $3/2^+$ resonances are still not known.

These two aspects could be solved in the near future, using the same methods under improved experimental conditions. It will certainly be necessary to propose an indirect measurement, with excellent energy resolution to distinguish states close to threshold and determine their spin. It will also be necessary to re-measure the reaction directly at relatively low energies with high accuracy, to constrain the signs of resonance interference. Furthermore, new experimental techniques may be proposed in the future to unlock the secrets of this reaction.

Declaration of competing interest

The authors declare that they have no known competing financial interests or personal relationships that could have appeared to influence the work reported in this paper.

Acknowledgments

I am very grateful to Laurie Dienis, Ignasio Wakudyanaye, and especially Dr. Chloé Fougères, for their help with the careful reading and for their suggestions for improving the quality of the article.

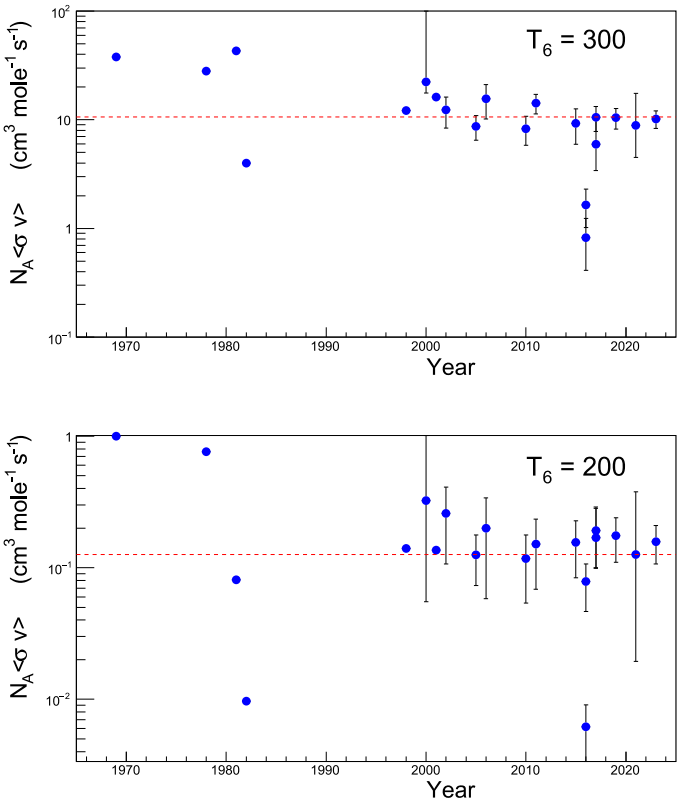

Fig. 48. Evolution of the ^{18}F(p, α)^{15}O reaction rate over the years for two different temperatures, 300 and 200 GK. In both cases, the value has not changed significantly since the early 2000s, nor has the associated uncertainty, despite considerable efforts. This is because some states in ^{19}Ne do not have a definitive spin assignment, and also because some resonances interfere with signs that are not yet known. The red dashed line is a guide for the eyes.
Source: From Ref. [9,13–15,27,31,38,39,41,70,128,146,147,178,193,194].

References

[1] J. Perrin, Annales de Physique, vol. 9, 1919, pp. 5–108.
[2] E. Rutherford, Phil. Mag. 90 (S1) (2010) 31–37.
[3] F.W. Aston, Lond. Edinb. Dublin Philos. Mag. J. Sci. 39 (233) (1920) 611–625.
[4] B.A. for the Advancement of Science. Meeting, Report of the British Association for the Advancement of Science: 1920, J. Murray, Albemarle Street, 1920, pp. 34–49.
[5] B. Abbott, R. Abbott, R. Adhikari, A. Ananyeva, S. Anderson, S. Appert, K. Arai, M. Araya, J. Barayoga, B. Barish, et al., Astrophys. J. Lett. 848 (2) (2017) L12.
[6] R.A. Alpher, H. Bethe, G. Gamow, Phys. Rev. 73 (7) (1948) 803.
[7] J. José, M. Hernanz, C. Iliadis, Nucl. Phys. A 777 (2006) 550–578, http://dx.doi.org/10.1016/j.nuclphysa.2005.02.121, URL https://www.sciencedirect.com/science/article/pii/S0375947405002708. Special Isseu on Nuclear Astrophysics.
[8] J. José, S.N. Shore, Cambridge Astrophys. Ser. 43 (2008) 121.
[9] A. Coc, M. Hernanz, J. José, J.-P. Thibaud, Astron. Astrophys. 357 (2000) 561–571.
[10] J. Gómez-Gomar, M. Hernanz, J. José, J. Isern, Mon. Not. R. Astron. Soc. 296 (4) (1998) 913–920, http://dx.doi.org/10.1046/j.1365-8711.1998.01421.x, arXiv:https://academic.oup.com/mnras/article-pdf/296/4/913/18408441/296-4-913.pdf.
[11] R. Diehl, Rep. Progr. Phys. 76 (2) (2013) 026301, http://dx.doi.org/10.1088/0034-4885/76/2/026301.
[12] O. König, J. Wilms, R. Arcodia, T. Dauser, K. Dennerl, V. Doroshenko, F. Haberl, S. Hämmerich, C. Kirsch, I. Kreykenbohm, M. Lorenz, A. Malyali, A. Merloni, A. Rau, T. Rauch, G. Sala, A. Schwope, V. Suleimanov, P. Weber, K. Werner, Nature 605 (7909) (2022) 248–250, http://dx.doi.org/10.1038/s41586-022-04635-y.
[13] M. Wiescher, K.-U. Kettner, Astrophys. J. 263 (1982) 891.
[14] S. Utku, J.G. Ross, N.P.T. Bateman, D.W. Bardayan, A.A. Chen, J. Görres, A.J. Howard, C. Iliadis, P.D. Parker, M.S. Smith, R.B. Vogelaar, M. Wiescher, K. Yildiz, Phys. Rev. C 57 (1998) 2731–2739, http://dx.doi.org/10.1103/PhysRevC.57.2731, URL https://link.aps.org/doi/10.1103/PhysRevC.57.2731.
[15] D. Kahl, J. José, P.J. Woods, Astron. Astrophys. 653 (2021) A64.
[16] C.E. Rolfs, W.S. Rodney, Cauldrons in the Cosmos: Nuclear Astrophysics, University of Chicago Press, 1988.
[17] C. Iliadis, Nuclear Physics of Stars, John Wiley and Sons, 2007.
[18] C.A. Bertulani, Nuclei in the Cosmos, World Scientific, 2014.
[19] R.H. Cyburt, A.M. Amthor, R. Ferguson, Z. Meisel, K. Smith, S. Warren, A. Heger, R.D. Hoffman, T. Rauscher, A. Sakharuk, H. Schatz, F.K. Thielemann, M. Wiescher, Astrophys. J. Suppl. Ser. 189 (1) (2010) 240, http://dx.doi.org/10.1088/0067-0049/189/1/240.
[20] G.R. Caughlan, W.A. Fowler, At. Data Nucl. Data Tables 40 (2) (1988) 283–334.

[21] D. Lattuada, M. Barbarino, A. Bonasera, W. Bang, H.J. Quevedo, M. Warren, F. Consoli, R. De Angelis, P. Andreoli, S. Kimura, G. Dyer, A.C. Bernstein, K. Hagel, M. Barbui, K. Schmidt, E. Gaul, M.E. Donovan, J.B. Natowitz, T. Ditmire, Phys. Rev. C 93 (2016) 045808, http://dx.doi.org/10.1103/PhysRevC.93.045808, URL https://link.aps.org/doi/10.1103/PhysRevC.93.045808.

[22] M. Barbui, W. Bang, A. Bonasera, K. Hagel, K. Schmidt, J.B. Natowitz, R. Burch, G. Giuliani, M. Barbarino, H. Zheng, G. Dyer, H.J. Quevedo, E. Gaul, A.C. Bernstein, M. Donovan, S. Kimura, M. Mazzocco, F. Consoli, R. De Angelis, P. Andreoli, T. Ditmire, Phys. Rev. Lett. 111 (2013) 082502, http://dx.doi.org/10.1103/PhysRevLett.111.082502, URL https://link.aps.org/doi/10.1103/PhysRevLett.111.082502.

[23] R. Longland, C. Iliadis, A. Champagne, J. Newton, C. Ugalde, A. Coc, R. Fitzgerald, Nucl. Phys. A 841 (1) (2010) 1–30, http://dx.doi.org/10.1016/j.nuclphysa.2010.04.008, URL https://www.sciencedirect.com/science/article/pii/S0375947410004185. The 2010 Evaluation of Monte Carlo based Thermonuclear Reaction Rates.

[24] Perspectives of nuclear physics in Europe, 2017, http://www.nupecc.org/.

[25] G. Kiss, M. La Cognata, C. Spitaleri, R. Yarmukhamedov, I. Wiedenhöver, L. Baby, S. Cherubini, A. Cvetinović, G. D'Agata, P. Figuera, G. Guardo, M. Gulino, S. Hayakawa, I. Indelicato, L. Lamia, M. Lattuada, F. Mudò, S. Palmerini, R. Pizzone, G. Rapisarda, S. Romano, M. Sergi, R. Spartà, O. Trippella, A. Tumino, M. Anastasiou, S. Kuvin, N. Rijal, B. Schmidt, S. Igamov, S. Sakuta, K. Tursunmakhatov, Z. Fülöp, G. Gyürky, T. Szücs, Z. Halász, E. Somorjai, Z. Hons, J. Mrázek, R. Tribble, A. Mukhamedzhanov, Phys. Lett. B 807 (2020) 135606, http://dx.doi.org/10.1016/j.physletb.2020.135606, URL https://www.sciencedirect.com/science/article/pii/S0370269320304093.

[26] D. Kahl, P.J. Woods, Y. Fujita, H. Fujita, K. Abe, T. Adachi, D. Frekers, T. Ito, N. Kikukawa, M. Nagashima, P. Puppe, D. Sera, T. Shima, Y. Shimbara, A. Tamii, J.H. Thies, Eur. Phys. J. A 55 (1) (2019) 4, http://dx.doi.org/10.1140/epja/i2019-12682-9.

[27] M.R. Hall, D.W. Bardayan, T. Baugher, A. Lepailleur, S.D. Pain, A. Ratkiewicz, S. Ahn, J.M. Allen, J.T. Anderson, A.D. Ayangeakaa, J.C. Blackmon, S. Burcher, M.P. Carpenter, S.M. Cha, K.Y. Chae, K.A. Chipps, J.A. Cizewski, M. Febbraro, O. Hall, J. Hu, C.L. Jiang, K.L. Jones, E.J. Lee, P.D. O'Malley, S. Ota, B.C. Rasco, D. Santiago-Gonzalez, D. Seweryniak, H. Sims, K. Smith, W.P. Tan, P. Thompson, C. Thornsberry, R.L. Varner, D. Walter, G.L. Wilson, S. Zhu, Phys. Rev. Lett. 122 (2019) 052701, http://dx.doi.org/10.1103/PhysRevLett.122.052701, URL https://link.aps.org/doi/10.1103/PhysRevLett.122.052701.

[28] D. Torresi, C. Wheldon, T. Kokalova, S. Bailey, A. Boiano, C. Boiano, M. Fisichella, M. Mazzocco, C. Parascandolo, D. Pierroutsakou, E. Strano, M. Zadro, M. Cavallaro, S. Cherubini, N. Curtis, A. Di Pietro, J.P. Fernández Garcia, P. Figuera, T. Glodariu, J. Gręboszc, M. La Cognata, M. La Commara, M. Lattuada, D. Mengoni, R.G. Pizzone, C. Signorini, C. Stefanini, L. Stroe, C. Spitaleri, Phys. Rev. C 96 (2017) 044317, http://dx.doi.org/10.1103/PhysRevC.96.044317, URL https://link.aps.org/doi/10.1103/PhysRevC.96.044317.

[29] A. Parikh, A.M. Laird, N. de Séréville, K. Wimmer, T. Faestermann, R. Hertenberger, D. Seiler, H.-F. Wirth, P. Adsley, B.R. Fulton, F. Hammache, J. Kiener, I. Stefan, Phys. Rev. C 92 (2015) 055806, http://dx.doi.org/10.1103/PhysRevC.92.055806, URL https://link.aps.org/doi/10.1103/PhysRevC.92.055806.

[30] S. Cherubini, M. Gulino, C. Spitaleri, G.G. Rapisarda, M. La Cognata, L. Lamia, R.G. Pizzone, S. Romano, S. Kubono, H. Yamaguchi, S. Hayakawa, Y. Wakabayashi, N. Iwasa, S. Kato, T. Komatsubara, T. Teranishi, A. Coc, N. de Séréville, F. Hammache, G. Kiss, S. Bishop, D.N. Binh, Phys. Rev. C 92 (2015) 015805, http://dx.doi.org/10.1103/PhysRevC.92.015805, URL https://link.aps.org/doi/10.1103/PhysRevC.92.015805.

[31] A.S. Adekola, D.W. Bardayan, J.C. Blackmon, C.R. Brune, K.Y. Chae, C. Domizioli, U. Greife, Z. Heinen, M.J. Hornish, K.L. Jones, R.L. Kozub, R.J. Livesay, Z. Ma, T.N. Massey, B. Moazen, C.D. Nesaraja, S.D. Pain, J.F. Shriner, N.D. Smith, M.S. Smith, J.S. Thomas, D.W. Visser, A.V. Voinov, Phys. Rev. C 83 (2011) 052801, http://dx.doi.org/10.1103/PhysRevC.83.052801, URL https://link.aps.org/doi/10.1103/PhysRevC.83.052801.

[32] J. José, Stellar Explosions: Hydrodynamics and Nucleosynthesis, vol. 10, 2016.

[33] T. Rauscher, Phys. Rev. C 81 (2010) 045807, http://dx.doi.org/10.1103/PhysRevC.81.045807, URL https://link.aps.org/doi/10.1103/PhysRevC.81.045807.

[34] R. Coszach, M. Cogneau, C. Bain, F. Binon, T. Davinson, P. Decrock, T. Delbar, M. Gaelens, W. Galster, J. Goerres, J. Graulich, R. Irvine, D. Labar, P. Leleux, M. Loiselet, C. Michotte, R. Neal, G. Ryckewaert, A. Shotter, J. Vanhorenbeeck, J. Vervier, M. Wiescher, P. Woods, Phys. Lett. B 353 (2) (1995) 184–188, http://dx.doi.org/10.1016/0370-2693(95)00550-5, URL https://www.sciencedirect.com/science/article/pii/0370269395005505.

[35] N. De Séréville, C. Angulo, A. Coc, N.L. Achouri, E. Casarejos, T. Davinson, P. Descouvemont, P. Figuera, S. Fox, F. Hammache, J. Kiener, A. Laird, A. Lefebvre-Schuhl, P. Leleux, P. Mumby-Croft, N.A. Orr, I. Stefan, K. Vaughan, V. Tatischeff, Phys. Rev. C 79 (2009) 015801, http://dx.doi.org/10.1103/PhysRevC.79.015801, URL https://link.aps.org/doi/10.1103/PhysRevC.79.015801.

[36] K.E. Rehm, M. Paul, A.D. Roberts, D.J. Blumenthal, J. Gehring, D. Henderson, C.L. Jiang, J. Nickles, J. Nolen, R.C. Pardo, J.P. Schiffer, R.E. Segel, Phys. Rev. C 52 (1995) R460–R463, http://dx.doi.org/10.1103/PhysRevC.52.R460, URL https://link.aps.org/doi/10.1103/PhysRevC.52.R460.

[37] K.E. Rehm, M. Paul, A.D. Roberts, C.L. Jiang, D.J. Blumenthal, S.M. Fischer, J. Gehring, D. Henderson, J. Nickles, J. Nolen, R.C. Pardo, J.P. Schiffer, R.E. Segel, Phys. Rev. C 53 (1996) 1950–1954, http://dx.doi.org/10.1103/PhysRevC.53.1950, URL https://link.aps.org/doi/10.1103/PhysRevC.53.1950.

[38] D.W. Bardayan, J.C. Blackmon, W. Bradfield-Smith, C.R. Brune, A.E. Champagne, T. Davinson, B.A. Johnson, R.L. Kozub, C.S. Lee, R. Lewis, P.D. Parker, A.C. Shotter, M.S. Smith, D.W. Visser, P.J. Woods, Phys. Rev. C 63 (2001) 065802, http://dx.doi.org/10.1103/PhysRevC.63.065802, URL https://link.aps.org/doi/10.1103/PhysRevC.63.065802.

[39] K.Y. Chae, D.W. Bardayan, J.C. Blackmon, D. Gregory, M.W. Guidry, M.S. Johnson, R.L. Kozub, R.J. Livesay, Z. Ma, C.D. Nesaraja, S.D. Pain, S. Paulauskas, M. Porter-Peden, J.F.S. Jr., N. Smith, M.S. Smith, J.S. Thomas, Phys. Rev. C 74 (2006) 012801, http://dx.doi.org/10.1103/PhysRevC.74.012801, URL https://link.aps.org/doi/10.1103/PhysRevC.74.012801.

[40] D. Bardayan, J. Batchelder, J. Blackmon, A. Champagne, T. Davison, R. Fitzgerald, W. Hix, C. Iliadis, R. Kozub, Z. Ma, S. Parete-Koon, P. Parker, N. Shu, M. Smith, P. Woods, Nucl. Phys. A 718 (2003) 590–592, http://dx.doi.org/10.1016/S0375-9474(03)00873-X, URL https://www.sciencedirect.com/science/article/pii/S037594740300873X.

[41] D.W. Bardayan, J.C. Batchelder, J.C. Blackmon, A.E. Champagne, T. Davinson, R. Fitzgerald, W.R. Hix, C. Iliadis, R.L. Kozub, Z. Ma, S. Parete-Koon, P.D. Parker, N. Shu, M.S. Smith, P.J. Woods, Phys. Rev. Lett. 89 (2002) 262501, http://dx.doi.org/10.1103/PhysRevLett.89.262501, URL https://link.aps.org/doi/10.1103/PhysRevLett.89.262501.

[42] C.E. Beer, A.M. Laird, A.S.J. Murphy, M.A. Bentley, L. Buchman, B. Davids, T. Davinson, C.A. Diget, S.P. Fox, B.R. Fulton, U. Hager, D. Howell, L. Martin, C. Ruiz, G. Ruprecht, P. Salter, C. Vockenhuber, P. Walden, Phys. Rev. C 83 (2011) 042801, http://dx.doi.org/10.1103/PhysRevC.83.042801, URL https://link.aps.org/doi/10.1103/PhysRevC.83.042801.

[43] C. Beer, A. Laird, S. Fox, B. Fulton, M. Bentley, C. Diget, A. Murphy, T. Davinson, P. Salter, C. Ruiz, L. Buchmann, H. Dare, B. Davids, U. Hager, D. Howell, L. Martin, G. Ruprecht, P. Walden, C. Vockhenhuber, 2012, pp. 1–5, 10th Symposium on Nuclei in the Cosmos ; Conference date: 27-07-2008 Through 01-08-2008.

[44] D.J. Mountford, A.S.J. Murphy, N.L. Achouri, C. Angulo, J.R. Brown, T. Davinson, F. de Oliveira Santos, N. de Séréville, P. Descouvemont, O. Kamalou, A.M. Laird, S.T. Pittman, P. Ujic, P.J. Woods, Phys. Rev. C 85 (2012) 022801, http://dx.doi.org/10.1103/PhysRevC.85.022801, URL https://link.aps.org/doi/10.1103/PhysRevC.85.022801.

[45] L. Gialanella, D. Schürmann, F. Strieder, A. Di Leva, N. De Cesare, A. D'Onofrio, G. Imbriani, J. Klug, C. Lubritto, A. Ordine, V. Roca, H. Röcken, C. Rolfs, D. Rogalla, M. Romano, F. Schümann, F. Terrasi, H. Trautvetter, Nucl. Instrum. Methods Phys. Res. A 522 (3) (2004) 432–438, http://dx.doi.org/10.1016/j.nima.2003.11.386, URL http://www.sciencedirect.com/science/article/pii/S0168900203031541.

[46] Z. Meisel, M. Moran, G. Gilardy, J. Schmitt, C. Seymour, M. Couder, Nucl. Instrum. Methods Phys. Res. A 850 (2017) 48–53, http://dx.doi.org/10.1016/j.nima.2017.01.035, URL http://www.sciencedirect.com/science/article/pii/S0168900217300359.

[47] G. Berg, M. Couder, M. Moran, K. Smith, M. Wiescher, H. Schatz, U. Hager, C. Wrede, F. Montes, G. Perdikakis, X. Wu, A. Zeller, M. Smith, D. Bardayan, K. Chipps, S. Pain, J. Blackmon, U. Greife, K. Rehm, R. Janssens, Nucl. Instrum. Methods Phys. Res. A 877 (2018) 87–103, http://dx.doi.org/10.1016/j.nima.2017.08.048, URL http://www.sciencedirect.com/science/article/pii/S0168900217309488.

[48] C. Vockenhuber, L. Buchmann, J. Caggiano, A. Chen, J. D'Auria, C. Davis, U. Greife, A. Hussein, D. Hutcheon, D. Ottewell, C. Ouellet, A. Parikh, J. Pearson, C. Ruiz, G. Ruprecht, M. Trinczek, J. Zylberberg, Nucl. Instrum. Methods Phys. Res. B 266 (19) (2008) 4167–4170, http://dx.doi.org/10.1016/j.nimb.2008.05.146, URL http://www.sciencedirect.com/science/article/pii/S0168583X08006988. Proceedings of the XVth International Conference on Electromagnetic Isotope Separators and Techniques Related to their Applications.

[49] C. Broggini, D. Bemmerer, A. Guglielmetti, R. Menegazzo, Annu. Rev. Nucl. Part. Sci. 60 (1) (2010) 53–73, http://dx.doi.org/10.1146/annurev.nucl.012809.104526, arXiv:https://doi.org/10.1146/annurev.nucl.012809.104526.

[50] C. Broggini, D. Bemmerer, A. Caciolli, D. Trezzi, Prog. Part. Nucl. Phys. 98 (2018) 55–84, http://dx.doi.org/10.1016/j.ppnp.2017.09.002, URL http://www.sciencedirect.com/science/article/pii/S0146641017300868.

[51] J. Su, H. Zhang, Z. Li, P. Ventura, Y. Li, E. Li, C. Chen, Y. Shen, G. Lian, B. Guo, X. Li, L. Zhang, J. He, Y. Sheng, Y. Chen, L. Wang, L. Zhang, F. Cao, W. Nan, W. Nan, G. Li, N. Song, B. Cui, L. Chen, R. Ma, Z. Zhang, T. Jiao, B. Gao, X. Tang, Q. Wu, J. Li, L. Sun, S. Wang, S. Yan, J. Liao, Y. Wang, S. Zeng, D. Nan, Q. Fan, N. Qi, W. Sun, X. Guo, P. Zhang, Y. Chen, Y. Zhou, J. Zhou, J. He, C. Shang, M. Li, J. Cheng, W. Liu, Sci. Bull. 67 (2) (2022) 125–132, http://dx.doi.org/10.1016/j.scib.2021.10.018, URL https://www.sciencedirect.com/science/article/pii/S2095927321006745.

[52] W. Liu, Z. Li, J. He, X. Tang, G. Lian, Z. An, J. Chang, H. Chen, Q. Chen, X. Chen, Z. Chen, B. Cui, X. Du, C. Fu, L. Gan, B. Guo, G. He, A. Heger, S. Hou, H. Huang, N. Huang, B. Jia, L. Jiang, S. Kubono, J. Li, K. Li, T. Li, Y. Li, M. Lugaro, X. Luo, H. Ma, S. Ma, D. Mei, Y. Qian, J. Qin, J. Ren, Y. Shen, J. Su, L. Sun, W. Tan, I. Tanihata, S. Wang, P. Wang, Y. Wang, Q. Wu, S. Xu, S. Yan, L. Yang, Y. Yang, X. Yu, Q. Yue, S. Zeng, H. Zhang, H. Zhang, L. Zhang, N. Zhang, Q. Zhang, T. Zhang, X. Zhang, X. Zhang, Z. Zhang, W. Zhao, Z. Zhao, C. Zhou, EPJ Web Conf. 109 (2016) 09001, http://dx.doi.org/10.1051/epjconf/201610909001.

[53] D. Robertson, M. Couder, U. Greife, F. Strieder, M. Wiescher, EPJ Web Conf. 109 (2016) 09002, http://dx.doi.org/10.1051/epjconf/201610909002.

[54] G. Gyürky, Z. Fülöp, F. Käppeler, G.G. Kiss, A. Wallner, Eur. Phys. J. A 55 (3) (2019) 41, http://dx.doi.org/10.1140/epja/i2019-12708-4.

[55] J. Powell, J. O'Neil, J. Cerny, Nucl. Instrum. Methods Phys. Res. B 204 (2003) 440–443, http://dx.doi.org/10.1016/S0168-583X(02)02110-9, URL https://www.sciencedirect.com/science/article/pii/S0168583X02021109. 14th International Conference on Electromagnetic Isotope Separators and Techniques Related to their Applications.

[56] K. Knie, T. Faestermann, G. Korschinek, Nucl. Instrum. Methods Phys. Res. B 123 (1) (1997) 128–131, http://dx.doi.org/10.1016/S0168-583X(96)00753-7, URL http://www.sciencedirect.com/science/article/pii/S0168583X96007537. Accelerator Mass Spectrometry.

[57] D. Robertson, P. Collon, D. Henderson, S. Kurtz, L. Lamm, C. Schmitt, B. Shumard, J. Webb, Nucl. Instrum. Methods Phys. Res. B 266 (15) (2008) 3481–3486, http://dx.doi.org/10.1016/j.nimb.2008.05.009, URL http://www.sciencedirect.com/science/article/pii/S0168583X08006381.

[58] A. Wallner, M. Bichler, K. Buczak, I. Dillmann, F. Käppeler, A. Karakas, C. Lederer, M. Lugaro, K. Mair, A. Mengoni, G. Schätzel, P. Steier, H.P. Trautvetter, Phys. Rev. C 93 (2016) 045803, http://dx.doi.org/10.1103/PhysRevC.93.045803, URL https://link.aps.org/doi/10.1103/PhysRevC.93.045803.

[59] M. Lestinsky, A. Brauning-Demian, H. Danared, M. Engstrom, W. Enders, S. Fedotova, B. Franzke, A. Heinz, F. Herfurth, A. Kallberg, O. Kester, Y. Litvinov, M. Steck, D. Reistad, A. Simonsson, O. Skeppstedt, T. Stöhlker, G. Vorobjev, for the CRYRING@ESR working group, Phys. Scr. 2015 (T166) (2015) 014075, http://dx.doi.org/10.1088/0031-8949/2015/T166/014075.

[60] J. Glorius, C. Langer, Z. Slavkovská, L. Bott, C. Brandau, B. Brückner, K. Blaum, X. Chen, S. Dababneh, T. Davinson, P. Erbacher, S. Fiebiger, T. Gaßner, K. Göbel, M. Groothuis, A. Gumberidze, G. Gyürky, M. Heil, R. Hess, R. Hensch, P. Hillmann, P.-M. Hillenbrand, O. Hinrichs, B. Jurado, T. Kausch, A. Khodaparast, T. Kisselbach, N. Klapper, C. Kozhuharov, D. Kurtulgil, G. Lane, C. Lederer-Woods, M. Lestinsky, S. Litvinov, Y.A. Litvinov, B. Löher, F. Nolden, N. Petridis, U. Popp, T. Rauscher, M. Reed, R. Reifarth, M.S. Sanjari, D. Savran, H. Simon, U. Spillmann, M. Steck, T. Stöhlker, J. Stumm, A. Surzhykov, T. Szücs, T.T. Nguyen, A. Taremi Zadeh, B. Thomas, S.Y. Torilov, H. Törnqvist, M. Träger, C. Trageser, S. Trotsenko, L. Varga, M. Volknandt, H. Weick, M. Weigand, C. Wolf, P.J. Woods, Y.M. Xing, Phys. Rev. Lett. 122 (2019) 092701, http://dx.doi.org/10.1103/PhysRevLett.122.092701, URL https://link.aps.org/doi/10.1103/PhysRevLett.122.092701.

[61] L.C. Biedenharn, M.E. Rose, Rev. Modern Phys. 25 (1953) 729–777, http://dx.doi.org/10.1103/RevModPhys.25.729, URL https://link.aps.org/doi/10.1103/RevModPhys.25.729.

[62] H. Lorenz-Wirzba, P. Schmalbrock, H. Trautvetter, M. Wiescher, C. Rolfs, W. Rodney, Nucl. Phys. A 313 (3) (1979) 346–362.

[63] P. Descouvemont, Theoretical Models for Nuclear Astrophysics, Nova Science Publishers, 2004.

[64] T. Szücs, I. Dillmann, R. Plag, Z. Fülöp, Nucl. Data Sheets 120 (2014) 191–193, http://dx.doi.org/10.1016/j.nds.2014.07.043, URL http://www.sciencedirect.com/science/article/pii/S0090375214004955.

[65] M. Galassi, J. Davies, J. Theiler, B. Gough, G. Jungman, P. Alken, M. Booth, F. Rossi, No. Release 2 (1996).

[66] E.P. Wigner, L. Eisenbud, Phys. Rev. 72 (1947) 29–41, http://dx.doi.org/10.1103/PhysRev.72.29, URL https://link.aps.org/doi/10.1103/PhysRev.72.29.

[67] G. Breit, E. Wigner, Phys. Rev. 49 (7) (1936) 519.

[68] R. Azuma, E. Uberseder, E. Simpson, C. Brune, H. Costantini, R. De Boer, J. Görres, M. Heil, P. LeBlanc, C. Ugalde, et al., Phys. Rev. C 81 (4) (2010) 045805.

[69] AZURE: R-matrix program. https://azure.nd.edu/login.php.

[70] D. Bardayan, K. Chipps, S. Ahn, J. Blackmon, R. deBoer, U. Greife, K. Jones, A. Kontos, R. Kozub, L. Linhardt, B. Manning, M. Matoš, P. O'Malley, S. Ota, S. Pain, W. Peters, S. Pittman, A. Sachs, K. Schmitt, M. Smith, P. Thompson, Phys. Lett. B 751 (2015) 311–315, http://dx.doi.org/10.1016/j.physletb.2015.10.073, URL https://www.sciencedirect.com/science/article/pii/S0370269315008321.

[71] http://www.nndc.bnl.gov/.

[72] C. Rolfs, Nucl. Phys. A 217 (1) (1973) 29–70, http://dx.doi.org/10.1016/0375-9474(73)90622-2, URL https://www.sciencedirect.com/science/article/pii/0375947473906222.

[73] N. Timofeyuk, D. Baye, P. Descouvemont, R. Kamouni, I. Thompson, Phys. Rev. Lett. 96 (16) (2006) 162501.

[74] C. Bertulani, Comput. Phys. Comm. 156 (1) (2003) 123–141.

[75] RADCAP: A potential model tool for direct capture reactions. https://data.mendeley.com/datasets/9x582wfz4m/1.

[76] T. Rauscher, K. Grün, H. Krauss, H. Oberhummer, E. Kwasniewicz, Phys. Rev. C 45 (4) (1992) 1996.

[77] I. Thompson, Comput. Phys. Rep. 7 (1988) 167–212.

[78] FRESCO: Coupled reaction channels calculations. http://www.fresco.org.uk/.

[79] R. Tribble, C. Bertulani, M. La Cognata, A. Mukhamedzhanov, C. Spitaleri, Rep. Progr. Phys. 77 (10) (2014) 106901.

[80] I. Stefan, Ph.D. thesis, Université de Caen, France, 2006.

[81] D.W. Bardayan, J.C. Blackmon, C.R. Brune, A.E. Champagne, A.A. Chen, J.M. Cox, T. Davinson, V.Y. Hansper, M.A. Hofstee, B.A. Johnson, R.L. Kozub, Z. Ma, P.D. Parker, D.E. Pierce, M.T. Rabban, A.C. Shotter, M.S. Smith, K.B. Swartz, D.W. Visser, P.J. Woods, Phys. Rev. C 62 (2000) 055804, http://dx.doi.org/10.1103/PhysRevC.62.055804, URL https://link.aps.org/doi/10.1103/PhysRevC.62.055804.

[82] E. Vogt, Rev. Modern Phys. 34 (1962) 723–747, http://dx.doi.org/10.1103/RevModPhys.34.723, URL https://link.aps.org/doi/10.1103/RevModPhys.34.723.

[83] P. Descouvemont, D. Baye, Rep. Progr. Phys. 73 (3) (2010) 036301.

[84] D.W. Bardayan, R.L. Kozub, M.S. Smith, Phys. Rev. C 71 (2005) 018801, http://dx.doi.org/10.1103/PhysRevC.71.018801, URL https://link.aps.org/doi/10.1103/PhysRevC.71.018801.

[85] J.-S. Graulich, S. Cherubini, R. Coszach, S. El Hajjami, W. Galster, P. Leleux, W. Bradfield-Smith, T. Davinson, A. Di Pietro, A.C. Shotter, J. Görres, M. Wiescher, F. Binon, J. Vanhorenbeeck, Phys. Rev. C 63 (2000) 011302, http://dx.doi.org/10.1103/PhysRevC.63.011302, URL https://link.aps.org/doi/10.1103/PhysRevC.63.011302.

[86] A.S.J. Murphy, A.M. Laird, C. Angulo, L. Buchmann, T. Davinson, P. Descouvemont, S.P. Fox, J. José, R. Lewis, C. Ruiz, K. Vaughan, P. Walden, Phys. Rev. C 79 (2009) 058801, http://dx.doi.org/10.1103/PhysRevC.79.058801, URL https://link.aps.org/doi/10.1103/PhysRevC.79.058801.

[87] W.W. Daehnick, R. Sherr, Phys. Rev. 133 (1964) B934–B947, http://dx.doi.org/10.1103/PhysRev.133.B934, URL https://link.aps.org/doi/10.1103/PhysRev.133.B934.

[88] K. Artemov, O. Belyanin, A. Vetoshkin, R. Wolskj, M. Golovkov, V. Goldberg, M. Madeja, V. Pankratov, I. Serikov, V. Timofeev, et al., Sov. J. Nucl. Phys.-USSR 52 (3) (1990) 408–411.

[89] V. Gol'Dberg, A. Pakhomov, Phys. At. Nucl. 56 (9) (1993) 1167–1172.

[90] F. Vanderbist, P. Leleux, C. Angulo, E. Casarejos, M. Couder, M. Loiselet, G. Ryckewaert, P. Descouvemont, M. Aliotta, T. Davinson, Z. Liu, P.J. Woods, Eur. Phys. J. A - Hadron. Nucl. 27 (2) (2006) 183–186, http://dx.doi.org/10.1140/epja/i2005-10265-1.

[91] A.N. Josephides, Studies of States in ^{19}Ne about the ^{18}F + p Threshold and the ^{18}Ne(α, p) HCNO Breakout Reaction (Ph.D. thesis), The University of Edinburgh, 2009.

[92] M. La Cognata, et al., Phys. Rev. C 99 (3) (2019) 034301, http://dx.doi.org/10.1103/PhysRevC.99.034301.

[93] D.W. Bardayan, J.C. Blackmon, W. Bradfield-Smith, C.R. Brune, A.E. Champagne, T. Davinson, B.A. Johnson, R.L. Kozub, C.S. Lee, R. Lewis, P.D. Parker, A.C. Shotter, M.S. Smith, D.W. Visser, P.J. Woods, Phys. Rev. C 62 (2000) 042802, http://dx.doi.org/10.1103/PhysRevC.62.042802, URL https://link.aps.org/doi/10.1103/PhysRevC.62.042802.

[94] D.W. Bardayan, J.C. Blackmon, J. Gómez del Campo, R.L. Kozub, J.F. Liang, Z. Ma, L. Sahin, D. Shapira, M.S. Smith, Phys. Rev. C 70 (2004) 015804, http://dx.doi.org/10.1103/PhysRevC.70.015804, URL https://link.aps.org/doi/10.1103/PhysRevC.70.015804.

[95] H. Smotrich, K.W. Jones, L.C. McDermott, R.E. Benenson, Phys. Rev. 122 (1961) 232–241, http://dx.doi.org/10.1103/PhysRev.122.232, URL https://link.aps.org/doi/10.1103/PhysRev.122.232.

[96] S. Wustenbecker, H. Becker, H. Ebbing, W. Schulte, M. Berheide, M. Buschmann, C. Rolfs, G. Mitchell, J. Schweitzer, Z. Phys. A Hadron. Nucl. 344 (2) (1992) 205–217.

[97] D.J. Mountford, Investigations of Nuclear Reactions Relevant to Stellar γ-Ray Emission (Ph.D. thesis), The University of Edinburgh, 2013.

[98] F. de Oliveira Santos, P. Himpe, M. Lewitowicz, I. Stefan, N. Smirnova, N.L. Achouri, J.C. Angélique, C. Angulo, L. Axelsson, D. Baiborodin, F. Becker, M. Bellegui, E. Berthoumieux, B. Blank, C. Borcea, A. Cassimi, J.M. Daugas, G. de France, F. Dembinski, C.E. Demonchy, Z. Dlouhy, P. Dolégiéviez, C. Donzaud, G. Georgiev, L. Giot, S. Grévy, D. Guillemaud Mueller, V. Lapoux, E. Liénard, M.J. Lopez Jimenez, K. Markenroth, I. Matea, W. Mittig, F. Negoita, G. Neyens, N. Orr, F. Pougheon, P. Roussel Chomaz, M.G. Saint Laurent, F. Sarazin, H. Savajols, M. Sawicka, O. Sorlin, M. Stanoiu, C. Stodel, G. Thiamova, D. Verney, A.C.C. Villari, Eur. Phys. J. A - Hadron. Nucl. 24 (2) (2005) 237–247, http://dx.doi.org/10.1140/epja/i2004-10143-4.

[99] Valerian Girard Alcindor, Ph. D Thesis, Universite de Caen, 2020.

[100] M. Assié, F. de Oliveira Santos, T. Davinson, F. de Grancey, L. Achouri, J.A.-N. nez, T. Al Kalanee, J.-C. Angélique, C. Borcea, R. Borcea, L. Caceres, I. Celikovic, V. Chudoba, D. Pang, C. Ducoin, M. Fallot, O. Kamalou, J. Kiener, Y. Lam, A. Lefebvre-Schuhl, G. Lotay, J. Mrazek, L. Perrot, A. Sánchez-Benítez, F. Rotaru, M.-G. Saint-Laurent, Y. Sobolev, N. Smirnova, M. Stanoiu, I. Stefan, K. Subotic, P. Ujic, R. Wolski, P. Woods, Phys. Lett. B 712 (3) (2012) 198–202, http://dx.doi.org/10.1016/j.physletb.2012.04.059, URL https://www.sciencedirect.com/science/article/pii/S0370269312004881.

[101] R.J. deBoer, Q. Liu, Y. Chen, M. Couder, J. Görres, E. Lamere, A. Long, S. Lyons, K. Manukyan, L. Morales, D. Robertson, C. Seymour, G. Seymour, E. Stech, B.V. Kolk, M. Wiescher, J. Phys. Conf. Ser. 1668 (1) (2020) 012011, http://dx.doi.org/10.1088/1742-6596/1668/1/012011.

[102] P.D. Group, P.A. Zyla, R.M. Barnett, J. Beringer, O. Dahl, D.A. Dwyer, D.E. Groom, C.J. Lin, K.S. Lugovsky, E. Pianori, D.J. Robinson, C.G. Wohl, W.M. Yao, K. Agashe, G. Aielli, B.C. Allanach, C. Amsler, M. Antonelli, E.C. Aschenauer, D.M. Asner, H. Baer, S. Banerjee, L. Baudis, C.W. Bauer, J.J. Beatty, V.I. Belousov, S. Bethke, A. Bettini, O. Biebel, K.M. Black, E. Blucher, O. Buchmuller, V. Burkert, M.A. Bychkov, R.N. Cahn, M. Carena, A. Ceccucci, A. Cerri, D. Chakraborty, R.S. Chivukula, G. Cowan, G. D'Ambrosio, T. Damour, D. de Florian, A. de Gouvêa, T. DeGrand, P. de Jong, G. Dissertori, B.A. Dobrescu, M. D'Onofrio, M. Doser, M. Drees, H.K. Dreiner, P. Eerola, U. Egede, S. Eidelman, J. Ellis, J. Erler, V.V. Ezhela, W. Fetscher, B.D. Fields, B. Foster, A. Freitas, H. Gallagher, L. Garren, H.J. Gerber, G. Gerbier, T. Gershon, Y. Gershtein, T. Gherghetta, A.A. Godizov, M.C. Gonzalez-Garcia, M. Goodman, C. Grab, A.V. Gritsan, C. Grojean, M. Grünewald, A. Gurtu, T. Gutsche, H.E. Haber, C. Hanhart, S. Hashimoto, Y. Hayato, A. Hebecker, S. Heinemeyer, B. Heltsley, J.J. Hernández-Rey, K. Hikasa, J. Hisano, A. Höcker, J. Holder, A. Holtkamp, J. Huston, T. Hyodo, K.F. Johnson, M. Kado, M. Karliner, U.F. Katz, M. Kenzie, V.A. Khoze, S.R. Klein, E. Klempt, R.V. Kowalewski, F. Krauss, M. Kreps, B. Krusche, Y. Kwon, O. Lahav, J. Laiho, L.P. Lellouch, J. Lesgourgues, A.R. Liddle, Z. Ligeti, C. Lippmann, T.M. Liss, L. Littenberg, C. Lourengo, S.B. Lugovsky, A. Lusiani, Y. Makida, F. Maltoni, T. Mannel, A.V. Manohar, W.J. Marciano, A. Masoni, J. Matthews, U.G. Meißner, M. Mikhasenko, D.J. Miller, D. Milstead, R.E. Mitchell, K. Mönig, P. Molaro, F. Moortgat, M. Moskovic, K. Nakamura, M. Narain, P. Nason, S. Navas, M. Neubert, P. Nevski, Y. Nir, K.A. Olive, C. Patrignani, J.A. Peacock, S.T. Petcov, V.A. Petrov, A. Pich, A. Piepke, A. Pomarol, S. Profumo, A. Quadt, K. Rabbertz, J. Rademacker, G. Raffelt, H. Ramani, M. Ramsey-Musolf, B.N. Ratcliff, P. Richardson, A. Ringwald, S. Roesler, S. Rolli, A. Romaniouk, L.J. Rosenberg, J.L. Rosner, G. Rybka, M. Ryskin, R.A. Ryutin, Y. Sakai, G.P. Salam, S. Sarkar, F. Sauli, O. Schneider, K. Scholberg, A.J. Schwartz, J. Schwiening, D. Scott, V. Sharma, S.R. Sharpe, T. Shutt, M. Silari, T. Sjöstrand, P. Skands, T. Skwarnicki, G.F. Smoot, A. Soffer, M.S. Sozzi, S. Spanier, C. Spiering, A. Stahl, S.L. Stone, Y. Sumino, T. Sumiyoshi, M.J. Syphers, F. Takahashi, M. Tanabashi, J. Tanaka, M. Taševský, K. Terashi, J. Terning, U. Thoma, R.S. Thorne, L. Tiator, M. Titov, N.P. Tkachenko, D.R. Tovey, K. Trabelsi, P. Urquijo, G. Valencia, R. Van de Water, N. Varelas, G. Venanzoni, L. Verde, M.G. Vincter, P. Vogel, W. Vogelsang, A. Vogt, V. Vorobyev, S.P. Wakely, W. Walkowiak, C.W. Walter, D. Wands, M.O. Wascko, D.H. Weinberg, E.J. Weinberg, M. White, L.R. Wiencke, S. Willocq, C.L. Woody, R.L. Workman, M. Yokoyama, R. Yoshida, G. Zanderighi, G.P. Zeller, O.V. Zenin, R.Y. Zhu, S.L. Zhu, F. Zimmermann, J. Anderson, T. Basaglia, V.S. Lugovsky, P. Schaffner, W. Zheng, Prog. Theor. Exp. Phys. 2020 (8) (2020) 083C01, http://dx.doi.org/10.1093/ptep/ptaa104, arXiv:https://academic.oup.com/ptep/article-pdf/2020/8/083C01/34673722/ptaa104.pdf.

[103] R. Brun, F. Rademakers, Nucl. Instrum. Methods Phys. Res. A 389 (1–2) (1997) 81–86.

[104] D. Mountford, R. deBoer, P. Descouvemont, A.S.J. Murphy, E. Uberseder, M. Wiescher, Nucl. Instrum. Methods Phys. Res. A 767 (2014) 359–363, http://dx.doi.org/10.1016/j.nima.2014.08.047, URL https://www.sciencedirect.com/science/article/pii/S0168900214009826.

[105] H. Yamaguchi, Y. Wakabayashi, S. Kubono, G. Amadio, H. Fujikawa, T. Teranishi, A. Saito, J. He, S. Nishimura, Y. Togano, Y. Kwon, M. Niikura, N. Iwasa, K. Inafuku, L. Khiem, Phys. Lett. B 672 (3) (2009) 230–234, http://dx.doi.org/10.1016/j.physletb.2009.01.033, URL http://www.sciencedirect.com/science/article/pii/S037026930900080X.

[106] D. Torresi, L. Cosentino, P. Descouveont, A. Di Pietro, C. Ducoin, P. Figuera, M. Fisichella, M. Lattuada, C. Maiolino, A. Musumarra, M. Papa, M.G. Pellegriti, M. Rovituso, D. Santonocito, G. Scalia, V. Scuderi, E. Strano, M. Zadro, J. Phys. Conf. Ser. 569 (1) (2014) 012024, http://dx.doi.org/10.1088/1742-6596/569/1/012024.

[107] M. Pellegriti, N. Achouri, C. Angulo, J.-C. Angélique, E. Berthoumieux, E. Casarejos, M. Couder, T. Davinson, C. Ghag, A. Murphy, N. Orr, I. Ray, I. Stefan, P. Descouvemont, Phys. Lett. B 659 (5) (2008) 864–869, http://dx.doi.org/10.1016/j.physletb.2007.12.017, URL https://www.sciencedirect.com/science/article/pii/S0370269307015377.

[108] R.P. Feynman, R.B. Leighton, M. Sands, Lectures on Physics: Quantum Mechanics, Pearson, Addison Wesley, 2006.

[109] J.G. Pronko, R.G. Hirko, D.C. Slater, Phys. Rev. C 7 (1973) 1382–1389, http://dx.doi.org/10.1103/PhysRevC.7.1382, URL https://link.aps.org/doi/10.1103/PhysRevC.7.1382.

[110] T. Otsubo, I. Asada, M. Takeda, M. Tsuda, Y. Oda, Nucl. Phys. A 259 (3) (1976) 452–460, http://dx.doi.org/10.1016/0375-9474(76)90081-6, URL https://www.sciencedirect.com/science/article/pii/0375947476900816.

[111] A.S. Adekola, C.R. Brune, D.W. Bardayan, J.C. Blackmon, K.Y. Chae, C. Domizioli, U. Greife, Z. Heinen, M.J. Hornish, K.L. Jones, R.L. Kozub, R.J. Livesay, Z. Ma, T.N. Massey, B. Moazen, C.D. Nesaraja, S.D. Pain, J.F. Shriner, N.D. Smith, M.S. Smith, J.S. Thomas, D.W. Visser, A.V. Voinov, Phys. Rev. C 84 (2011) 054611, http://dx.doi.org/10.1103/PhysRevC.84.054611, URL https://link.aps.org/doi/10.1103/PhysRevC.84.054611.

[112] J.C. Dalouzy, L. Achouri, M. Aliotta, C. Angulo, H. Benhabiles, C. Borcea, R. Borcea, P. Bourgault, A. Buta, A. Coc, A. Damman, T. Davinson, F. de Grancey, F. de Oliveira Santos, N. de Séréville, J. Kiener, M.G. Pellegriti, F. Negoita, A.M. Sánchez-Benítez, O. Sorlin, M. Stanoiu, I. Stefan, P.J. Woods, Phys. Rev. Lett. 102 (2009) 162503, http://dx.doi.org/10.1103/PhysRevLett.102.162503, URL https://link.aps.org/doi/10.1103/PhysRevLett.102.162503.
[113] J.E. Riley, A.M. Laird, N. de Séréville, A. Parikh, S.P. Fox, F. Hammache, I. Stefan, P. Adsley, M. Assié, B. Bastin, F. Boulay, A. Coc, S. Franchoo, R. Garg, S.A. Gillespie, V. Guimaraes, C. Hamadache, N. Hubbard, J. Kiener, A. Lefebvre-Schuhl, F.d. Santos, A. Remadi, L. Perrot, D. Suzuki, G. Verde, V. Tatischeff, M. Williams, Phys. Rev. C 103 (2021) 015807, http://dx.doi.org/10.1103/PhysRevC.103.015807, URL https://link.aps.org/doi/10.1103/PhysRevC.103.015807.
[114] J.A. Kuehner, Phys. Rev. 125 (1962) 1650–1655, http://dx.doi.org/10.1103/PhysRev.125.1650, URL https://link.aps.org/doi/10.1103/PhysRev.125.1650.
[115] D.W. Visser, J.A. Caggiano, R. Lewis, W.B. Handler, A. Parikh, P.D. Parker, Phys. Rev. C 69 (2004) 048801, http://dx.doi.org/10.1103/PhysRevC.69.048801, URL https://link.aps.org/doi/10.1103/PhysRevC.69.048801.
[116] J. Pronko, R. Lindgren, Nucl. Instrum. Methods 98 (3) (1972) 445–449, http://dx.doi.org/10.1016/0029-554X(72)90226-1, URL https://www.sciencedirect.com/science/article/pii/0029554X72902261.
[117] J.G. Pronko, R.G. Hirko, D.C. Slater, Phys. Rev. C 7 (1973) 1382.
[118] J. Cramer, W. Eidson, Nucl. Phys. 55 (1964) 593–612, http://dx.doi.org/10.1016/0029-5582(64)90179-8, URL https://www.sciencedirect.com/science/article/pii/0029558264901798.
[119] A.J. Ferguson, Angular Correlation Methods in Gamma-Ray Spectroscopy, North-Holland Publishing Company, 1965.
[120] F. Boulay, B. Bastin, F.d. Santos, T. Davinson, A. Lemasson, P. Ujic, J. Mrazek, A.M. Sánchez-Benítez, E. Traykov, D. Ramos, L. Achouri, L. Acosta, C. Borcea, M. Ciemala, P. Delahaye, A. Estrade, G. de France, J. Grinyer, B. Jacquot, O. Kamalou, A. Laird, V. Margerin, G. Marquinez-Duran, F. Negoita, M. Rejmund, C. Rodriguez-Tajes, F. Rotaru, C. Schmitt, N. de Séréville, O. Sorlin, M. Stanoiu, J. Thomas, P. Woods, J. Phys. Conf. Ser. 940 (1) (2018) 012003, http://dx.doi.org/10.1088/1742-6596/940/1/012003.
[121] J. Dalouzy, Spectroscopie du ^{19}Ne par Diffusion Inélastique. Applications à l'Astrophysique (Ph.D. thesis), Université de Caen, 2008, URL https://theses.hal.science/tel-00365695.
[122] J. Spencer, H. Enge, Nucl. Instrum. Methods 49 (2) (1967) 181–193, http://dx.doi.org/10.1016/0029-554X(67)90684-2, URL https://www.sciencedirect.com/science/article/pii/0029554X67906842.
[123] D. Overway, J. Jänecke, F. Becchetti, C. Thorn, G. Kekelis, Nucl. Phys. A 366 (2) (1981) 299–319, http://dx.doi.org/10.1016/0375-9474(81)90290-6, URL https://www.sciencedirect.com/science/article/pii/0375947481902906.
[124] M. Dufour, P. Descouvemont, Nucl. Phys. A 785 (3) (2007) 381–394, http://dx.doi.org/10.1016/j.nuclphysa.2006.12.101, URL https://www.sciencedirect.com/science/article/pii/S0375947407000292.
[125] P. Descouvemont, D. Baye, Nucl. Phys. A 463 (3) (1987) 629–643, http://dx.doi.org/10.1016/0375-9474(87)90635-X, URL https://www.sciencedirect.com/science/article/pii/037594748790635X.
[126] K. Shimazoe, M. Uenomachi, H. Takahashi, Commun. Phys. 5 (1) (2022) 24, http://dx.doi.org/10.1038/s42005-022-00801-w.
[127] A.S. Adekola, C.R. Brune, D.W. Bardayan, J.C. Blackmon, K.Y. Chae, J.A. Cizewski, K.L. Jones, R.L. Kozub, T.N. Massey, C.D. Nesaraja, S.D. Pain, J.F. Shriner, M.S. Smith, J.S. Thomas, Phys. Rev. C 85 (2012) 037601, http://dx.doi.org/10.1103/PhysRevC.85.037601, URL https://link.aps.org/doi/10.1103/PhysRevC.85.037601.
[128] F. Portillo, R. Longland, A.L. Cooper, S. Hunt, A.M. Laird, C. Marshall, K. Setoodehnia, Phys. Rev. C 107 (2023) 035809, http://dx.doi.org/10.1103/PhysRevC.107.035809, URL https://link.aps.org/doi/10.1103/PhysRevC.107.035809.
[129] K. Ma, Y.-L. Ye, C.-J. Lin, J.-H. Chen, D.-X. Wang, J.-X. Han, H.-M. Jia, L. Yang, L.-S. Yang, Z.-Y. Hu, Y. Chen, W.-L. Pu, G. Li, Z.-W. Tan, D.-H. Huang, T.-P. Luo, S.-H. Zhong, J.-L. Lou, X.-F. Yang, Z.-H. Li, Q.-T. Li, J.-Y. Xu, Z.-H. Yang, K. Wei, Chin. Phys. C 47 (11) (2023) 114001, http://dx.doi.org/10.1088/1674-1137/acc16f.
[130] D.W. Bardayan, J. Phys. G: Nucl. Part. Phys. 43 (4) (2016) 043001, http://dx.doi.org/10.1088/0954-3899/43/4/043001.
[131] N. de Séréville, A. Coc, C. Angulo, M. Assunção, D. Beaumel, B. Bouzid, S. Cherubini, M. Couder, P. Demaret, F. de Oliveira Santos, P. Figuera, S. Fortier, M. Gaelens, F. Hammache, J. Kiener, D. Labar, A. Lefebvre, P. Leleux, M. Loiselet, A. Ninane, S. Quichaoui, G. Ryckewaert, N. Smirnova, V. Tatischeff, J.-P. Thibaud, Nucl. Phys. A 718 (2003) 259–262, http://dx.doi.org/10.1016/S0375-9474(03)00725-5, URL https://www.sciencedirect.com/science/article/pii/S0375947403007255.
[132] K.E. Rehm, F. Borasi, C.L. Jiang, D. Ackermann, I. Ahmad, B.A. Brown, F. Brumwell, C.N. Davids, P. Decrock, S.M. Fischer, J. Görres, J. Greene, G. Hackmann, B. Harss, D. Henderson, W. Henning, R.V.F. Janssens, G. McMichael, V. Nanal, D. Nisius, J. Nolen, R.C. Pardo, M. Paul, P. Reiter, J.P. Schiffer, D. Seweryniak, R.E. Segel, M. Wiescher, A.H. Wuosmaa, Phys. Rev. Lett. 80 (1998) 676–679, http://dx.doi.org/10.1103/PhysRevLett.80.676, URL https://link.aps.org/doi/10.1103/PhysRevLett.80.676.
[133] J.G. Camacho, A.M. Moro, Euroschool Exot. Beams 4 (2014) 39–66.
[134] C. Cohen-Tannoudji, B. Diu, F. Laloe, B. Dui, Quantum mechanics (2 vol. set), 2006.
[135] M. Born, Z. Phys. 37 (12) (1926) 863–867, http://dx.doi.org/10.1007/BF01397477.
[136] D. Jackson, Ltd. Lond. (1970).
[137] F. de Oliveira, A. Coc, P. Aguer, C. Angulo, G. Bogaert, J. Kiener, A. Lefebvre, V. Tatischeff, J.-P. Thibaud, S. Fortier, J. Maison, L. Rosier, G. Rotbard, J. Vernotte, M. Arnould, A. Jorissen, N. Mowlavi, Nucl. Phys. A 597 (2) (1996) 231–252, http://dx.doi.org/10.1016/0375-9474(95)00455-6, URL https://www.sciencedirect.com/science/article/pii/0375947495004556.
[138] R.H. Bassel, Phys. Rev. 149 (1966) 791–797, http://dx.doi.org/10.1103/PhysRev.149.791, URL https://link.aps.org/doi/10.1103/PhysRev.149.791.
[139] C. Iliadis, M. Wiescher, Phys. Rev. C 69 (2004) 064305, http://dx.doi.org/10.1103/PhysRevC.69.064305, URL https://link.aps.org/doi/10.1103/PhysRevC.69.064305.
[140] P. Kunz, U. Color. 30/Jun/1982 Version.
[141] M.H. Macfarlane, J.B. French, Rev. Modern Phys. 32 (1960) 567–691, http://dx.doi.org/10.1103/RevModPhys.32.567, URL https://link.aps.org/doi/10.1103/RevModPhys.32.567.
[142] P. Brussaard, P. Glaudemans, A. Klein, Shell-model applications in nuclear spectroscopy, 1978.
[143] I. Towner, J. Hardy, At. Data Nucl. Data Tables 6 (2) (1969) 153–234.
[144] B.A. Brown, Natl. Super Conduct. Cyclotr. Lab. 11 (2005).
[145] C. Iliadis, Nucl. Phys. A 618 (1–2) (1997) 166–175.
[146] R.L. Kozub, D.W. Bardayan, J.C. Batchelder, J.C. Blackmon, C.R. Brune, A.E. Champagne, J.A. Cizewski, T. Davinson, U. Greife, C.J. Gross, C.C. Jewett, R.J. Livesay, Z. Ma, B.H. Moazen, C.D. Nesaraja, L. Sahin, J.P. Scott, D. Shapira, M.S. Smith, J.S. Thomas, P.J. Woods, Phys. Rev. C 71 (2005) 032801, http://dx.doi.org/10.1103/PhysRevC.71.032801, URL https://link.aps.org/doi/10.1103/PhysRevC.71.032801.
[147] D.W. Bardayan, K.A. Chipps, S. Ahn, J.C. Blackmon, S. Carmichael, U. Greife, K.L. Jones, J. José, A. Kontos, R.L. Kozub, L. Linhardt, B. Manning, M. Matoš, P.D. O'Malley, S. Ota, S.D. Pain, W.A. Peters, S.T. Pittman, A. Sachs, K.T. Schmitt, M.S. Smith, P. Thompson, Phys. Rev. C 96 (2017) 055806, http://dx.doi.org/10.1103/PhysRevC.96.055806, URL https://link.aps.org/doi/10.1103/PhysRevC.96.055806.
[148] TALYS. https://tendl.web.psi.ch/tendl_2019/talys.html.
[149] J. Lighthall, B. Back, S. Baker, S. Freeman, H. Lee, B. Kay, S. Marley, K. Rehm, J. Rohrer, J. Schiffer, D. Shetty, A. Vann, J. Winkelbauer, A. Wuosmaa, Nucl. Instrum. Methods Phys. Res. A 622 (1) (2010) 97–106, http://dx.doi.org/10.1016/j.nima.2010.06.220, URL https://www.sciencedirect.com/science/article/pii/S0168900210014105.

[150] P.T. MacGregor, D.K. Sharp, S.J. Freeman, C.R. Hoffman, B.P. Kay, T.L. Tang, L.P. Gaffney, E.F. Baader, M.J.G. Borge, P.A. Butler, W.N. Catford, B.D. Cropper, G. de Angelis, J. Konki, T. Kröll, M. Labiche, I.H. Lazarus, R.S. Lubna, I. Martel, D.G. McNeel, R.D. Page, O. Poleshchuk, R. Raabe, F. Recchia, J. Yang, Phys. Rev. C 104 (2021) L051301, http://dx.doi.org/10.1103/PhysRevC.104.L051301, URL https://link.aps.org/doi/10.1103/PhysRevC.104.L051301.

[151] SOLARIS solenoid spectrometer. https://www.anl.gov/phy/solaris.

[152] A.M. Laird, A. Parikh, A.S.J. Murphy, K. Wimmer, A.A. Chen, C.M. Deibel, T. Faestermann, S.P. Fox, B.R. Fulton, R. Hertenberger, D. Irvine, J. José, R. Longland, D.J. Mountford, B. Sambrook, D. Seiler, H.-F. Wirth, Phys. Rev. Lett. 110 (2013) 032502, http://dx.doi.org/10.1103/PhysRevLett.110.032502, URL https://link.aps.org/doi/10.1103/PhysRevLett.110.032502.

[153] A. Kankainen, P.J. Woods, F. Nunes, C. Langer, H. Schatz, V. Bader, T. Baugher, D. Bazin, B.A. Brown, J. Browne, D.T. Doherty, A. Estrade, A. Gade, A. Kontos, G. Lotay, Z. Meisel, F. Montes, S. Noji, G. Perdikakis, J. Pereira, F. Recchia, T. Redpath, R. Stroberg, M. Scott, D. Seweryniak, J. Stevens, D. Weisshaar, K. Wimmer, R. Zegers, Eur. Phys. J. A 52 (1) (2016) 6.

[154] A. Kankainen, P. Woods, H. Schatz, T. Poxon-Pearson, D. Doherty, V. Bader, T. Baugher, D. Bazin, B. Brown, J. Browne, A. Estrade, A. Gade, J. José, A. Kontos, C. Langer, G. Lotay, Z. Meisel, F. Montes, S. Noji, F. Nunes, G. Perdikakis, J. Pereira, F. Recchia, T. Redpath, R. Stroberg, M. Scott, D. Seweryniak, J. Stevens, D. Weisshaar, K. Wimmer, R. Zegers, Phys. Lett. B 769 (2017) 549–553, http://dx.doi.org/10.1016/j.physletb.2017.01.084, URL https://www.sciencedirect.com/science/article/pii/S0370269317301338.

[155] A. Matta, P. Morfouace, N. de Séréville, F. Flavigny, M. Labiche, R. Shearman, J. Phys. G: Nucl. Part. Phys. 43 (4) (2016) 045113, http://dx.doi.org/10.1088/0954-3899/43/4/045113.

[156] NPTool. https://nptool.in2p3.fr/.

[157] C. Perey, F. Perey, At. Data Nucl. Data Tables 17 (1) (1976) 1–101, http://dx.doi.org/10.1016/0092-640X(76)90007-3, URL https://www.sciencedirect.com/science/article/pii/0092640X76900073.

[158] L.M. Martz, S.J. Sanders, P.D. Parker, C.B. Dover, Phys. Rev. C 20 (1979) 1340–1346, http://dx.doi.org/10.1103/PhysRevC.20.1340, URL https://link.aps.org/doi/10.1103/PhysRevC.20.1340.

[159] F. Pühlhofer, H. Ritter, R. Bock, G. Brommundt, H. Schmidt, K. Bethge, Nucl. Phys. A 147 (2) (1970) 258–272, http://dx.doi.org/10.1016/0375-9474(70)90266-6, URL https://www.sciencedirect.com/science/article/pii/0375947470902666.

[160] W.R. Coker, Phys. Rev. C 9 (1974) 784–786, http://dx.doi.org/10.1103/PhysRevC.9.784, URL https://link.aps.org/doi/10.1103/PhysRevC.9.784.

[161] D.H. Luong, D.J. Hinde, M. Dasgupta, M. Evers, R. Rafiei, R. du Rietz, EPJ Web Conf. 17 (2011) 03002, http://dx.doi.org/10.1051/epjconf/20111703002.

[162] M.S. Kwag, K.Y. Chae, S. Ahn, D.W. Bardayan, K.A. Chipps, J.A. Cizewski, M.E. Howard, R.L. Kozub, K. Kwak, B. Manning, M. Matos, P.D. O'Malley, S.D. Pain, W.A. Peters, S.T. Pittman, A. Ratkiewicz, M.S. Smith, S. Strauss, Eur. Phys. J. A (4) 108, http://dx.doi.org/10.1140/epja/s10050-020-00106-y.

[163] P. Buttle, L. Goldfarb, Nucl. Phys. A 176 (2) (1971) 299–320, http://dx.doi.org/10.1016/0375-9474(71)90272-7, URL https://www.sciencedirect.com/science/article/pii/0375947471902727.

[164] M. McCleskey, A.M. Mukhamedzhanov, L. Trache, R.E. Tribble, A. Banu, V. Eremenko, V.Z. Goldberg, Y.-W. Lui, E. McCleskey, B.T. Roeder, A. Spiridon, F. Carstoiu, V. Burjan, Z. Hons, I.J. Thompson, Phys. Rev. C 89 (2014) 044605, http://dx.doi.org/10.1103/PhysRevC.89.044605, URL https://link.aps.org/doi/10.1103/PhysRevC.89.044605.

[165] P. Descouvemont, Astrophys. J. 543 (1) (2000) 425.

[166] C.R. Brune, W.H. Geist, R.W. Kavanagh, K.D. Veal, Phys. Rev. Lett. 83 (1999) 4025–4028, http://dx.doi.org/10.1103/PhysRevLett.83.4025, URL https://link.aps.org/doi/10.1103/PhysRevLett.83.4025.

[167] F. de Oliveira, A. Coc, P. Aguer, G. Bogaert, J. Kiener, A. Lefebvre, V. Tatischeff, J.-P. Thibaud, S. Fortier, J.M. Maison, L. Rosier, G. Rotbard, J. Vernotte, S. Wilmes, P. Mohr, V. Kölle, G. Staudt, Phys. Rev. C 55 (1997) 3149–3151, http://dx.doi.org/10.1103/PhysRevC.55.3149, URL https://link.aps.org/doi/10.1103/PhysRevC.55.3149.

[168] J.P.L. Fernandez, N. Michel, M. Płoszajczak, A. Mercenne, Phys. Rev. C 108 (2023) 044616, http://dx.doi.org/10.1103/PhysRevC.108.044616, URL https://link.aps.org/doi/10.1103/PhysRevC.108.044616.

[169] G. Baur, Phys. Lett. B 178 (2–3) (1986) 135–138.

[170] C. Spitaleri, M. La Cognata, L. Lamia, A.M. Mukhamedzhanov, R.G. Pizzone, Eur. Phys. J. A 52 (4) (2016) 77, http://dx.doi.org/10.1140/epja/i2016-16077-2.

[171] S. Typel, G. Baur, Ann. Physics 305 (2) (2003) 228–265.

[172] C. Spitaleri, A. Mukhamedzhanov, L. Blokhintsev, M. La Cognata, R. Pizzone, A. Tumino, Phys. At. Nucl. 74 (12) (2011) 1725–1739.

[173] A. Tumino, C. Spitaleri, S. Cherubini, M. Gulino, M. La Cognata, L. Lamia, R. Pizzone, S. Puglia, G. Rapisarda, S. Romano, et al., Few-Body Syst. 54 (5–6) (2013) 745–753.

[174] D.Y. Pang, A.M. Mukhamedzhanov, Phys. Rev. C 90 (2014) 044611, http://dx.doi.org/10.1103/PhysRevC.90.044611, URL https://link.aps.org/doi/10.1103/PhysRevC.90.044611.

[175] A. Mukhamedzhanov, L. Blokhintsev, B. Irgaziev, A. Kadyrov, M. La Cognata, C. Spitaleri, R. Tribble, J. Phys. G: Nucl. Part. Phys. 35 (1) (2008) 014016.

[176] M. La Cognata, S. Romano, C. Spitaleri, S. Cherubini, V. Crucillà, M. Gulino, L. Lamia, R.G. Pizzone, A. Tumino, R. Tribble, C. Fu, V.Z. Goldberg, A.M. Mukhamedzhanov, D. Schmidt, G. Tabacaru, L. Trache, B.F. Irgaziev, Phys. Rev. C 76 (2007) 065804, http://dx.doi.org/10.1103/PhysRevC.76.065804, URL https://link.aps.org/doi/10.1103/PhysRevC.76.065804.

[177] M. La Cognata, C. Spitaleri, A.M. Mukhamedzhanov, B. Irgaziev, R.E. Tribble, A. Banu, S. Cherubini, A. Coc, V. Crucillà, V.Z. Goldberg, M. Gulino, G.G. Kiss, L. Lamia, J. Mrazek, R.G. Pizzone, S.M.R. Puglia, G.G. Rapisarda, S. Romano, M.L. Sergi, G. Tabacaru, L. Trache, W. Trzaska, A. Tumino, Phys. Rev. Lett. 101 (2008) 152501, http://dx.doi.org/10.1103/PhysRevLett.101.152501, URL https://link.aps.org/doi/10.1103/PhysRevLett.101.152501.

[178] R.G. Pizzone, B.T. Roeder, M. McCleskey, L. Trache, R.E. Tribble, C. Spitaleri, C.A. Bertulani, S. Cherubini, M. Gulino, I. Indelicato, M. La Cognata, L. Lamia, G.G. Rapisarda, R. Spartá, Eur. Phys. J. A 52 (2) (2016) 24, http://dx.doi.org/10.1140/epja/i2016-16024-3.

[179] M. Lattuada, F. Riggi, D. Vinciguerra, C. Spitaleri, G. Vourvopoulos, D. Miljanic, E. Norbeck, Z. Phys. At. Nucl. 330 (2) (1988) 183–188.

[180] S. Cherubini, V. Kondratyev, M. Lattuada, C. Spitaleri, D. Miljanic, M. Zadro, G. Baur, Astrophys. J. 457 (1996) 855.

[181] C. Spitaleri, S. Typel, R.G. Pizzone, M. Aliotta, S. Blagus, M. Bogovac, S. Cherubini, P. Figuera, M. Lattuada, M. Milin, D. Miljanić, A. Musumarra, M.G. Pellegriti, D. Rendić, C. Rolfs, S. Romano, N. Soić, A. Tumino, H.H. Wolter, M. Zadro, Phys. Rev. C 63 (2001) 055801, http://dx.doi.org/10.1103/PhysRevC.63.055801, URL https://link.aps.org/doi/10.1103/PhysRevC.63.055801.

[182] A. Musumarra, R. Pizzone, S. Blagus, M. Bogovac, P. Figuera, M. Lattuada, M. Milin, D. Miljanic, M. Pellegriti, D. Rendic, et al., Phys. Rev. C 64 (6) (2001) 068801.

[183] M. La Cognata, C. Spitaleri, O. Trippella, G. Kiss, G. Rogachev, A. Mukhamedzhanov, M. Avila, G. Guardo, E. Koshchiy, A. Kuchera, et al., Phys. Rev. Lett. 109 (23) (2012) 232701.

[184] A. Tumino, C. Spitaleri, M. La Cognata, S. Cherubini, G. Guardo, M. Gulino, S. Hayakawa, I. Indelicato, L. Lamia, H. Petrascu, et al., Nature 557 (7707) (2018) 687.

[185] M. Gulino, S. Cherubini, G.G. Rapisarda, S. Kubono, L. Lamia, M.L. Cognata, H. Yamaguchi, S. Hayakawa, Y. Wakabayashi, N. Iwasa, S. Kato, H. Komatsubara, T. Teranishi, A. Coc, N.D. Séréville, F. Hammache, C. Spitaleri, J. Phys. Conf. Ser. 420 (1) (2013) 012149, http://dx.doi.org/10.1088/1742-6596/420/1/012149.

[186] M. La Cognata, C. Spitaleri, R. Tribble, T. Al-Abdullah, A. Banu, S. Cherubini, V. Crucillà, C. Fu, V. Goldberg, M. Gulino, et al., J. Phys. G: Nucl. Part. Phys. 35 (1) (2007) 014014.

[187] M.L. Cognata, C. Spitaleri, A. Mukhamedzhanov, A. Banu, S. Cherubini, A. Coc, V. Crucillà, V. Goldberg, M. Gulino, B. Irgaziev, G.G. Kiss, L. Lamia, J. Mrazek, R.G. Pizzone, S.M.R. Puglia, G.G. Rapisarda, S. Romano, M.L. Sergi, G. Tabacaru, L. Trache, R.E. Tribble, W. Trzaska, A. Tumino, Astrophys. J. 708 (1) (2009) 796, http://dx.doi.org/10.1088/0004-637X/708/1/796.

[188] M.L. Cognata, R.G. Pizzone, J. José, M. Hernanz, S. Cherubini, M. Gulino, G.G. Rapisarda, C. Spitaleri, Astrophys. J. 846 (1) (2017) 65, http://dx.doi.org/10.3847/1538-4357/aa845f.

[189] A. Tumino, C.A. Bertulani, M. La Cognata, L. Lamia, R.G. Pizzone, S. Romano, S. Typel, Annu. Rev. Nucl. Part. Sci. 71 (Volume 71, 2021) (2021) 345–376, http://dx.doi.org/10.1146/annurev-nucl-102419-033642, URL https://www.annualreviews.org/content/journals/10.1146/annurev-nucl-102419-033642.

[190] T. Budner, M. Friedman, C. Wrede, B.A. Brown, J. José, D. Pérez-Loureiro, L.J. Sun, J. Surbrook, Y. Ayyad, D.W. Bardayan, K. Chae, A.A. Chen, K.A. Chipps, M. Cortesi, B. Glassman, M.R. Hall, M. Janasik, J. Liang, P. O'Malley, E. Pollacco, A. Psaltis, J. Stomps, T. Wheeler, Phys. Rev. Lett. 128 (2022) 182701, http://dx.doi.org/10.1103/PhysRevLett.128.182701, URL https://link.aps.org/doi/10.1103/PhysRevLett.128.182701.

[191] I. Stefanescu, A. Spiridon, L. Trache, E. Pollacco, A. Saastamoinen, B. Roeder, J. Phys. Conf. Ser. 1024 (1) (2018) 012007, http://dx.doi.org/10.1088/1742-6596/1024/1/012007.

[192] C. Wrede, B.E. Glassman, D. Pérez-Loureiro, J.M. Allen, D.W. Bardayan, M.B. Bennett, B.A. Brown, K.A. Chipps, M. Febbraro, C. Fry, M.R. Hall, O. Hall, S.N. Liddick, P. O'Malley, W.-J. Ong, S.D. Pain, S.B. Schwartz, P. Shidling, H. Sims, P. Thompson, H. Zhang, Phys. Rev. C 96 (2017) 032801, http://dx.doi.org/10.1103/PhysRevC.96.032801, URL https://link.aps.org/doi/10.1103/PhysRevC.96.032801.

[193] C. Iliadis, R. Longland, A. Champagne, A. Coc, R. Fitzgerald, Nucl. Phys. A 841 (1) (2010) 31–250, http://dx.doi.org/10.1016/j.nuclphysa.2010.04.009, URL https://www.sciencedirect.com/science/article/pii/S0375947410004197. The 2010 Evaluation of Monte Carlo based Thermonuclear Reaction Rates.

[194] M.R. Hall, D.W. Bardayan, T. Baugher, A. Lepailleur, S.D. Pain, A. Ratkiewicz, S. Ahn, J.M. Allen, J.T. Anderson, A.D. Ayangeakaa, J.C. Blackmon, S. Burcher, M.P. Carpenter, S.M. Cha, K.Y. Chae, K.A. Chipps, J.A. Cizewski, M. Febbraro, O. Hall, J. Hu, C.L. Jiang, K.L. Jones, E.J. Lee, P.D. O'Malley, S. Ota, B.C. Rasco, D. Santiago-Gonzalez, D. Seweryniak, H. Sims, K. Smith, W.P. Tan, P. Thompson, C. Thornsberry, R.L. Varner, D. Walter, G.L. Wilson, S. Zhu, Phys. Rev. C 102 (2020) 045802, http://dx.doi.org/10.1103/PhysRevC.102.045802, URL https://link.aps.org/doi/10.1103/PhysRevC.102.045802.